Graduate Theses and Dissertations

Iowa State University Capstones, Theses and Dissertations

2015

Device physics of organic and perovskite solar cells

Mehran Samiee Esfahani
Iowa State University

Follow this and additional works at: https://lib.dr.iastate.edu/etd

Part of the Electrical and Electronics Commons

Device physics of organic and perovskite solar cells

by

Mehran Samiee Esfahani

A dissertation submitted to the graduate faculty

in partial fulfillment of the requirements for the degree of

DOCTOR OF PHILOSOPHY

Major: Electrical Engineering

Program of Study Committee:
Vikram Dalal, Major Professor
Rana Biswas
Joseph Shinar
Sumit Chaudhary
Mani Mina

Iowa State University

Ames, Iowa

2015

TABLE OF CONTENTS

iv

ACKNOWLEDGEMENTS

ABSTRACT

We report on fundamental electronic properties of the PTB7:PCBM$_{70}$ bulk heterojunction solar cells: Sub-gap quantum efficiency measurements determine the Urbach energy of tail states (33 meV) and D/A interfacial bandgap (1.34 eV). Density of deep defects is determined by capacitance spectroscopy, and is $\sim10^{16}$ cm^{-3}.eV^{-1}. By photo-current spectroscopy, we assess surface recombination velocity at D/A interface, which translates to a capture cross-section of $\sim10^{-16}$ cm^2 for deep defects. These properties are then used in our analytical modeling. Using a multiple-level trap model, we compute recombination rates in the cells. The model can predict dark saturation currents and ideality factors, and strongly suggests that band tail recombination is the main limiting factor of open-circuit voltage.

Additionally, we find that, upon light exposure, photo-induced defects lead to increased trap-assisted recombination and photo-voltage instability. To increase photo-stability, we propose a novel n-i-p hybrid device where n$^+$/a-Si:H is used as the front contact of the bulk heterojunction. Highly energetic photons (blue and UV light), which induce defects in the light-absorbing material, are blocked (absorbed) in the n$^+$/a-Si:H layer. This leads to significant reduction of photo-induced damage in the blend, and thereby enhances photo-stability. Some photo-current is, however, lost due to absorption in n$^+$/a-Si:H. In order to overcome this drawback, we present a novel organic-inorganic hybrid tandem solar cell, in which blue photons are harvested by an a-(SiC):H front cell. A PTB7:PCBM$_{70}$ cell is used as the back cell. Our results demonstrate

a V_{OC} of 1.67 V, J_{SC} of 7.3 mA/cm^2 and overall efficiency of 7.6%, which is among the highest reported in the literature.

In the last part of this dissertation, we study the electronic properties of methyl-ammonium lead iodide perovskite solar cells. Capacitance spectroscopy shows the existence of a shallow (0.24 eV) and a deep (~0.62 eV) defect band in the bandgap. Moreover, we find that attempt-to-escape frequency is ~10^{11} Hz. The deeper defect band has a Gaussian distribution with a peak density of ~3×10^{16} cm^{-3}.eV^{-1}. Ideality factors and dark saturation currents indicate that band-to-band recombination is dominant at high excitation levels, and limits the photo-voltage.

CHAPTER I

INTRODUCTION TO SOLAR ENERGY AND SOLAR CELLS

1.1. Introduction: Photovoltaics

Among all renewable energy sources, solar energy has the highest theoretical potential for power production (~89000 TW). This great potential is reduced to a practical value of only a few thousand TWs due to geographical accessibility, which sets technical limitations on the amount of sunlight that can be harvested with current technology[1]. But even at this limited capacity, solar power is far more than enough to provide the global annual energy demand, which is of the order of 100000 TWh [2,3].

Solar Photovoltaics (PV) have the highest technical potential (~7500 TW) among other forms of solar power such as solar fuels and solar thermal energy[1]. Moreover, it offers minimal carbon footprint [4]. These advantages make PV systems center of attention in strategic research and planning. Fig. 1.1(a) and (b) show, respectively, the reduction in
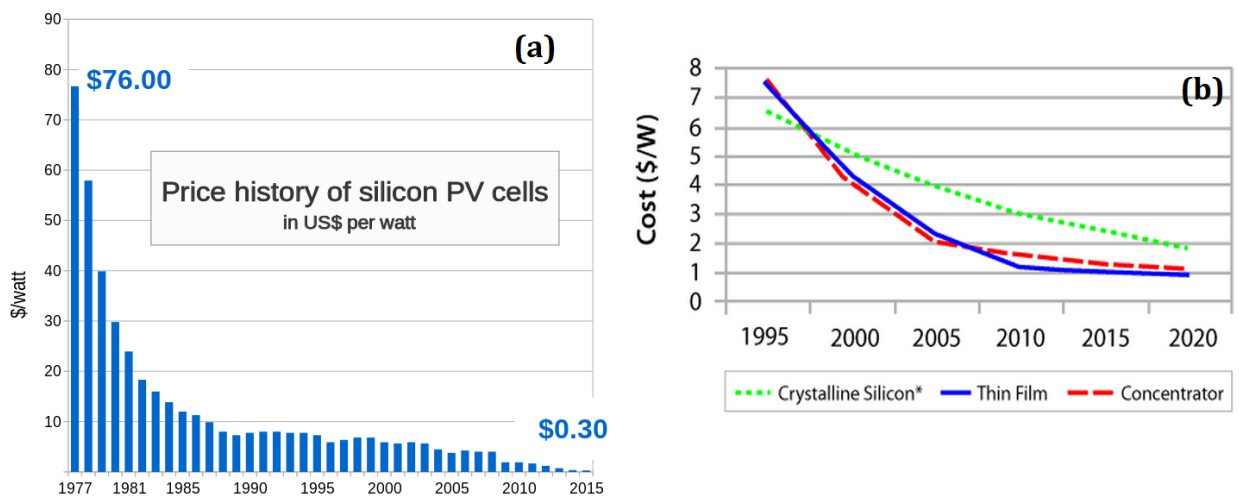
Fig. 1. 1. (a) Price history of silicon PV cells [5] , (b) Capital cost of PV systems in the past two decades [6].
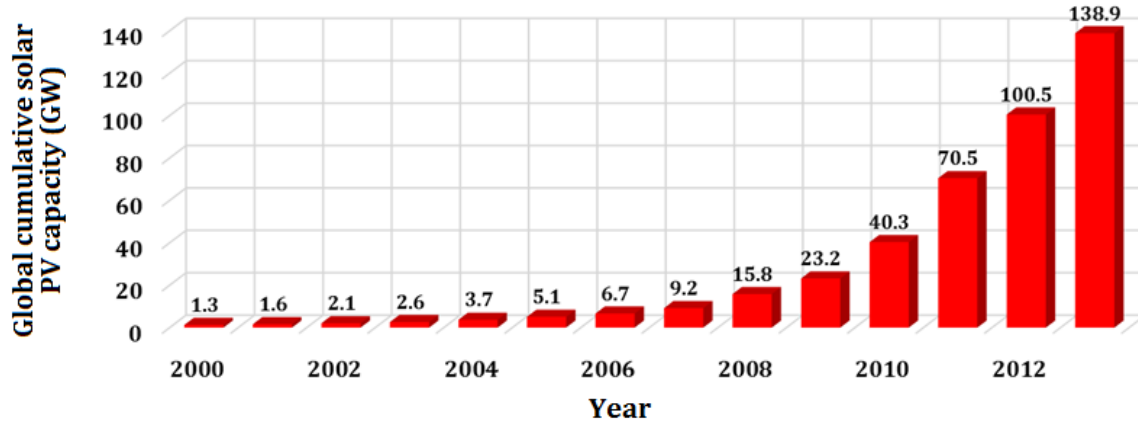
Fig. 1. 2. Global cumulative installed solar PV capacity [7].

price of silicon solar cells and capital cost of PV system over the past few decades. Accordingly, the cumulative global PV capacity has increased at a very rapid pace since the beginning of the millennium (Fig. 1.2.).

Despite this substantial growth, solar electricity is still considerably more expensive compared to electricity produced from traditional sources such as coal and natural gas (Fig. 1.3). This high price is mostly due to solar modules and Balance of System (BOS) (Fig.1.4), and has limited PV electricity generation to only ~1% of the annual global energy
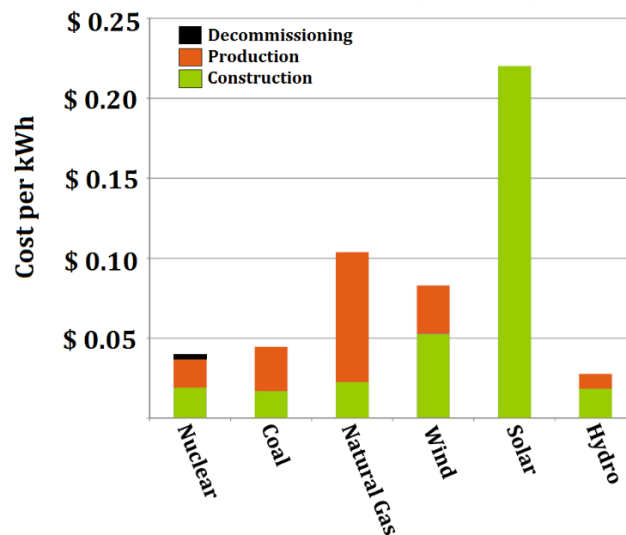
Fig. 1. 3. Cost of electricity for different energy sources [8].
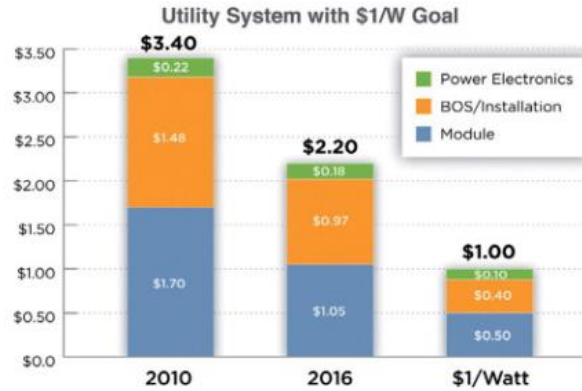
Fig. 1. 4. *Solar PV system costs by part* [9]. *The goal is to achieve $1/W by 2020.*

demand. For solar electricity to be competitive, the cost of solar panels and BOS should, therefore, be considerably reduced. Attempts are being made to cut these prices by 75% between 2010 and 2020 [10]. The current milestone, according to US Department of Energy's SunShot initiative, is to reduce the price of PV power to below $1/W by the end of 2020 [10,11].

Along these lines, a significant portion of research in solar community focuses on developing new photovoltaic materials that can be synthesized and deposited at low prices to make PV modules more affordable. Two very important classes of materials in this regard are "organic" and "hybrid organic-inorganic perovskite" semiconductors. A part of research at Iowa State University concentrates on synthesis and device characterization of solar cells based on these semiconductors.

1.2. Thesis structure

The first two chapters of this thesis are dedicated to describing the general operating principles of solar cells and characterization methods. In chapter 3, we narrow down to the field of Organic Photovoltaics (OPV). A recent high-performance polymer in

this field is PTB7. Chapter 4 is dedicated to exploring the device physics of PTB7-based solar cells, and reporting our results on fundamental electronic characteristics of PTB7:PCBM$_{70}$ bulk heterojunctions. We used capacitance spectroscopy technique to measure defect density, and subgap QE to identify tail states. Dark IV and Dark IV vs. temperature were used to identify recombination mechanisms in the device. Moreover, a multiple-level trap model is employed to compute recombination rates in the device, and explain ideality factors and dark saturation currents in PTB7 cells.

Based on the recombination model, we address the photo-stability issues of polymeric cells in chapter 5, and introduce a new device architecture with hybrid interfaces for improved light-stability. In the second part of chapter 5, we report a high-performance inorganic/organic tandem cell as an alternative for enhanced efficiency in hybrid cells.

The last chapter of this dissertation is dedicated to fundamental electronic properties and device characteristics of a new PV material: lead-halide perovskites cells.

1.3. Basic structures and processes in solar cells

A solar cell is a PN junction device for converting sunlight into electrical power. The basic structures of a solar cell is shown in Fig. 1.5. It consists of a light absorbing material (i-layer) sandwiched between a heavily n-doped (n$^+$ cathode), and a heavily p-doped (p$^+$ anode) film. Photons enter the cell through a semi-transparent contact, and are absorbed in the main layer, creating Electron/Hole Pairs (EHPs). The electrons are collected at the n$^+$ (i.e. the Electron Transport Layer or ETL), and the holes are collected at the p$^+$ (Hole Transport Layer or HTL). The collected carriers give rise to the current in the external
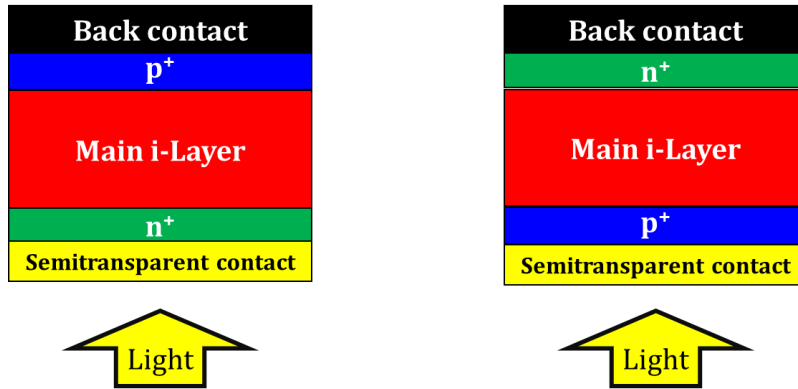
Fig. 1. 5. *Structure of single-junction n-i-p (left), and p-i-n (right) solar cells.*

circuitry. By convention, if the light is first incident on the n⁺, the structure is called an n-i-p cell. If, on the other hand, p⁺ is at the front side, the cell has a p-i-n structure.

Power Conversion Efficiency (PCE) is defined as the ratio of the output power to the input power of a cell (PCE=P_{out}/P_{in}), and primarily depends on the properties of light-absorbing material and the device structure. The latest efficiency chart (Fig. 1.6) published by the National Renewable Energy Laboratory (NREL) [12], provides insight into how the PCEs of different solar technologies have evolved over the past four decades.

As we indicated earlier, organic and perovskite solar cells are favorable for their potential low cost, light weight and ease of fabrication. As shown in Fig. 1.6, organic cells have been under research for more than two decades and have produced efficiencies up to ~11%. Perovskite solar cells, on the other hand, emerged on the chart about two years ago, and their efficiencies have already passed ~20%, which is comparable to the efficiency of best silicon cells (~26%). There is, therefore, great interest and excitement in solar research community to bring these cells to mass production.

Energy band diagram of Fig. 1.7 shows the basic operation of a crystalline silicon solar cell. The efficiency of the solar cell depends on two fundamental processes:
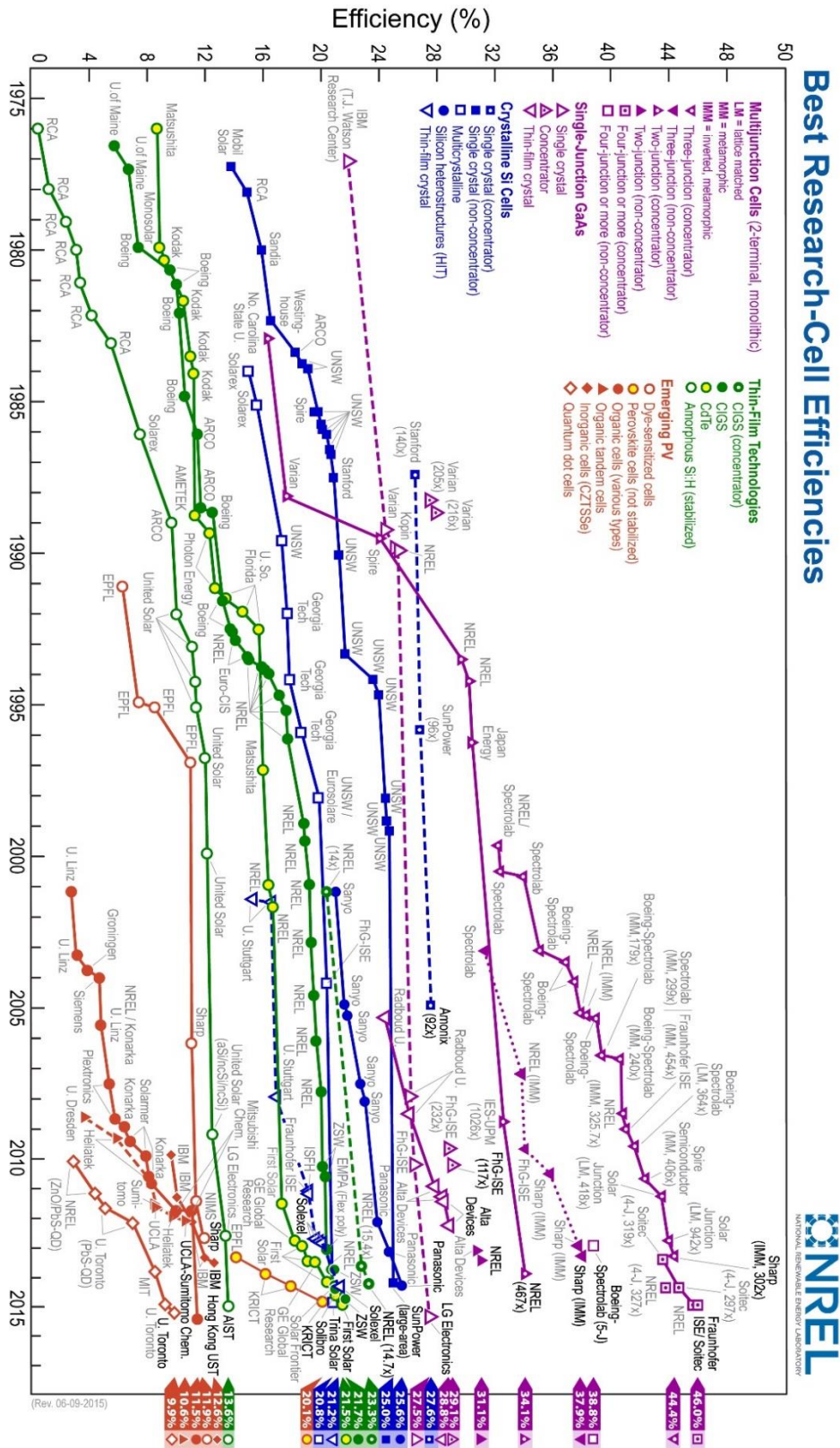
Fig. 1. 6. NREL efficiency chart (July 2015).
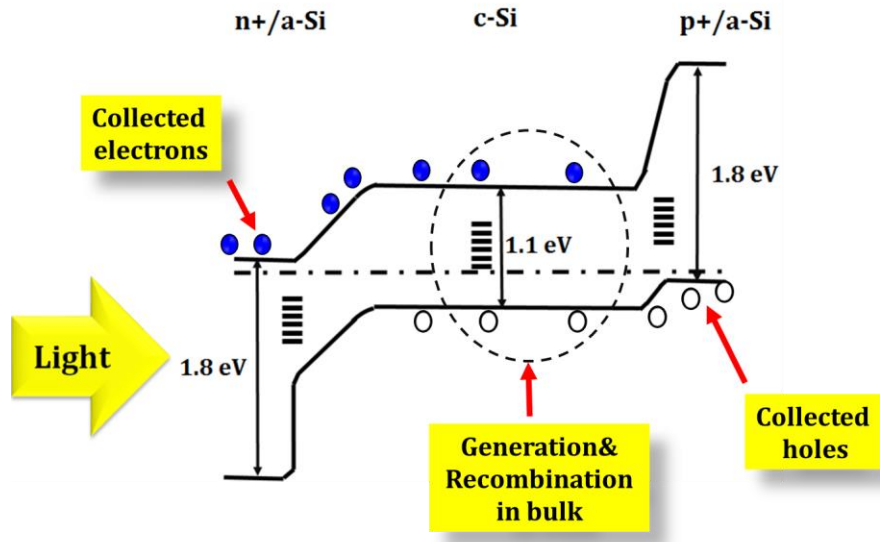
Fig. 1. 7. Energy band diagram of a crystalline silicon solar cell. In this figure the light-absorbing material is c-Si wafer, and a-Si forms HTL and ETL. Bulk generated charge carriers that diffuse to contacts are collected. Collection may be assisted by electric field.

(i)   Generation involves light absorption in the bulk of the main layer which leads to generation of charge carriers.

(ii)   Recombination is annihilation of charge carriers of opposite kinds. In order to achieve high efficiencies, it is essential that light-generated carriers get collected at the electrodes before they are recombined. The photo-generated carriers which are not lost to recombination are collected at the contacts, and give rise to the external current. Energy band diagram of Fig. 1.7 shows a sample heterojunction silicon (HIT) cell with n^+ and p^+ amorphous silicon (a-Si) as ETL and HTL, respectively. The carriers which are generated in the bulk escape recombination by diffusion and are collected at the contacts. In general, however, charge collection might be assisted by an internal electric field. In the following sections, we briefly discuss absorption of light, recombination of charge carriers, and then diffusion- and field-assisted collection.
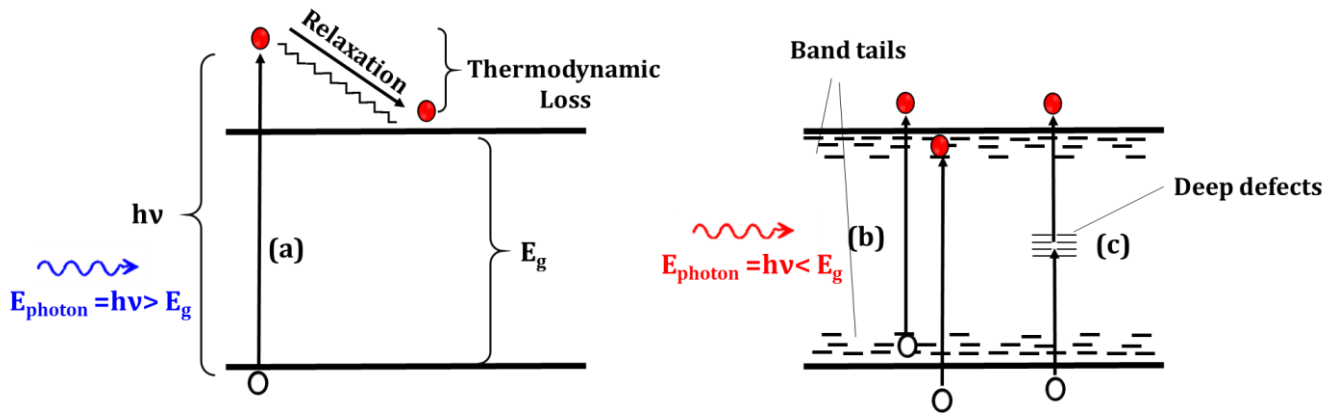
Fig. 1. 8. Absorption through (a) band-to-band transition, (b) tail state absorption, and (c) deep defects.

1.3.1. Absorption

When a photon of energy E=hν enters a material, it may excite an electron from a lower state to a higher state. Fig. 1.8. shows possible optical transitions, which lead to the generation of free charge carriers. If photon energy (hν) is greater than the bandgap, an electron is excited from the valence to the conduction band. The difference (hν-E_g) is dissipated in the form of heat as the excited electron relaxes to the bottom of the conduction band by losing energy to lattice collisions (thermodynamic loss) (Fig. 1.8. (a))[13]. If hν is less than E_g, electrons can still be excited through subgap transitions. This can occur through deep defects or via band tails[14,15]. The subgap transitions, however, do not significantly contribute to the charge carrier generation. This is due to the fact that deep defects and band-tail states have far less density compared to the extended band states. Much of the charge generation is, therefore, due to band-to-band absorption. Subgap transitions, however, provide valuable information about the material band structure, and are regularly used to obtain information about the distribution of deep defects and tail
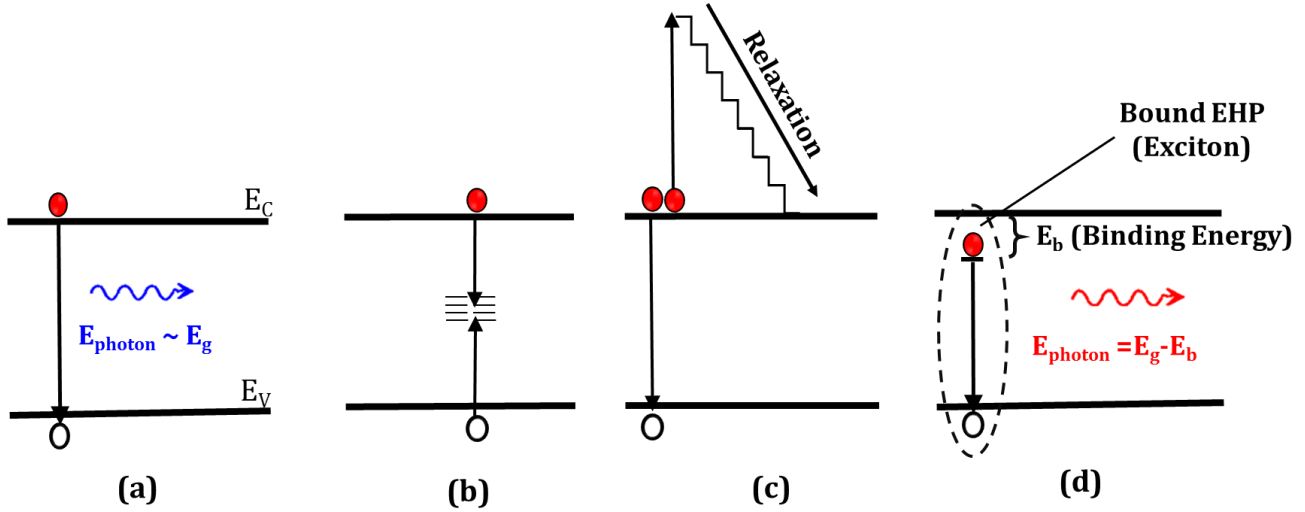
Fig. 1. 9. Recombination mechanisms (a) Band-to-band, (b) Trap-assisted, (c) Auger, and (d) Excitonic.

states [16,17,18]. As the light propagates in the sample its intensity drops exponentially due to absorption[19]:

$$I = I_0 . \exp(-\alpha x) \tag{1.1}$$

Where I is the intensity at distance x in the material, I_0 is initial light intensity, and α is absorption coefficient usually expressed in cm^{-1}. The inverse of absorption coefficient $(1/\alpha)$ is called absorption depth, and corresponds to the traveling distance over which ~63% of the initial photons get absorbed in the material.

1.3.2 Recombination

As mentioned previously, recombination is the process during which two charge carriers of opposite type annihilate each other. Energy is released in the form of photons (radiative recombination) or heat (non-radiative recombination) during this process. Four types of recombination are schematically shown in Fig. 1.9. : band-to-band, trap-assisted, Auger and excitonic. In this section, we briefly introduce these recombination mechanisms.

1.3.2.1. Band-to-band recombination[20,21]

In band-to-band recombination, an electron in the conduction band directly recombines with a hole in the valance band (Fig. 1.9(a)). Band-to-band recombination is typically radiative, i.e. the energy difference is released in the form of a photon. The recombination rate (R) can be expressed in the following form[20, 21]:

$$R = c_B(np - n_i^2) \qquad (1.2)$$

Where c_B is the band-to-band recombination constant (in cm^3/sec). "n" and "p" are electron and hole concentration (cm^{-3}), and n_i is the intrinsic carrier concentration (cm^{-3}). In a p-type material under small signal conditions:

(i) $p \gg n$, and $p \gg n_i$

(ii) $\Delta n, \Delta p \ll p$ where $\Delta n, \Delta p$ are excess carrier concentration

Eq. (1.2) reduces to:

$$R = c_B\left[(n+\Delta n)(p+\Delta p) - n_i^2\right] \approx c_B.\Delta n.p \triangleq \Delta n/\tau_{B-B} \qquad (1.3)$$

Where τ_{B-B} is the band-to-band recombination lifetime and is defined as:

$$\tau_{B-B} \triangleq 1/(c_B.N_A) \qquad (1.4)$$

$N_A \sim p$ is the density of acceptor atoms. Similarly, lifetime in an n-type material is inversely proportional to the concentration of donor atoms. *Carrier lifetime in band-to-band recombination is, hence, inversely proportional to doping level*.

1.3.2.2. Trap-assisted recombination [22]

Fig. 1.9 (b) shows how an electron from the conduction band, and a hole from the valence band may recombine through a trap state in the material bandgap. This is called trap-assisted or Schockley-Read-Hall (SRH) recombination. SRH recombination may occur

both in the bulk and at the interfaces. Interfacial SRH recombination obeys kinetics similar to that of bulk SRH. It is shown that the SRH recombination rate (R) obeys the following expression[22]:

$$R = \frac{np - n_i^2}{\tau_p(n+n_1) + \tau_n(p+p_1)}$$

(1.5)

Where τ_p and τ_n are, respectively, the hole and electron minority carrier lifetimes. "n" and "p" are carrier concentration, and n_i is the intrinsic carrier concentration. "n_1" and "p_1" are computable constants, and are approximately equal to electron and hole concentrations if the Fermi level was at the trap level (For details see ref. 22).

The minority carrier lifetimes are:

$$\tau_{n,p} = \frac{1}{c_{n,p} N_T}$$

(1.6)

Where N_T (cm^{-3}) is the concentration of defects. "$c_{n,p}$" are the electron and hole caption coefficients (cm^3/sec) , and are material constants.

For small signal conditions in a p-type material Eq. (1.5) reduces to:

$$R = \frac{\Delta n}{\tau_n} = c_n . \Delta n . N_T$$

(1.7-a)

Similarly, for an n-type material:

$$R = \frac{\Delta p}{\tau_p} = c_p . \Delta n . N_T$$

(1.7-b)

Rate of SRH recombination, therefore, depends *on minority carrier lifetime*. Moreover, it is *directly proportional to the concentration of electronic defects in the material*.

1.3.2.3.   Auger recombination[23, 24]

Auger is a non-radiative recombination process involving three bodies (carriers). This is schematically shown for Auger recombination of electrons in Fig. 1.9 (c). In this

scheme, the energy released from recombination is transferred to another carrier, and excites it to a higher state. The excited electron then relaxes to the bottom of conduction band through thermalization process. The recombination rate is shown to have the following format [23, 24]:

$$R = c \left(p.n^2 - n_i^2.n \right) \tag{1.8}$$

Where c is a constant, n and p are, respectively, electron and hole concentrations, and n_i is the intrinsic carrier concentration.

For an n-doped material in small signal (i.e. $p_0 \ll \Delta n \sim \Delta p \ll n_0 = N_D$) Eq. (1.8) reduces to:

$$R = c.N_D^2.\Delta p \triangleq \frac{\Delta p}{\tau_p} \tag{1.9}$$

Where N_D is the dopant density and τ_p is minority carrier lifetime, defined as:

$$\tau_p = 1/(c.N_D^2) \tag{1.10}$$

Hence, in Auger recombination carrier lifetime is inversely proportional to *the second power of doping concentration*. Hence, at very high doping levels (such as in the n^+ and p^+ layers of a solar cell), Auger recombination becomes the dominant source of loss[25].

The overall recombination rate of free charge carriers is the sum of various recombination mechanisms discussed above (band-to-band, trap assisted and Auger). The net carrier lifetime may, therefore, be determined by Matthiessen's rule[26, 27, 28]:

$$\frac{1}{\tau} = \frac{1}{\tau_{B-B}} + \frac{1}{\tau_{Trap}} + \frac{1}{\tau_{Auger}} \tag{1.11}$$

where τ_{B-B}, τ_{Trap} and τ_{Auger} are band-to-band, trap-assisted, and Auger recombination lifetimes, respectively.

1.3.2.4.   Excitonic recombination [24, 29]

The photo-generated Electron/Hole Pair (EHP) are not free charge carriers, but are bound to each through Coulombic attraction. This bound pair is called an "exciton". Because of the Coulombic force, the energy difference between the hole and the electron is less than the bandgap by E_b (binding energy). In the energy band diagram, therefore, an exciton is depicted as a temporary subgap energy level (Fig. 1.9(d)).

The binding energy of an exciton at n^{th} level is[30]:

$$E_b = -\frac{\mu}{m_0} \times \frac{1}{\varepsilon_r} \times \frac{R_H}{n^2} \tag{1.12}$$

Where μ is the reduced mass, m_0 is free electron mass, and R_H is Rydberg constant of hydrogen atom (=13.6 eV). ε_r in Eq. (1.12) is the dielectric constant of the material. In the case of traditional photovoltaic materials such as silicon, the dielectric constant is relatively high (ε_r=11.9 for silicon), leading to very low binding energy (E_b~15 meV)[31, 32]. This value is below the kT (26 meV at room temperature), which causes the excitons to thermally dissociate at room temperature in inorganic semiconductors[33].

In the case of organic semiconductors, on the contrary, ε_r is much lower (~2-5)[34] which causes high E_b (depending on the material from 0.2 eV to in excess of 1 eV)[35, 36,37]. In such cases, recombination of excitons is a significant course of carrier loss, and cannot be neglected in efficiency calculations.

1.3.3. Charge collection[38]

It is shown that for a pulse of excess carriers:

$$Ð\frac{\partial^2(\Delta n)}{\partial x^2} + \acute{\mu}.\varepsilon.\frac{\partial(\Delta n)}{\partial x} + G - R = \frac{\partial(\Delta n)}{\partial t} \tag{1.13}$$

This is called the ambipolar transport equation. Where $\mathcal{E}$ is the electric field, G and R are the generation and recombination rates, respectively. "x" is coordinates and "t" is time. $\acute{D}$ and $\acute{\mu}$ are ambipolar diffusion coefficient and mobility, respectively, and are defined by the following equations:

$$\acute{\mu} = \frac{\mu_n\mu_p(p-n)}{n\mu_n+p\mu_p} \tag{1.14}$$

$$\acute{D} = \frac{n\mu_n D_p + p\mu_p D_n}{n\mu_n + p\mu_p} \tag{1.15}$$

In these equations, μ_n and μ_p are electron and hole mobility, respectively. Likewise, D_n and D_p are diffusion coefficient of electrons and holes.

For a p-type material at low injection, the ambipolar equation reduces to:

$$D_n\frac{\partial^2(\Delta n)}{\partial x^2} + \mu_n.\mathcal{E}.\frac{\partial(\Delta n)}{\partial x} + G - \frac{\Delta n}{\tau_{no}} = \frac{\partial(\Delta n)}{\partial t} \tag{1.16}$$

A similar equation for can be derived for holes in an n-type material:

$$D_p\frac{\partial^2(\Delta p)}{\partial x^2} - \mu_p.\mathcal{E}.\frac{\partial(\Delta p)}{\partial x} + G - \frac{\Delta p}{\tau_{po}} = \frac{\partial(\Delta p)}{\partial t} \tag{1.17}$$

τ_{n0} and τ_{p0} are minority carrier lifetimes at low level injections, and are determined by the Eq. (1.11).

The important message of Eqs. (1.16) and (1.17) is *that the drift, diffusion and recombination rate of excess carriers is governed by minority carriers*. Therefore, the overall quality of charge collection in a solar cell depends on the transport of minority carriers.

1.3.3.1.   Diffusion-based collection

Now, consider a p-type sample of thickness t. Let's assume light enters at x=0, and gets absorbed in the vicinity of the surface, i.e. the absorption depth is much thinner than the sample (α^{-1}<<t) .

At steady state, for x>0⁺ Eq. (1.16) reduces to:

$$D_n \frac{\partial^2(\Delta n)}{\partial x^2} + \mu_n . \mathcal{E} . \frac{\partial(\Delta n)}{\partial x} - \frac{\Delta n}{\tau_{no}} = 0 \qquad (1.18)$$

In the absence of electric field (no drift), this will further simplify to:

$$D_n \frac{\partial^2(\Delta n)}{\partial x^2} - \frac{\Delta n}{\tau_{no}} = 0 \qquad (1.19)$$
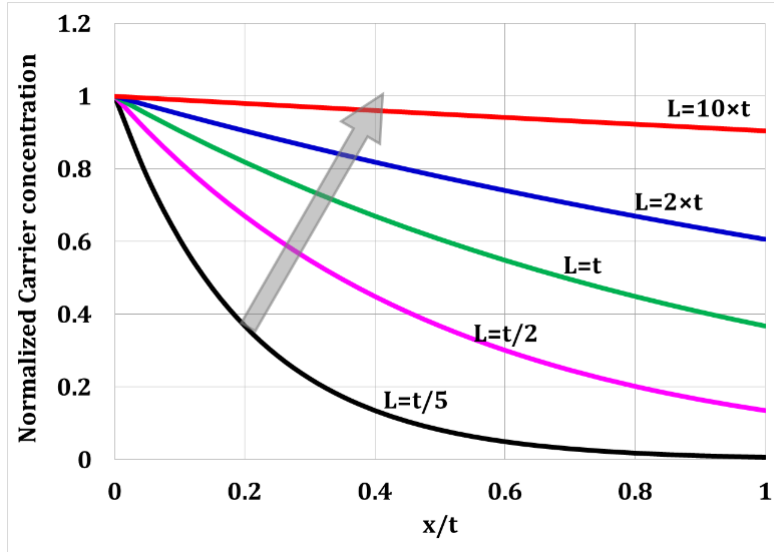
Fig. 1. 10. Carrier concentration as a function of L. L is carrier diffusion length in case of diffusion-based collection, and drift-length in case of field-assisted collection. The arrow indicates increase in L.

Which yields and exponential distribution of carriers (shown in Fig. 1.10) [39]:

$$\Delta n = \Delta n(x = 0) . \exp\left(-\frac{x}{L_n}\right) \qquad (1.20)$$

Where $L_n = \sqrt{D_n \times \tau_{n0}}$ is the electron diffusion length[27,39]. In this case, how well the carriers are collected at x=t depends on the relative size of the carrier diffusion length and sample thickness (Fig. 1.10). In crystalline solar cells, for example, where the carrier diffusion lengths are of the order of a few hundred μm, the sample could be made on wafers with similar thicknesses. The minority carrier diffusion length is large enough that the carriers could reach the contacts through diffusion only. This is depicted in the energy band diagram of Fig. 1.11.
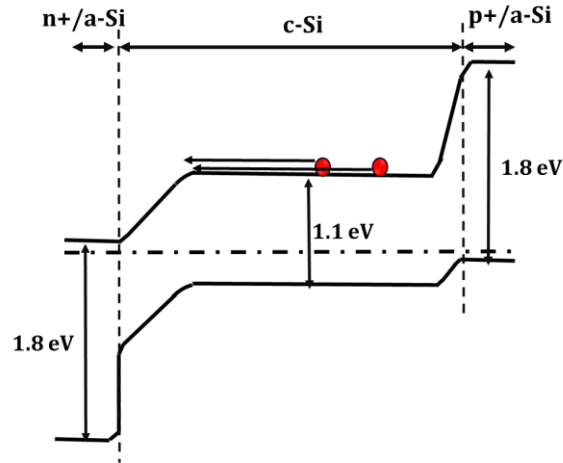
Fig. 1. 11. Diffusion-based collection in crystalline HIT silicon solar cells. The main layer of the device is a p-type silicon wafer. The minority carriers (electrons) reach the junction by diffusion and are collected.

1.3.3.2.   Field-assisted collection

For an n-type material, when carrier diffusion is negligible, Eq. (1.17) reduces to:

$$\frac{\partial(\Delta p)}{\partial x} - \frac{\Delta p}{\mu_p.\mathcal{E}.\tau_{po}} = 0 \tag{1.21}$$

Which gives rise to an exponential distribution of carriers:

$$\Delta p = \Delta p(x = 0).\exp\left(-\frac{x}{L_{p,DRIFT}}\right) \tag{1.22}$$

Where $L_{p,DRIFT}$ is the "drift length" or "range" of holes, and is defined as $\mu_p.\tau_{p0}.|\mathcal{E}|$ [40, 41]. A high carrier collection is thus achieved, if drift length is much larger than sample thickness (Fig 1.10).

A good example is amorphous silicon (a-Si:H), where the mobility-life time product of carriers is of the order of 10^{-8} cm^2/sec [42] . Consequently, carrier diffusion length is very small, and the device must be made thin enough (a few hundred nm) such that the depletion layer extends through-out the bulk of the device. This is shown in the band diagram of Fig. 1.12. The carriers are drifted toward the contacts by the built-in electric field of the device, and a high carrier collection is achieved. In the case of organic devices,

the samples must be even thinner (in the range of ~100 nm) as the mobility-life time

product is even smaller compared to a-Si, and is measured to be 10^{-11}-10^{-9} cm^2/sec[43, 44].

1.4. Schockley-Queisser (SQ) limit

The solar cell efficiency primarily depends on the material bandgap. For wide

bandgap semiconductors, poor absorption results in low efficiencies, while high
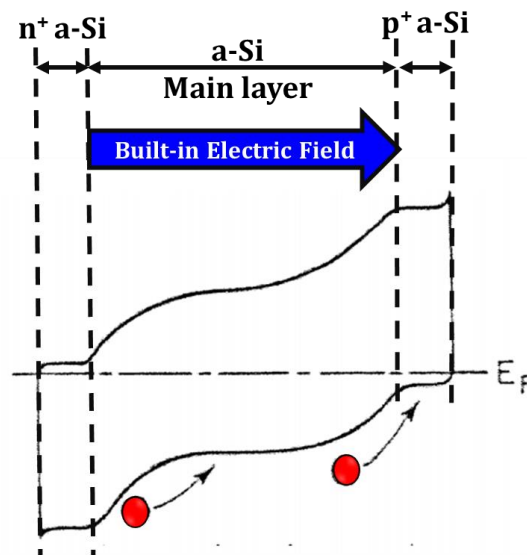
Fig. 1. 12. Field-assisted collection in thin film solar cells. The light-absorbing material is a-Si and the depletion layer is extended across the device. Minority carriers (in this case holes) are drifted by the built-in electric field and are collected at the p+ layer [45].

thermodynamic loss reduces performance when the bandgap is too narrow. Fig. 1.13

shows the maximum theoretical efficiency of a single junction solar cell as a function of its

bandgap[46]. These calculations are done in 1961 by Hans Queisser and William Schockley at

Schockley Semiconductors[47]. In their calculations, they assumed that the sources of loss are

limited to absorption loss, black body radiation, and radiative recombination. They showed

that the maximum achievable efficiency of a single junction cell is ~34% at E_g~1.34 eV.

In practice, however, various recombination losses and other non-idealities (such as parasitic series and shunt resistances) are present in the device, and push the performance below SQ limit. The NREL efficiency chart shows that for the best single junction cell, device performance does not exceed ~30%. Higher efficiencies are achievable by using tandem structures which will be discussed in chapter 5. In the case of organic cells, the presence of excitonic losses reduces the SQ limit to ~23% in the case of bulk heterojunctions[48]. The practical efficiency has, however, stayed as low as ~12% as depicted in Fig. 1.6.
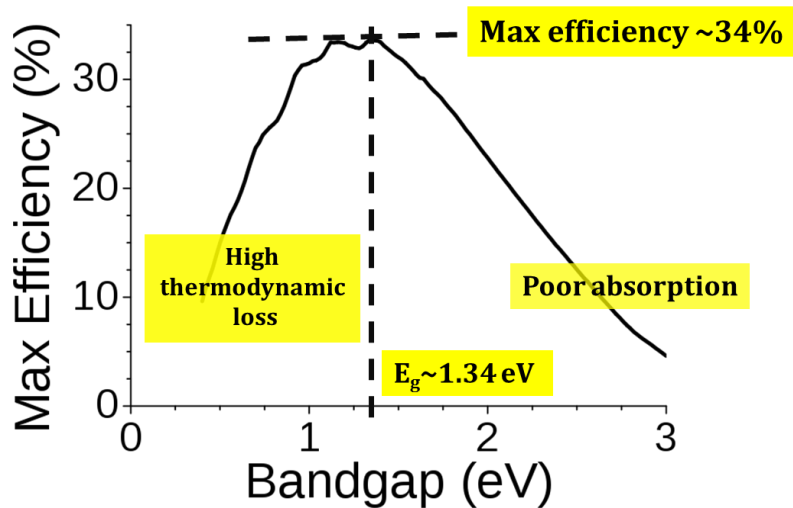
Fig. 1. 13. Schockley-Queisser (SQ) limit for single junction solar cells as a function of material bandgap[46].

1.5. Closing remarks

In this chapter, we had a brief look at the basic operating principles of solar cells, and discussed how optical absorption and transport properties such as mobility-life time product and carrier diffusion length affect device performance.

The next chapter is dedicated to device characterization techniques. In particular, we are interested in identifying parameters such as band tails and electronic defect

densities which play a key role in quantifying recombination and thus understanding device physics.

CHAPTER II
DEVICE CHARACTERIZATION TECHNIQUES

2.1. Introduction

Studying physics of photovoltaic devices entails measurement of cell performance and assessment of electronic and optical properties of the light-absorbing material. Among characterization methods are the light current-voltage (IV) and Quantum Efficiency (QE) measurements which assess device performance. Dark IV, on the other hand, evaluates the diode behavior of the cell, and provides insight into recombination rates, and carrier loss mechanisms under different bias conditions. Capacitance spectroscopy and subgap QE are helpful in explaining dark IV results by providing fundamental electronic properties of the material such as the Density of States (DOS) and Urbach energy. These parameters are also essential in recombination rate computations and ideality factor derivations, which help physicists understand and interpret the data.

Due to the electrical nature of our characterization techniques, we introduce the equivalent circuits of a solar cell in the next section. We then focus on explaining the above-mentioned characterization methods, and describe the theory behind them.

2.2. Equivalent circuit of a solar cell

The equivalent circuit of a solar cell is shown in Fig. 2.1(a)[49]. In this circuit, I_L is light-generated current. The diode represents bias-dependence of current loss due to recombination at the PN junction. R_{sh} and R_s are parasitic shunt and series resistances, and are, respectively, infinity and zero in an ideal solar cell. The collected current is:

$$I=I_L-I_D-I_{sh} \tag{2.1}$$
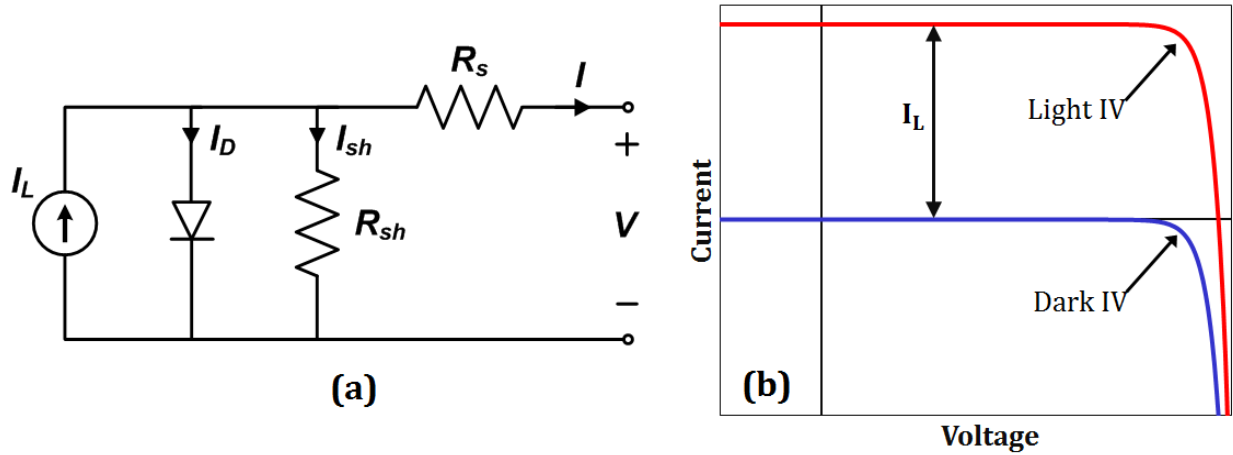
*Fig. 2. 1 . (a) Equivalent circuit of a solar cell with a single diode[49], and
(b) Corresponding light and dark IV characteristics for ideal case where R_s=0 and R_{sh}=∞.*

In which I_D is the diode current given by:

$$I_D = I_0 \left[\exp \left(\frac{V+IR_s}{nV_T} \right) - 1 \right] \tag{2.2}$$

Where I_0 is saturation current, n is ideality factor (typically a number between 1 and 2), and V_T is thermal voltage equal to 25.9 mV at 300 K. Current in Eq. (2.1) is therefore:

$$I = I_L - I_0 \left[\exp \left(\frac{V+IR_s}{nV_T} \right) - 1 \right] - \frac{V+IR_s}{R_{sh}} \tag{2.3}$$

In Fig. 2.1(b), this current is plotted as a function of voltage for an ideal solar cell where R_s~0 and R_{sh}→∞. In the absence of light (I_L=0), the dark IV curve reflects diode's characteristics (I=-I_D). When light is introduced, the curve shifts along the vertical axis by an amount equal to photo-current (I_L). Notice that, for convenience, we plot the photocurrent on +y axis.

The equivalent circuit of Fig. 2.1(a) and Eq. (2.2) estimate the dark current with a single ideality factor. In practice, however, the ideality factor changes with the applied voltage (discussed later), and more than one diode (typically 2) are needed in the equivalent circuit diagram to accommodate the bias dependence of ideality factor.
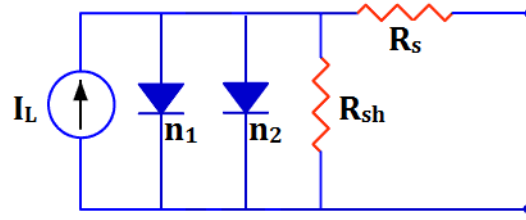
Fig. 2. 2. Double-diode equivalent circuit of a solar cell. n_1 and n_2 are ideality factors of the diodes[50].

In such case, current through the cell is given by:

$$I = I_L - I_{01}\left[\exp\left(\frac{V+IR_s}{n_1.V_T}\right) - 1\right] - I_{02}\left[\exp\left(\frac{V+IR_s}{n_2.V_T}\right) - 1\right] - \frac{V+IR_s}{R_{sh}}$$ (2.4)

where n_1 and n_2 are ideality factors, and I_{01} and I_{02} are saturation currents. Fig. 2.2 shows the corresponding double-diode model for a solar cell[50].

In the next section, we explain how to measure, analyze and interpret IV characteristics of a solar cell based on the equivalent circuit models and the diode equations.

2.3. Current-Voltage (IV) measurements

In IV measurements, the voltage across the sample is varied over the desired range, and the corresponding current values are recorded. This could be done under illumination (light IV), or in the absence of light (dark IV) (Fig. 2.1(b)). In this section, we first discuss light IV characteristics, and then explain our approach in analyzing and interpreting dark IV data.

2.3.1. Light IV characteristics[51,52]

For a great part of this work, light IV is measured under illumination from a class C solar simulator (an ELH light bulb)[53] set at 1X sun intensity. The light IV characteristics of a
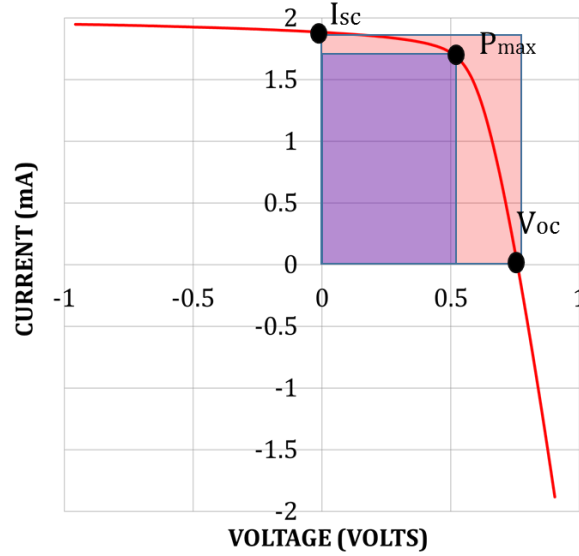
Fig. 2. 3. Light IV characteristic of a solar cell under illumination from an ELH bulb set at 1X sun intensity. Device area is 0.106 cm². For this cell V_{OC}=0.76 V, I_{SC}=1.88 mA, FF=64%, R_s≈77Ω, and R_{sh}≈10.5 kΩ [54].

sample solar cell is shown in Fig. 2.3. The Power Conversion Efficiency (PCE) of the device is calculated through the following expression:

$$\text{PCE} = \frac{V_{OC} \times J_{SC} \times FF}{P_{in}}$$ (2.5)

Where P_{in} is incident power, and is set at ∼100 mW/cm² (∼1 X sun intensity). V_{OC} is the open circuit voltage, J_{SC} is the short circuit current density (mA/cm²), and FF is the fill factor defined as:

$$FF = \frac{P_{max}}{V_{OC} \times J_{SC}}$$ (2.6)

P_{max} is the maximum output power as shown on Fig. 2.3.

For the IV curve shown in Fig. 2.3, V_{OC} is ∼0.76 V, J_{SC} is 17 mA/cm², and FF is 65%, which yield a PCE of ∼8%. It is customary to plot current density instead of current, to count for the device area. In that case the graph is called a J-V characteristic.
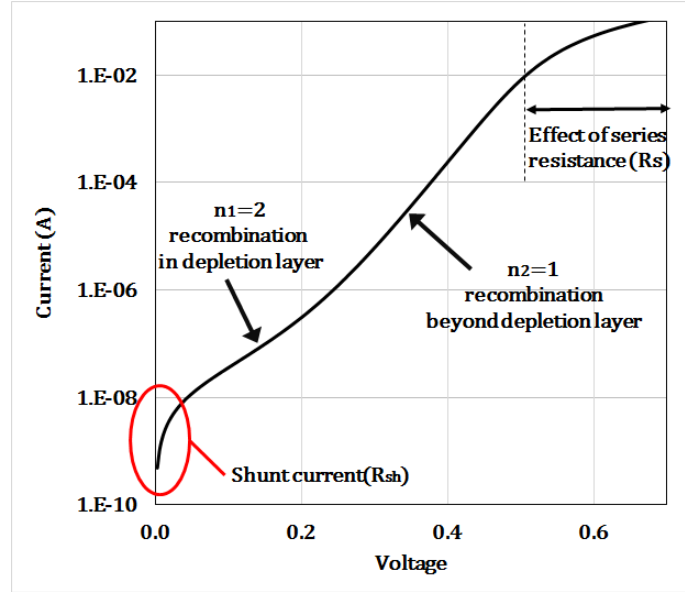
Fig. 2. 4. Dark IV of a silicon PN junction. For this diode: $I_{01}=4\times10^{-9}$ A, $n_1=2$, $I_{02}=4\times10^{-11}$ A, $n_2=1$, $R_{sh}=10^7\Omega$ and $R_s=1$ Ω for a device area of 0.1 cm^2 [50].

2.3.2. Dark IV characteristics

In dark IV measurements, the diode behavior of the cell is probed. With $I_L=0$ in the dark, Eq. (2.4) reduces to:

$$I_{Dark} = I_{01}\left[\exp\left(\frac{V+IR_s}{n_1.V_T}\right)-1\right] + I_{02}\left[\exp\left(\frac{V+IR_s}{n_2.V_T}\right)-1\right] + \frac{V+IR_s}{R_{sh}} \qquad (2.7)$$

The corresponding dark current for a standard silicon PN junction is depicted on a semi-log scale in Fig. 2.4. At very low voltages, shunt current (through R_{sh}) is dominant. This is normally due to unwanted shunt paths or pinholes in the device. As the voltage increases, the current continues to go up exponentially, until very high current values where the voltage-drop across series resistance (R_S) becomes significant, and limits the current. In such high biases, the dark IV curve bends and deviates from exponential behavior.

Ideality factors are obtained from the slope of dark IV in the exponential regimes, and are characteristics of dominating recombination mechanisms. In the standard junction

of Fig. 2.4, for example, recombination is dominated by depletion layer at low biases, giving rise to an ideality factor of 2. Depletion layer width, however, shrinks at higher biases, and band-to-band recombination in the electrically neutral bulk becomes significant, leading to an ideality factor is 1 [55, 56]. Similarly, ideality factors can be derived for other recombination mechanisms. It is shown, for instance, that Auger recombination has a characteristic ideality factor of 2/3 [57,58], and high carrier injection levels result in an ideality factor of 2 [57, 59].

In addition to ideality factors, dark IVs provide us with saturation currents (I_{01} and I_{02}), which are metrics of recombination rates for their corresponding loss mechanisms at zero bias. Saturation current is related to recombination rate through[58]:

$$I_0 = \int_{over\ t}^{at\ V=0} R(x).dx \qquad (2.8)$$

Where R is recombination rate, V is applied bias, x is coordinates, and t is the device thickness. Dark IV is, therefore, a very powerful diagnostic tool, and its accurate measurement and analysis provides valuable insight into recombination rates and loss mechanisms in the device.

2.4. External Quantum Efficiency (EQE)[60,61,62,63]

EQE of a solar cell at a given wavelength (λ) is defined as the ratio of collected carriers to the number of incident photons at that wavelength:

$$EQE\ (\lambda) = \frac{\#\ of\ collected\ carriers\ (\lambda)}{\#\ of\ incedent\ photons(\lambda)} \qquad (2.9)$$

This quantity (hereafter referred to as QE) shows how efficiently photons are harvested by the device as a function of photon energy, and is, therefore, a very important metric of solar cell performance. We, hence, dedicate this section to explain the QE measurement method.

First, a monochromatic beam with desired wavelength (λ) is created. The photon flux of the beam is evaluated by measuring the response of a reference cell. This reference is typically a silicon solar cell or a photodiode whose QE at λ is known. Afterwards, sample's signal is measured, and the QE is obtained by comparing signals from the sample and the reference:

$$\text{QE of sample } (\lambda) = \frac{\text{Signal from sample } (\lambda)}{\text{Signal from reference} (\lambda)} \times \frac{\text{Area of reference cell}}{\text{Area of sample}} \times \text{QE of reference } (\lambda) \quad (2.10)$$

Fig. 2.5 shows the QE measurement setup. White light from a halogen bulb enters a monochromator where it hits a diffraction grating. By appropriately setting the incidence angle of the white light (θ_i), the desired wavelength is separated from the rest of the diffracted light through a slit at the end of the monochromator. The DC light that comes out of the slit is converted to a.c. (13 Hz) using an optical chopper. A lens is used to collimate
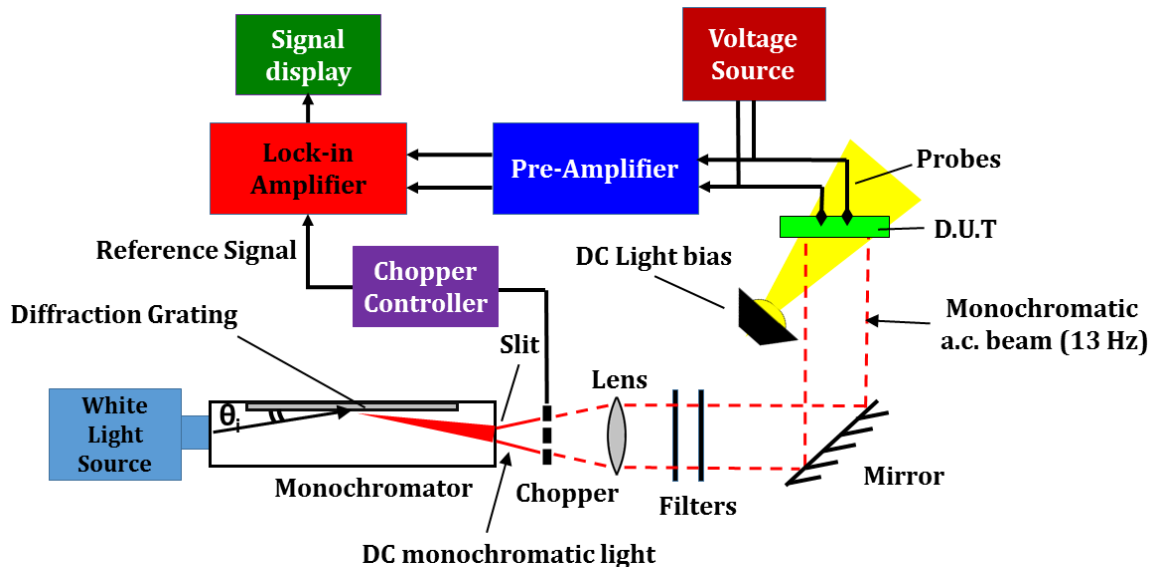
Fig. 2. 5. QE measurement setup. DUT is the sample or the reference cell.
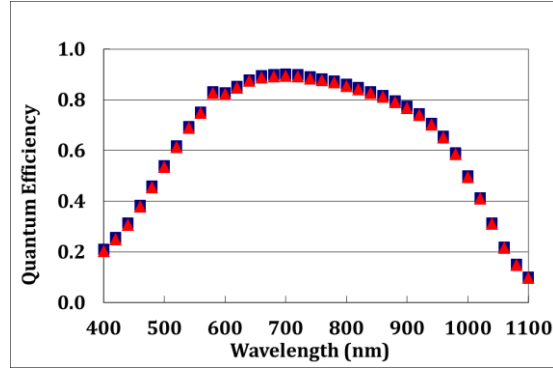
Fig. 2. 6. Sample QE of a crystalline silicon solar cell measured between 400 to 900 mn.

the chopped light and form an a.c. beam, which is then directed onto the Device Under Test (D.U.T) using a mirror. Unwanted harmonics caused by higher orders of diffraction in the monochromator are suppressed by order-sorting filters. Signal from the DUT is collected by the probes and is fed into a pre-amplifier. A lock-in amplifier, which is synchronized with the chopper through a reference signal, isolates DUT's response to the beam from the unwanted signals in pre-amplifier output. Such undesired signals are caused by ambient light, and electromagnetic noise/interference in the surroundings. DUT's response to the beam is displayed on the signal readout by the lock-in amplifier. A voltage source and a separate DC light source are also provided, and enable us to measure DUT under different voltage and light biases. A sample QE for a crystalline silicon solar cell is shown in Fig. 2.6.

2.5.   Subgap Quantum Efficiency

Fig. 2.7 shows density of electronic states as a function of energy in a semiconductor with energetic disorder[64]. The extended band states are separated from each other by an energy gap. Exponential tail states penetrate from the band edges towards the middle of the gap where deep localized defects are dominant. Knowing parameters such as the
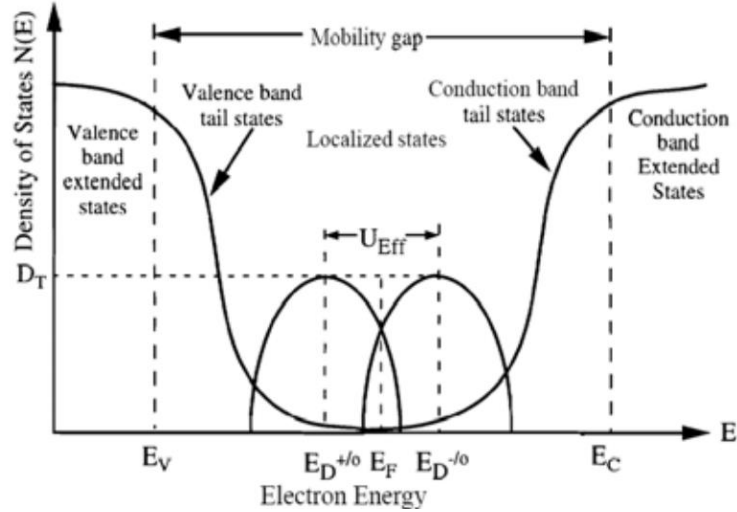
Fig. 2. 7. Density of electronic states in a material with energetic disorder. The tail states are distributed exponentially, and there are Gaussian peaks of deep defects in the mid-gap region.

energy band gap and energetic disorder (distribution of tail states) is essential in gaining insight into device physics. These parameters can be obtained by careful measurement of QE and absorption coefficient (α) at the onset of absorption. In this section, we discuss these measurements and show how to extract the above-mentioned parameters for the materials under study.

A widely-used solar material with distribution of electronic states similar to the one in Fig. 2.7 is hydrogenated amorphous silicon (a-Si:H). Fig. 2.8 shows the absorption coefficient of an a-Si:H sample as a function of photon energy [65]. As the energy of the incident photon falls below the gap energy, absorption coefficient changes according to the possible optical transitions (inset). Three distinct regions are observed in Fig. 2.8:

(a)   This region is due to transitions from extended valance band states to conduction band states. The absorption coefficient (α) obeys the following form[66, 67,68] :

$$(\alpha h \nu)^{1/m} = A(h \nu - E_T) \tag{2.11}$$
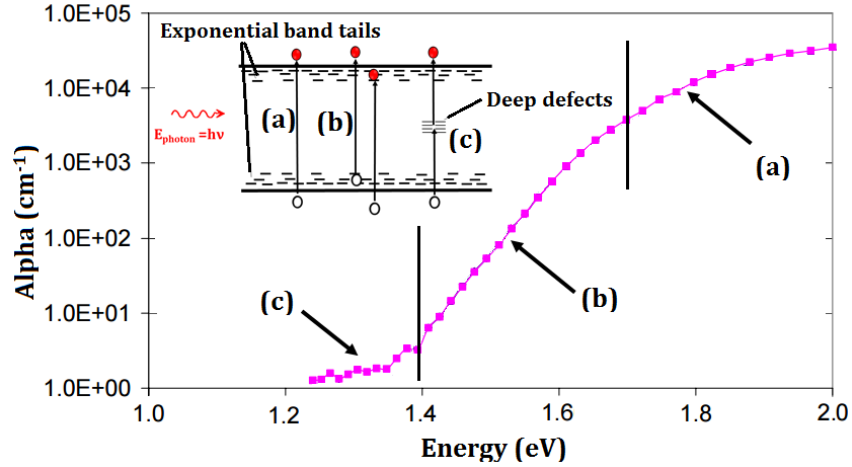
Fig. 2. 8. Absorption in a-Si:H due to: (a) Band-to-band transitions, (b) tail-to-band transitions, and (c) transition through deep defects. Intersection between (a) and (b) is the bandgap (~1.7eV), and slope of region (b) yields an Urbach energy of ~45 meV.

Where A is a constant, hv is the photon energy and E_T is the optical or "Tauc" bandgap. "m" is 2 for indirect and 0.5 for direct bandgap materials. By plotting $(\alpha hv)^{1/m}$ vs. $(hv - E_T)$ one can determine the value and type of the bandgap. The bandgap of a-Si:H sample shown in Fig. 2.8 is ~1.7 eV. It should be noted, however, that the exact bandgap of a-Si:H is very sensitive to growth conditions, and can vary over at least the range of 1.6 eV to 1.8 eV depending on the hydrogen content[69]. Alloying a-Si:H with other elements such as Ge or C can also, respectively, narrow or widen the optical bandgap[70].

(b)   In this region, α drops exponentially with decrease in photon energy due to the exponential distribution of tail states[71, 72]:

$$\alpha = \alpha_0 . \exp\left(-\frac{E_g - hv}{E_0}\right) \qquad (2.12)$$

Where α_0 absorption in the band-edge, hv is photon energy, and E_g is material band gap. E_0 is called Urbach energy, and shows how broadly the tail states are distributed inside the bandgap. For the sample shown in Fig. 2.8, E_0 is roughly 45 meV.

(c)   At very low energies (E<1.4 eV), the transitions through deep defects dominate, and
        cause the curve to plateau.

In order to find bandgap and Urbach energies, we first measure QE at wavelengths close to and below the bandgap. As discussed in section 1.3.3, under appropriate bias conditions, carrier diffusion/drift length is much larger than the sample thickness, and all light-generated carriers are collected at the contacts. In such case, QE is limited by absorption, particularly at the band edges where α is an exponential function of energy [73,74]:

$$QE = (1-R)(1-e^{-\alpha t}) \tag{2.13}$$

where α is absorption coefficient, t is sample thickness, and R is reflection from the sample. Hence, absorption coefficient is obtained from QE as:

$$\alpha = -\frac{1}{t} \times Ln\left(1 - \frac{QE}{1-R}\right) \tag{2.14}$$

Fig. 2.8. is actually derived from the subgap QE spectra of an a-Si:H sample using Eq. (2.14). It should be noted that since at subgap wavelengths αt<<1, Eq. (2.13) reduces to:

$$\alpha \approx \frac{QE}{t(1-R)} \tag{2.15}$$

which means that the slope of Ln(QE) vs. Energy also provides the Urbach energy.

The measurement and data analysis method we explained here can be applied to any material. In some cases, however, instead of a homo-junction, a type II heterojunction is used for charge generation (e.g. organic bulk heterojunctions-discussed in the next chapter). The subgap QE spectra for such junctions are shown in Fig. 2.9 [75]. There are four distinguished regions due to: (1) Bulk absorption, (2) band-to-band and (3) band-to-tail charge transfers (CT), and (4) CT through deep defects. These transitions are shown in the

band diagrams of Fig. 2.9(b). The deflection point between the band-to-band CT and exponential absorption tails is the interfacial bandgap of the heterojunction ($E_{g, int}$). Urbach energy of tail states is extracted from the slope of region (3).
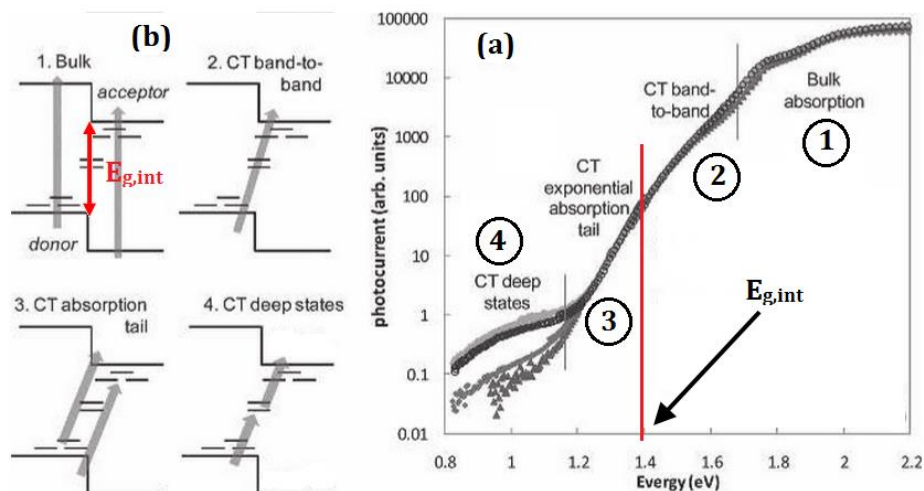
Fig. 2. 9. Subgap spectra of a type II heterojunction (a), and corresponding energy band diagram for each region (b). The gray arrows show the routes for Charge Transfer (CT) in each region.

2.6. Capacitance vs. Frequency (CF)

In CF measurements, the capacitance of a sample is measured in the dark as a function of frequency to assess the energetic distribution of electronic defects in its bandgap. This information, as we discussed in chapter 1, is useful in estimating carrier life-times in trap-assisted recombination, and proves critical in recombination rate computations and understanding photo-degradation mechanisms of organic cells in chapter 4.

The emission rate of electrons from a gap state into conduction band obeys the following equation[76, 77]:
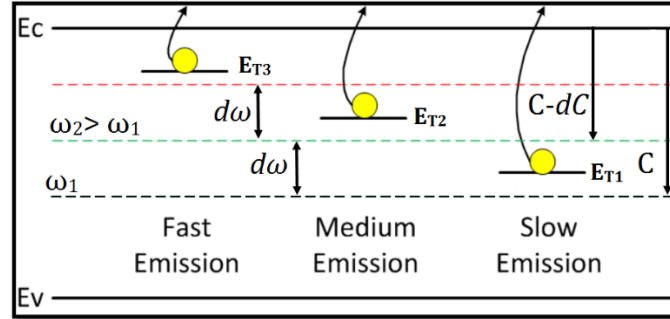
Fig. 2. 10. Shallow traps have very fast emission rate and therefore contribute to the measured capacitance at high and low frequencies. Deeper trap have low emission rate and respond to the input at lower frequencies.

$$e_n = \nu_0 \times \exp\left(-\frac{E_C - E_T}{kT}\right) \qquad (2.16)$$

Where e_n is the emission rate, E_C is the edge of the conduction band, E_T is the energy level of the trap, k is the Boltzman constant, and T is temperature in Kelvin. ν_0 is called the "Attempt To Escape Frequency" (ATEF), and is a material constant in the range of $10^{11} \text{-} 10^{12}$ Hz for a-Si:H [78, 79].

Eq. (2.16) has important implications, which form the basis of capacitance spectroscopy. First of all, emission rate drops exponentially as the trap's depth (E_C-E_T) increases (Fig. 2.10 [80]). When capacitance is measured at frequencies less than the emission rate of deep traps (ω_1), gap states (E_{T1}, E_{T2} and E_{T3}) respond to the applied signal and contribute to the measured capacitance (C). As the input frequency increases ($d\omega$), deeper traps (E_{T1}) with relatively slower emission rates cannot respond to the applied signal, and therefore the measured capacitance will decrease (C-dC). The slope of capacitance vs. frequency (dC/df) is, hence, negative and is directly proportional to the population of traps that are deactivated by increase in frequency. It is shown that the Density Of States (DOS) is calculated by taking the derivative of capacitance with respect to frequency[81, 82, 83]:
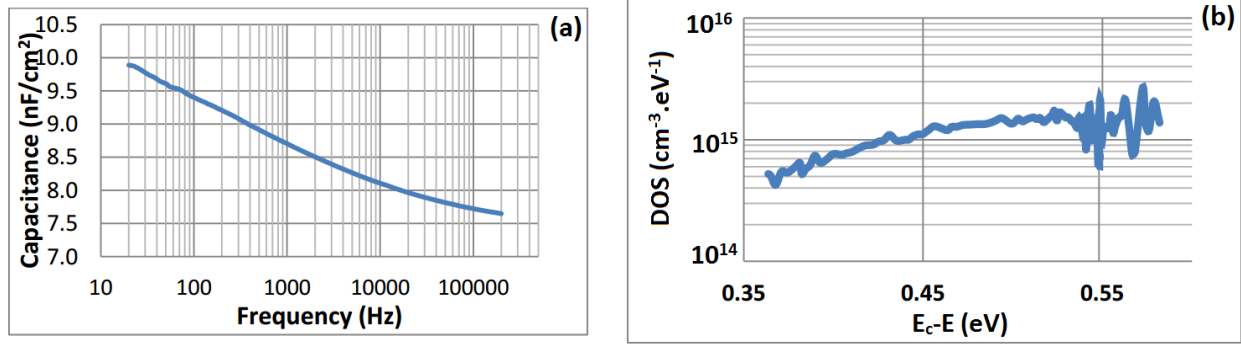
Fig. 2. 11. (a) Capacitance vs. frequency, and (b) Corresponding DOS for a nc-Si cell.

$$g(E) = -\frac{V_{FB}}{qw\,k_BT} \cdot \frac{d\,C(\omega)}{d\,Ln(\omega)} \tag{2.17}$$

Where g(E) is DOS, C is capacitance, ω is angular frequency, V_{FB} is the flat-band voltage of the cell, "w" is the depletion layer width, k_B is Boltzman constant, and T is temperature in degrees Kelvin. E in Eq. (2.17) is energy (in eV), and is related to the applied frequency by the following expression:

$$E_\omega = \frac{k_BT}{q}\,Ln\left(\frac{\omega_0}{\omega}\right) \tag{2.18}$$

Where ω_0 is angular ATEF ($2\pi\nu_0$). E_ω is referenced with respect the band edge (E_C in case of an n-type materials, and E_V in case of a p-type materials). Fig. 2.11 shows an example of CF curve for a nano-crystalline silicon (nc-Si) solar cell and its corresponding DOS [84].

Another important implication of Eq. (2.16) is that higher temperatures activate carrier emission from deep defects. A good example in this regard is depicted in Fig2.12[85]. Fig. 2.12(a) shows the capacitance of an a-Si:H solar cell between 20 Hz to 200 kHz at different temperatures. As temperature is stepped up, emission from deeper defects contribute to the measured capacitance. Consequently, the slope of CF curve increases at elevated temperatures, and the energy window that is being examined by CF shifts towards
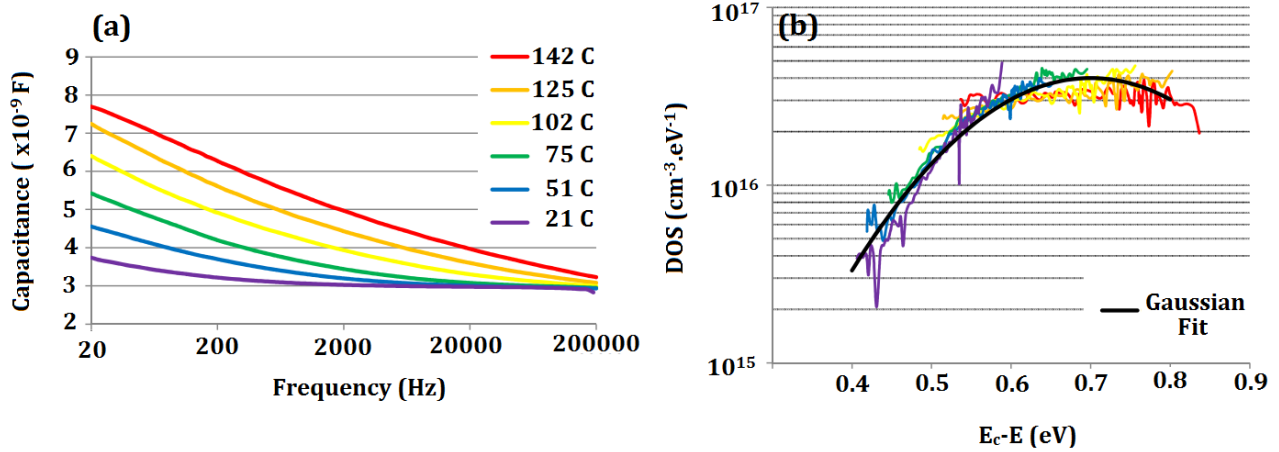
Fig. 2. 12. (a)Capacitance vs. frequency at different temperatures on an a-Si:H cell, and (b) corresponding DOSs concatenated together. The solid line is a Gaussian fit showing that the sample has a peak in trap density ~0.7 eV below E_c.

mid-gap region. Calculating DOS at each window, and concatenating the results yield energetic distribution of traps over a 0.4-eV-wide energy window (Fig. 2.12(b)).

By conducting CF measurements at different temperatures we can also obtain parameters such as the ATEF and activation energy of defect bands. This will be discussed in section 2.8.

2.7   Capacitance vs. Voltage (CV)

We use CV measurements to estimate dopant density and depletion layer width in our samples. This is particularly needed in analyzing CF results (Eq. 2.17). For a PN junction the depletion layer capacitance (per unit area) is (See, for instance, refs 86, 87, 88):

$$C_{dep} = \frac{\varepsilon}{W_{dep}} = \sqrt{\frac{q.\varepsilon.N_D}{2.(V_{bi}+V_r)}} \qquad (2.19)$$
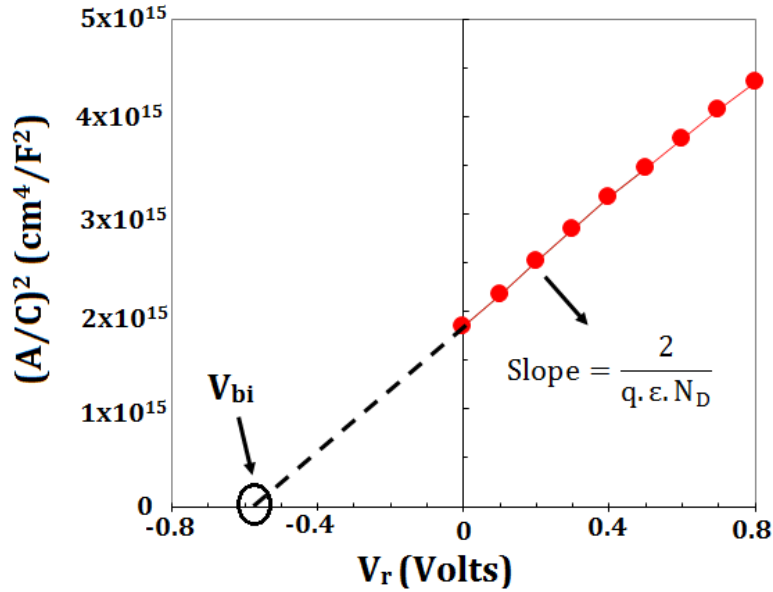
Fig. 2. 13. CV data for a crystalline silicon solar cell. The intercept gives a built-in potential of ~0.6V, and from the slope we find that the wafer doping level is ~4×10^{15} cm^{-3}.
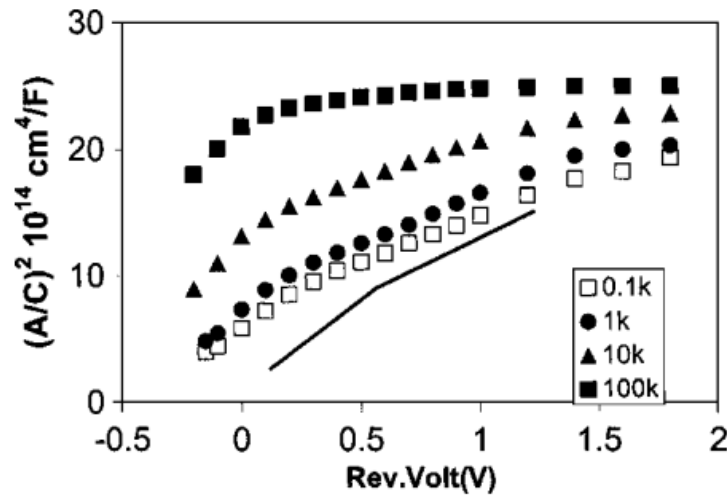
Fig. 2. 14. CV data for a nc-Si solar cell at different frequencies. The solid line is guide to the two slopes of the curves. The slopes yield N_D=1.6x10^{16} cm^{-3}, and a N_T=9x10^{15} cm^{-3}.

Where W_{dep} is depletion layer width, ε is permittivity, N_D is doping density, V_{bi} is built-in voltage, and V_r is the applied reverse voltage. Hence:

$$\frac{1}{C^2} = \frac{2}{q.\varepsilon.N_D} (V_{bi} + V_r)$$

(2.20)

The slope of $1/C^2$ vs. voltage, hence, yields doping density, and its intercept with horizontal axis yields built-in voltage. This is shown for a crystalline silicon solar cell in Fig. 2.13 [89].

In practice, the slope of $1/C^2$ vs. voltage is not always fixed with the applied bias. Fig. 2.14 shows CV data on a nano-crystalline silicon (nc-Si) solar cell at different frequencies[90]. There are clearly two distinct regions in this data set. Kimerling [91] showed that the slope at low reverse bias yields the density of shallow defects (i.e. N_D). At higher reverse bias, on the other hand, deeper defects (N_T) are activated, and the slope of the curve measures N_D+N_T. By carefully analyzing both regions and subtracting the results, one obtains both dopant density (N_D) and total density of deep defects (N_T).

At very high frequencies (e.g. 100 kHz in Fig 2.14), deep traps do not contribute to the measured capacitance due to their low emission rate. In such cases, as we go to higher reverse bias the device becomes fully depleted, and capacitance saturates. Under such circumstances, the measured capacitance is equal the geometrical capacitance of the device:

$$C = \varepsilon \frac{A}{t} \tag{2.21}$$

Knowing the device area (A) and permittivity (ε) of the material, one can therefore get an estimate of the i-layer thickness (t) by measuring device capacitance in reverse bias at high frequencies.

Overall, careful capacitance measurements under different bias conditions at various frequencies provide us with important characteristics such as doping level, total density of defects, built-in potential, depletion layer width, and thickness of the main layer.

2.8. CF vs. Temperature measurements (CFT)

There are two important unknowns in Eq. (2.16) that need to be assessed for material under study. One is the attempt-to-escape-frequency (ATEF), and the other is the trap activation energy (E_C-E_T). We use CFT to extract these parameters.

We know that ATEF is given by (See, for example, refs 92 and 93) :

$$\nu_0 = N_C \times v_{th} \times \sigma_n \tag{2.22}$$

Where N_C is the effective density of states in conduction band, v_{th} is thermal velocity, and σ_n is the capture cross section of the trap. Since $N_C \propto T^{3/2}$ [94,95] and $v_{th} \propto T^{1/2}$ [96], one can write:

$$\nu_0 = \xi \times T^2 \tag{2.23}$$

Where ξ is a constant, and we call it pre-factor. By plugging the above relation into Eq. (2.16) and taking the natural log of both sides, one obtains:

$$Ln\left(\frac{e_n}{T^2}\right) = Ln(\xi) - \frac{E_A}{kT} \tag{2.24}$$

Where E_A is the activation energy (=E_C-E_T). $Ln(e_n.T^{-2})$ vs. $(kT)^{-1}$ is, therefore, an Arrhenius plot whose slope is the activation energy. Moreover, the intercept yields the pre-factor, which can be used in calculating ATEF at any given temperature. Figs. 2.15(a) shows raw CFT data for a P3HT-based polymeric solar cells[97]. Here, a cryogenic stage was used to step down sample's temperature from 296 K to 112K in 12 steps. CF was measured at each step from f_{low}=20 Hz to f_{high}=1 MHz. In Fig. 2.15(b), $f \times dC/df$ is plotted versus frequency at each temperature. The peak frequency (f_{peak}), which corresponds to the emission rate from a defect band (e_n), shifts to lower frequencies as the temperature is stepped down.

In Fig. 2.16, $Ln(f_{peak}/T^2)$ is plotted vs. 1/T. By fitting Eq. (2.24) to these data points, one
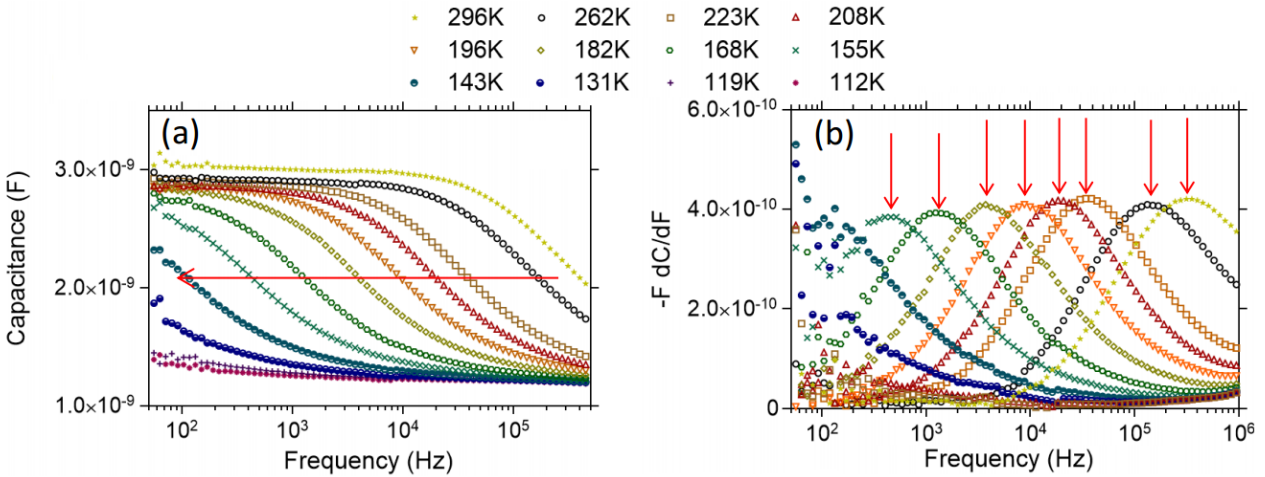
Fig. 2. 15.(a) CF data at different temperatures for P3HT-based polymer solar cells. Arrow shows reduction in temperature. (b) Corresponding $f \times dC/df$ as a function of frequency. Arrows show the peak in DOS. Peak frequency shifts with temperature[97].
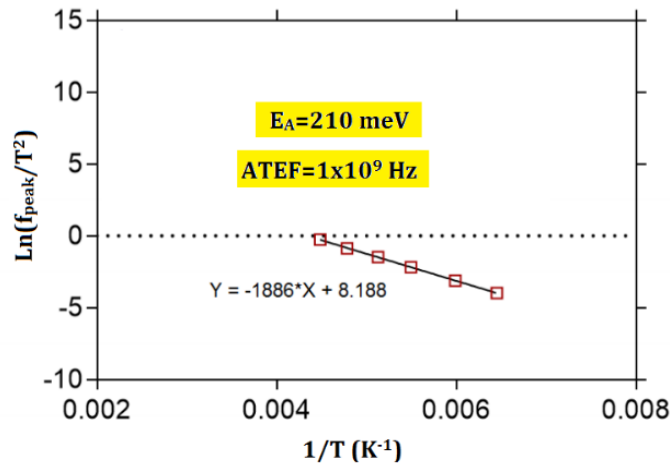
Fig. 2. 16. $Ln(f_{peak}/T^2)$ vs. $1/T$ for peak frequencies (f_{peak}) in Fig. 2.15(b). The slope yields an activation energy of 210 meV, and the intercept reveals that ATEF is $\sim 10^9 Hz$[97].

finds that the shift in f_{peak} is Arrhenius with an activation energy of 210 meV. This indicates the existence of a defect band located 0.2 eV above from the valance band. Moreover, the intercept of the line in Fig. 2.16 yields an ATEF of $\sim 10^9$ Hz for P3HT at room temperature[97].

CHAPTER III
ORGANIC BULK HETEROJUNCTION SOLAR CELLS

3.1.   Introduction: Why organic cells?

In an organic cell, the light-absorbing layer is a semiconducting polymer or small molecules. Fig. 3.1 shows the molecular structures of some of the most commonly-used polymers for making solar cells[98]. These organic compounds offer a very high absorption coefficient (typically in the range of 10^5 /cm)[99,100,101], which means that organic cells can be made very thin (~100 nm in thickness). Moreover, since they can be deposited at low-temperatures, flexible plastic substrate can be used in large-scale role-to-role manufacturing of organic cells[102]. These properties render organic cells as cost-effective alternative source of energy. Organic solar cells have, therefore, inspired excitement in the photovoltaic research community for the past two decades. The efficiencies of organic solar cells have, consequently, risen from about 1% in 1986[103] to ~11% in 2014[104].
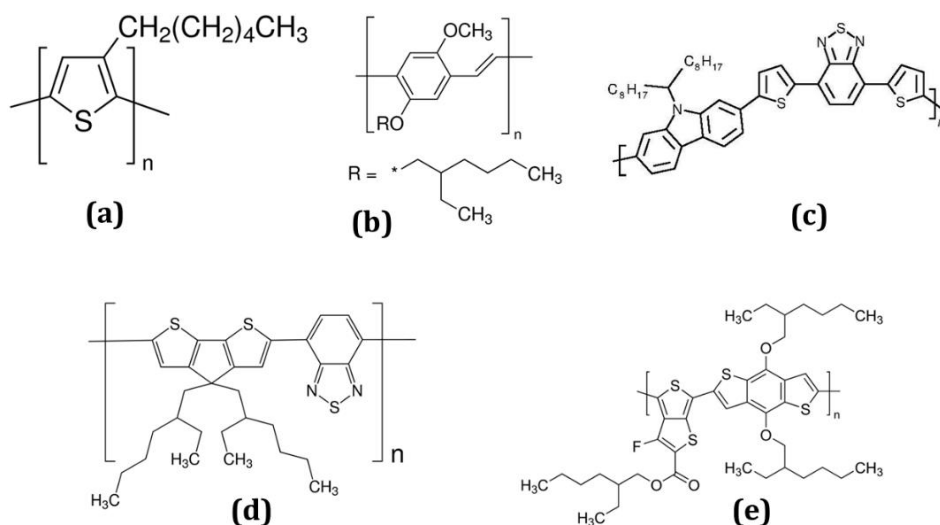
Fig. 3. 1. Molecular structure of some frequently-used light absorbing polymers: (a) P3HT, (b) MEH-PPV, (c) PCDTBT, (d) PCPDTBT, and (e) PTB7.

This chapter is intended to explain the fundamental concepts in device physics of organic Bulk Heterojunction (BHJ) cells such as device structure, band diagrams, recombination losses, field-assisted vs. diffusion currents in IV characteristics, and stability issues.

3.2.   Operating principle of organic solar cells

As we discussed in earlier chapters, when a photon is absorbed in a material, it creates an electron hole pair (EHP). The electron and hole are bound to each other through Coulomb force:

$$F = \frac{1}{4\pi\,\varepsilon_0 \varepsilon_r} \times \frac{q^2}{r^2} \tag{3.1}$$

Where q is unit charge, r is distance, ε_r and ε_0 are relative and vacuum permittivity, respectively. As we discussed earlier in chapter 1, the binding energy is, therefore, inversely proportional to the relative permittivity. For traditional inorganic semiconductors (e.g. Si), high ε_r (~11.9) leads to small binding energies (~15 meV). Thus, the excitons in inorganic semiconductors dissociate thermally at normal operating temperatures, and give rise to free charge carriers in the material.

For organic semiconductors, on the other hand, low ε_r leads to high binding energies in the range of 0.1 to 1 eV, which means that the excitons in organic semiconducting polymers do not thermally dissociate operating temperature. This imposes a sever limitation on application of polymers as light-absorbing layer in solar cells, unless the bound EHP are broken into free charge carriers. This could be achieved through using a heterojunction (shown in Fig. 3.2)[105]. Here, the polymer is brought into contact with another material to form a type II heterojunction. This second material is usually a
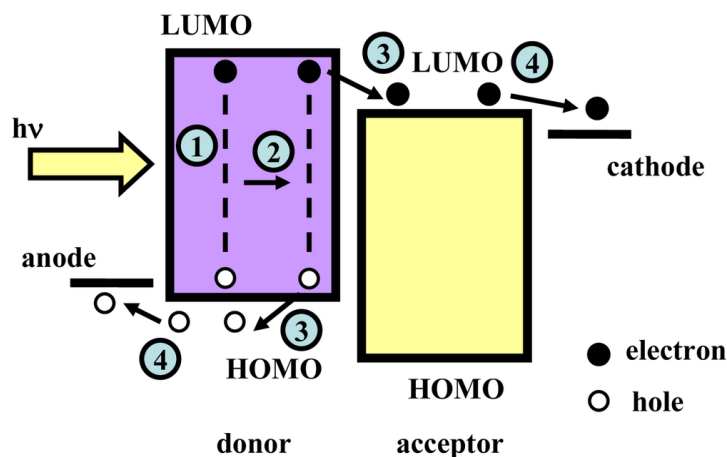
Fig. 3. 2. Basic processes in an organic solar cells: (1) Light absorption, (2) Diffusion of excitons to the interface, (3) Exciton dissociation at the interface, (4) Carrier transport and collection at the contacts.
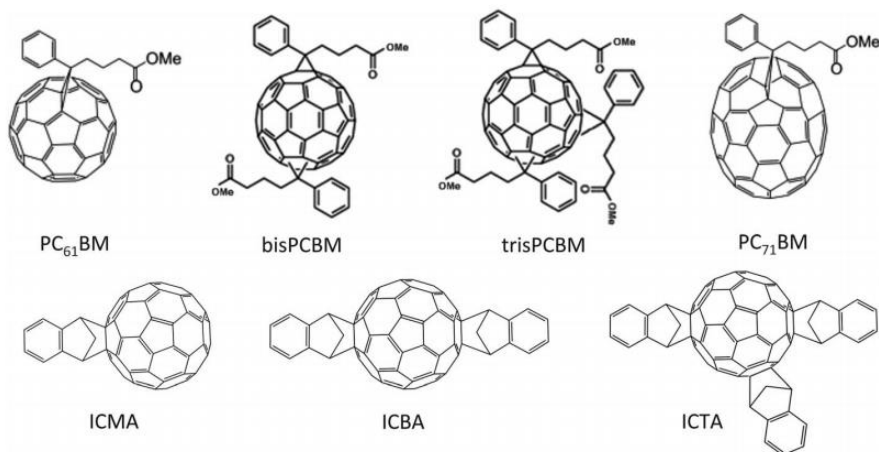
Fig. 3. 3. Molecular structure of some frequently-used acceptors in organic photovoltaics.

fullerene. The molecular structure of three of the most commonly used fullerenes are depicted in Fig. 3.3[106].

The fundamental operating principle of bilayer heterojunctions are depicted in Fig. 3.2: (1) Absorption of light gives rise to excitons in polymer. (2) Since excitons are electrically neutral entities, they can reach the junction only through diffusion, and (3) get dissociated at the interface due to the local electric field. During the dissociation process the electron is "transferred" from polymer to the fullerene. Hence, the polymer is
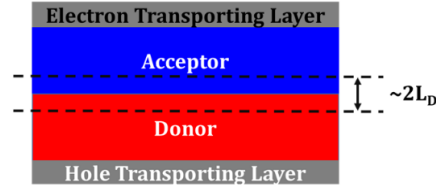
Fig. 3. 4. Structure of a bilayer device. Only the excitons which are generated within the diffusion length of the D/A interface (between the dashed lines) dissociate and give rise to free charge carrier.

frequently referred to as the "donor". The fullerene, on the other hand, receives the electron, and hence is called the "acceptor". (4) The free electrons and holes are transported and collected at the contacts through, respectively, the acceptor and the donor materials. The quantum efficiency can, therefore, be expressed as the product of the efficiencies of the four steps[107]:

$$\eta_{QE} = \eta_A \times \eta_{ED} \times \eta_{CT} \times \eta_{CC} \tag{3.2}$$

Where η_{QE} is the quantum efficiency, η_A is the efficiency of absorption process in the organic material, η_{ED} is the fraction of excitons that diffuse to the donor/acceptor (D/A) interface. η_{CT} is the efficiency of exciton dissociation process at D/A interface, and η_{CC} is the fraction of free charges that get collected at the contacts.

3.3.   Device structures: Bilayer vs. Bulk Heterojunction (BHJ)

The heterojunction described in the previous section can be realized simply by a bilayer structure. This is depicted in Fig. 3.4. In this bilayer device the amount of generated charge carriers strongly depends on the diffusion length of the excitons. Since exciton diffusion length is known to be roughly in the range of 5-20 nm[108, 109, 110], only those photons that get absorbed within this distance of the heterojunction can result in free charge carriers. All
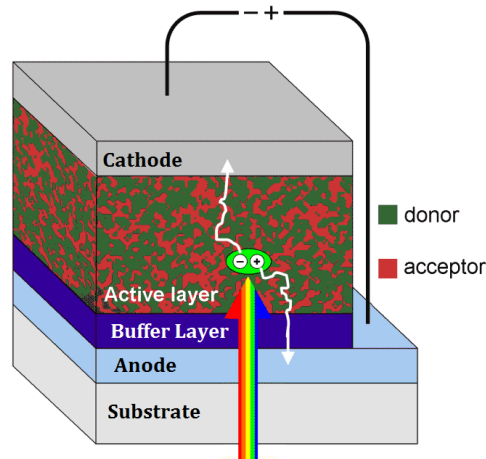
Fig. 3. 5. A bulk heterojunction solar cell. Donor and acceptor materials are mixed such that excitons can reach the interface easily. After dissociation, the electron is transported to cathode via the acceptor phase. Likewise, the hole travels to anode through the donor network.

other excitons that are generated farther from D/A interface are lost to recombination before reaching the interface. Bilayer devices therefore show very small PCEs (<0.1%).

In order to achieve higher efficiencies, the heterojunction is distributed across the bulk of the device by simply mixing the acceptor and the donor materials together[111]. The resulting morphology is depicted in Fig. 3.5[112], and is called a "Bulk Heterojunction" (BHJ). A bulk heterojunction, therefore, consists of two interpenetrating networks: interconnected donor-rich and acceptor-rich domains. After the excitons dissociate at the interface, the free holes and electrons are transported to the contacts, through donor and acceptor networks, respectively. A very critical parameter which determined device performance of the bulk heterojunctions is, therefore, the donor and acceptors domain sizes. If the domains are considerably larger than the exciton diffusion lengths, cell efficiency will drop due to annihilation of excitons before reaching the donor/acceptor (D/A) interface. If, on the other hand, the domain are very small, they will not form a
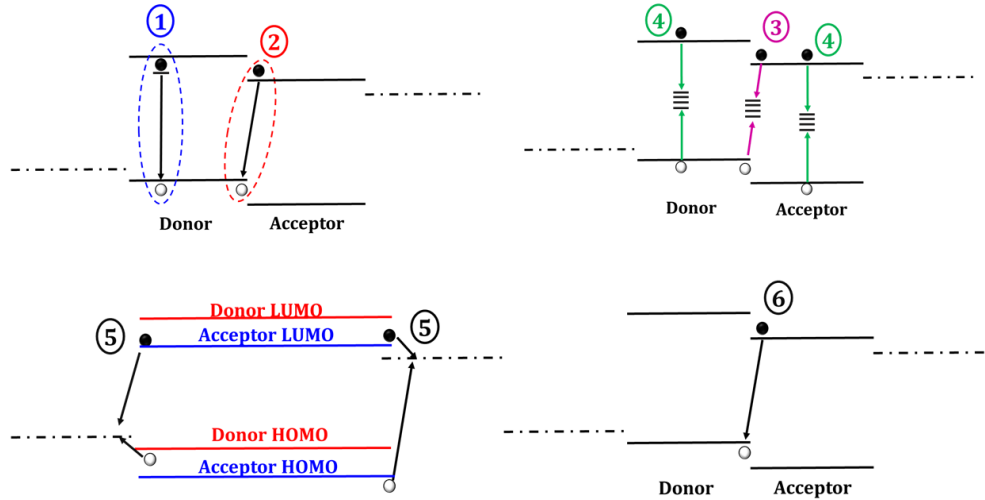
Fig. 3. 6. Recombination pathways in a BHJ: (1) Excitonic, (2) Geminate, (3) D/A interface trap-assisted, (4 Trap-assisted inside the domains, (5) contact, and (6) Band-to-band recombination.

continuous network which is much needed for transporting the free charge carriers to the contacts. The optimal domain size, is therefore considered to be roughly of the size of exciton diffusion length (10-20 nm).

3.4.   Recombination in organic solar cells

Fig. 3.6 shows different pathways of loss in a bulk heterojunction:

(1) Excitonic loss: Excitons that are generated far from the D/A acceptor interface will not reach the interface, and are lost to recombination.

(2) Geminate loss[113,114,115]: is defined as the recombination of a carrier pair which were generated by the same photon. After the exciton dissociation at the D/A interface, the two carriers are still separated by a small distance and are attracted to each through Coulomb force. It is possible that they recombine with each other through a direct band to band transition.

(3) Trap assisted recombination at the interface: While being transported to the contacts, the free charge carriers can still meet carriers from opposite type at the

D/A interface, and recombine with them through the interfacial defect states. Applying an external electric field sweeps away the carriers from the interface and enhances collection.

(4) Recombination in the domains: The free charge carriers can, in principle, recombine inside the domains as well. However, considering that the donor is p-type, and the acceptor is n-type, holes and electrons are majority carriers in, respectively, donor and acceptor domains. As a result, the carrier lifetimes are expected to be much longer in the bulk of the domains than at the D/A interface, where free charges can easily recombine with carriers of the opposite type. This is easily understood from Matthiessen's rule:

$$\frac{1}{\tau} = \frac{1}{\tau_{bulk}} + \frac{1}{\tau_{interface}} \cong \frac{1}{\tau_{interface}}$$

The overall carrier lifetime is hence not limited by in-domain recombination.

(5) Recombination at the contacts: since acceptor and donor networks are in contact with both electrodes, it is possible that electrons and holes get recombined at contacts. Using electron-blocking interlayers (e.g. NiO_x [116,117]) in the anode, and hole-blocking interlayers (e.g. TiO_x [118,119]) at the cathode will suppress this recombination pathway.

(6) Band-to-band recombination: Free charge carriers can recombine non-geminately at the interface through transitions between LUMO of acceptor and HOMO of donor.

The maximum performance that can be achieved with a donor-acceptor blend, and the dominating recombination loss mechanism(s) depend heavily on the individual polymer

and fullerene that are being used. In the next chapter, we focus on presenting our results on a specific high-performing BHJ (PTB7:PCBM$_{70}$ blend). Based on fundamental measurements discussed in chapter 2, we analytically calculate and predict the device characteristic. The outcome of our analytical modeling helps understanding recombination and device data.

CHAPTER IV
DEVICE PHYSICS OF PTB7:PCBM$_{70}$ BULK HETEROJUNCTION SOLAR CELLS

4.1. Introduction

PTB7 is an important polymer in the field of organic photovoltaics, and a lot is known about its morphological characteristics, both in pristine state and when blended with PCBM$_{70}$. Very little is, however, reported on the fundamental electronic properties of the blend. Electronic properties, such as defect densities and Urbach tails, are important for understanding device physics, and are key in identifying sources of loss in any solar cell; we therefore dedicate part of this chapter to exploring these properties using the measurement techniques described in chapter 2.

We then move forward and use our findings to develop a model for explaining device-level characteristics of PTB7:PCBM$_{70}$ solar cells. Knowing the electronic properties of the blend, we first compute trap-assisted recombination rates using an analytical approach. A closed-form expression for recombination rate is then used to explain fundamental device characteristics such as photo-voltage, dark IV and V$_{OC}$ vs. light intensity. The model is, moreover, applied to understand V$_{OC}$-limiting factors, as well as the photo-degradation mechanism.

4.2. Material properties of PTB7 and PTB7:PCBM$_{70}$ blend

PTB7 is developed by Luping Yu at the University of Chicago in 2010[120]. Blended with PCBM$_{70}$, it has produced efficiencies as high as 9% [121]. The molecular structure and
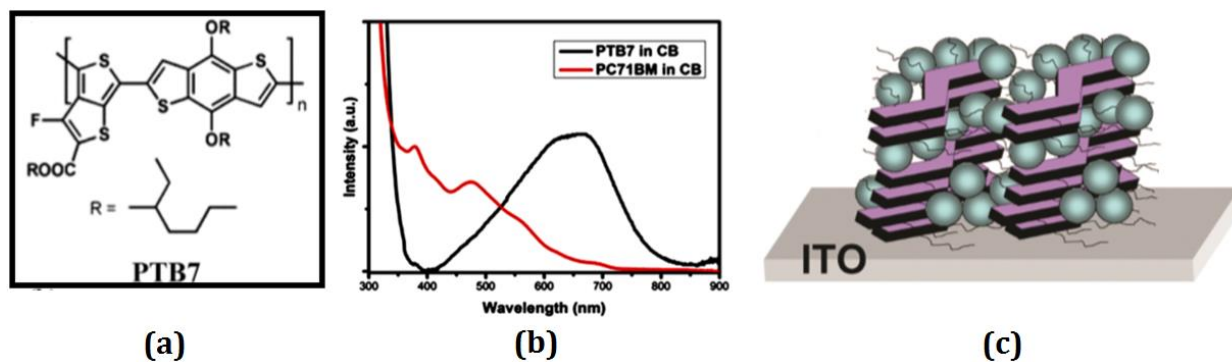
Fig.4.1. Molecular structure of PTB7[122] (a), absorption spectra of PTB7 (black) and PCBM70 (red)[122](b), schematic of the blend (c) which depicts orientation of polymer backbones (purple) with respect to the substrate. The blue balls are PCBM70 molecules [123].
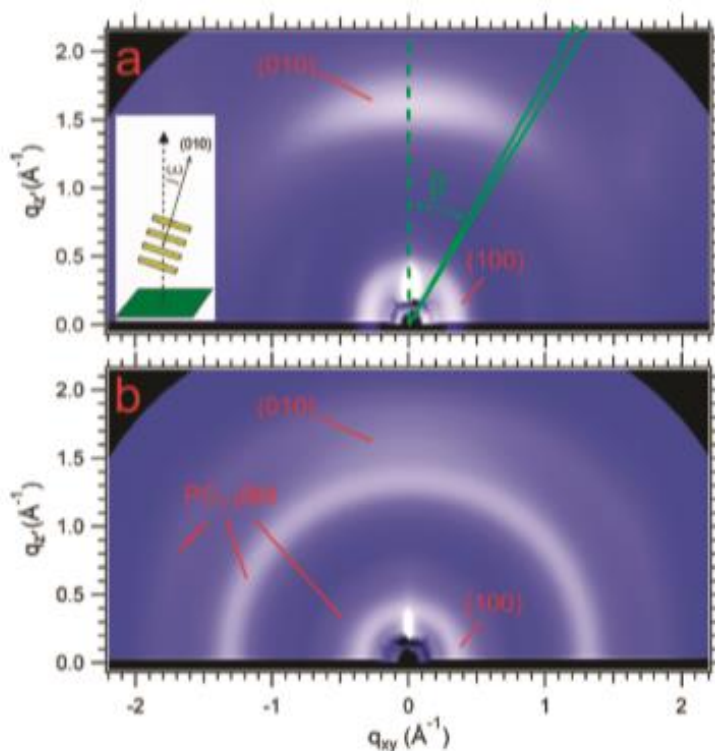
Fig. 4.2. GIXRD pattern of a PTB7 (a) and PTB7:PCBM70 blend (b) thin films [124].

absorption spectra of PTB7 is presented in Fig. 4.1. The HOMO and LUMO level of this material are measured to be 5.15 and 3.31 eV, respectively [120]. This makes a bandgap of ~1.8 eV causing the absorption to drop beyond~ 700 nm (Fig. 4.1(b)).

Research has shown[122] that when the PTB7:acceptor blend is spin coated, the polymer backbone orientation is such that the π-π stacking direction is out of plane (Fig. 4.1 (c)).

This makes the material attractive for photovoltaic applications, since the direction perpendicular to the substrate is favorable for charge transport in a solar cell. Carrier mobility, however, remains as low as $\sim 5 \times 10^{-4}$ cm^2/V.sec [120], primarily due to the fact that PTB7 is a mostly amorphous polymer. X-ray diffraction studies [124] have shown that only about 20% of a spin-coated PTB7 film is crystalline, and the rest is indeed amorphous. Fig. 4.2 (a) and (b) shows grazing incidence X-ray diffraction (GIXRD) pattern of a PTB7 and a PTB7:PCBM$_{70}$ film, respectively[124]. The 010 peak (π-π stacking peak) of PTB7 is very broad and distributed in azimuthal direction, indicating the absence of long-range order in the material. The case is worse in the PTB7:PCBM$_{70}$ blend film, where the 010 peak is barely visible (Fig. 4-2(b)). Morphological studies by H. Ade et. al.[125] have shown that the blend film consists of two phases: pure PCBM$_{70}$ domain and polymer-rich domains, where polymer-rich domains consist of $\sim$ 70 wt% polymer and $\sim$30 wt% PCBM$_{70}$.

The PTB7:PCBM$_{70}$ blend is deposited by spin-coating. For highest reported efficiencies the host solvent is either 1,2-dichlorobenzene or chlorobenzene. A small amount ($\sim$3 vol%) of 1,8-diiodooctane (DIO) is used as solvent additive in the solution. Studies on the liquid-state have revealed that the presence of DIO in the solution decreases PCBM$_{70}$ agglomerate size[126] which, in turn, leads to smaller acceptor domain size after spin coating [125, 126]. Smaller domain size yield a finer morphology with higher polymer-acceptor interface area which is known to be necessary for achieving high currents in bulk-heterojunction solar cells. It is also shown that the presence of DIO in the solution does not alter domain composition of the polymer-rich phase and does not affect the crystallinity of

the film[125]. Recent transient measurements suggest that best cells made with DIO have negligible geminate loss [127]. So, we safely neglect the geminate loss in our device analysis and will focus on only on non-geminate loss calculations.

4.3.   Fabrication Process

Fabrication process and device structure of a standard PTB7:PCBM$_{70}$ bulk heterojunction solar cell are shown in Fig. 4.3 (a) and (b), respectively. First, a thin layer of a hole transporting layer material (PEDOT:PSS) is spin-coated on cleaned ITO-covered glass substrate at 4000 rpm for 40 sec. Then the substrate is annealed at 150 C for 20 minutes in air. The samples were afterwards transferred into a Nitrogen glovebox where ~100nm of PTB7:PCBM$_{70}$ (1:1.5) blend is spin-coated from solution state. The solution consists of 10 mg/ml of PTB7 and 15 mg/ml of PCBM70 in 1,2-dichlorobenzene with 3 vol.% 1,8-diiodooctane as processing additive.

After spin-coating the blend, the device is thermally annealed on a hotplate. Annealing time and temperature could vary depending on the experiment. Then calcium

(a)   (b)
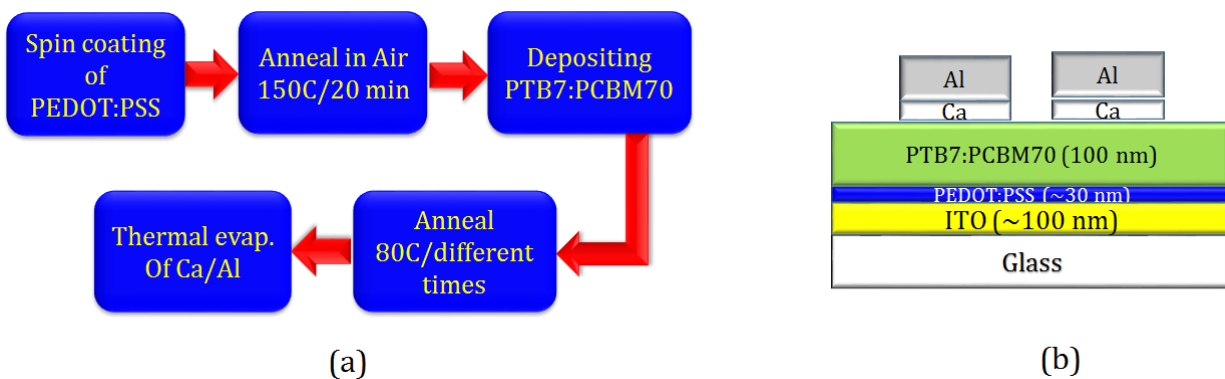
Fig. 4.3. Fabrication process (a), and device structure (b) of a standard p-i-n PTB7:PCBM$_{70}$ cell.

Fig. 4.5. Density of defects in PTB7:PCBM$_{70}$ cells obtained by CF measurements.
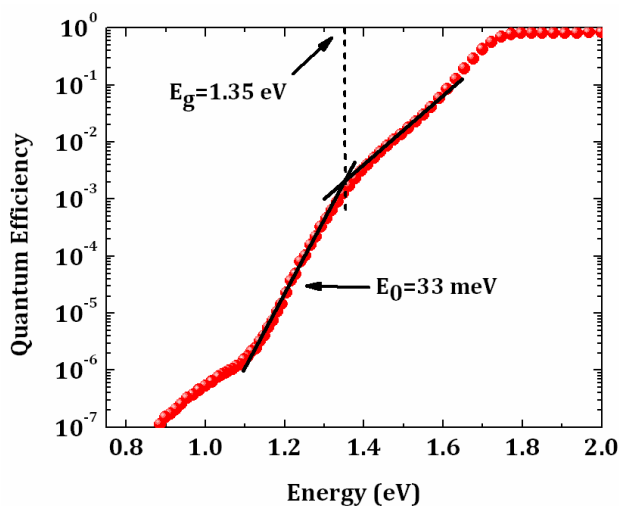
*Fig. 4. 6. Subgap QE of a PTB7:PCBM$_{70}$ cell. The D/A interfacial bandgap is ~1.35 eV,
and Urbach energy of tail states is 33 meV.*

4.5. Effect of low temperature thermal treatment

Thermal annealing is known to improve the performance of BHJs by enhancing the material's transport characteristics through crystallization. Moreover, it induces D/A phase separation which leads to the growth of polymer and fullerene domains. When the domains are large enough, they form two interpenetrating networks of polymer and fullerene, which transport holes and electrons to anode and cathode, respectively [128,129]. It should be noted, however, that high-temperature or prolonged annealing leads to excessive D/A phase

separation. In such cases, the overall performance of the device drops because of excitonic loss in large domains.

It is shown previously that thermally-induced D/A phase separation at elevated temperatures decays the performance of BHJs made from PTB polymers [123]. However, there were no conclusive study on the effect of thermal treatment on PTB7-based cells. So, we decided to explore this area, and find out whether there are any combination of annealing temperature/time that can improve device characteristics. We started at very low temperatures, and annealed the samples at 80 C for various times before depositing Ca/Al cathodes. Fig. 4.7 shows the resulting IV characteristics, which demonstrates no significant change in performance. The curves are almost exactly the same, and there is no significant gain or loss in the power conversion efficiency. The only curious change is a small increase in V$_{OC}$ by ~30 mV upon thermal treatment.
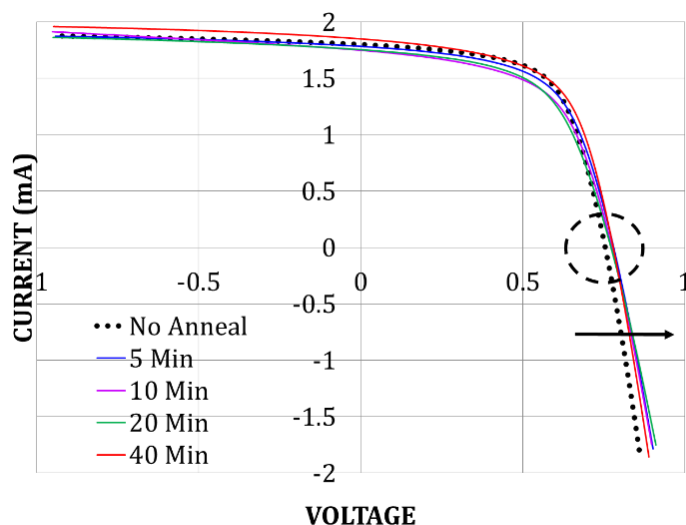
Fig. 4.7. Current-Voltage characteristics of PTB7:PCBM70 cells thermally treated at 80C for various times. The IV curves are identical. The only notable change is a tiny increase in V$_{OC}$ (All thermally treated devices have upto ~30 mV higher photo-voltage compared to un-annealed cells.).
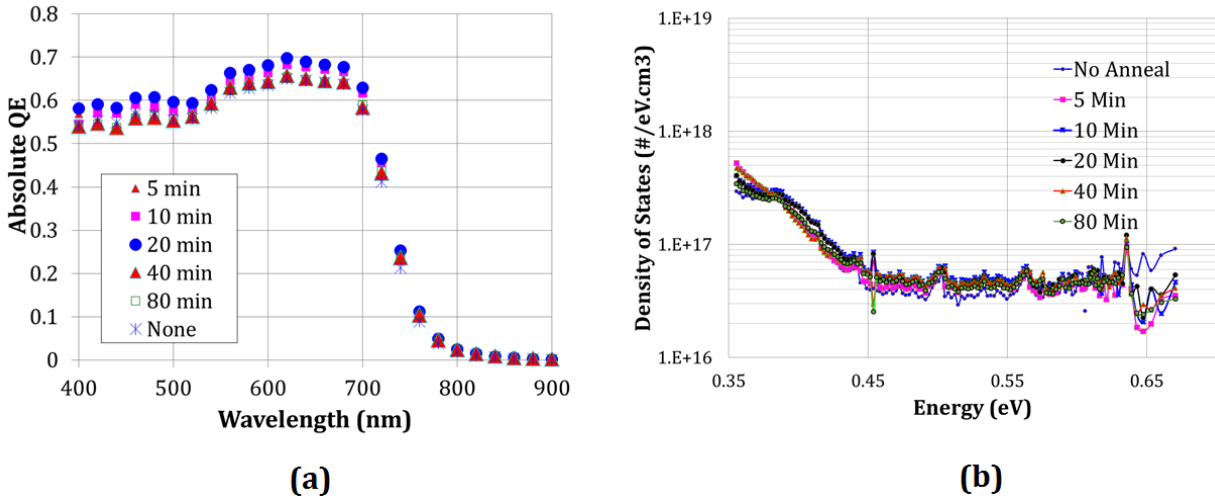
Fig. 4.8. QE (a) and DOS (b) of PTB7:PCBM70 cells annealed at 80 C for 0, 5, 10, 20, 40 and 80 minutes.

Figs 4.8 (a) and (b) show the QE and DOS of the cells, respectively. There is no appreciable difference between the characteristics of the cells, implying that the treatment does not induce any significant morphological changes in the blend (at least in terms of phase separation, defect states, bandgap and transport characteristics).

Fig. 4.9(a) shows the dark IV characteristics of the cells. There is a huge decrease (2 to 3 orders of magnitude) in shunt current when the device is treated. This reduction in shunt current is related to the observed increase in V_{OC} through the equivalent circuit of the device (Fig. 2.1).

We conclude that thermal treatment at low temperatures does not appreciably influence the morphology of the main layer. It, however, significantly reduces shunt current which obscures dark IV by burying the ideality factors and saturation currents. These are critical parameters that contain valuable information about recombination in the device, and ought to be extracted and analyzed very carefully. Proper heat treatment is, therefore, a critical step in device fabrication and minimizes the parasitic shunt, most likely by
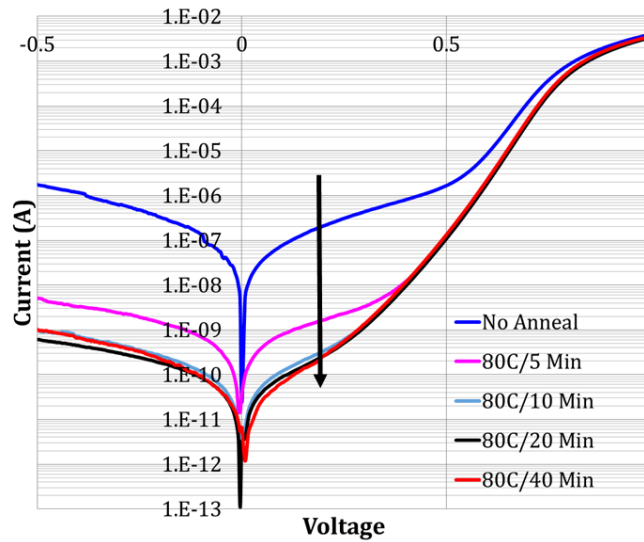
Fig. 4.9. Dark IV characteristics of devices annealed at 80C for different times.

removing the residual solvent from the film and improving the PEDOT:PSS/blend interface.

We must add that annealing devices at elevated temperatures (>100 C), lead to decrease in short circuit current and loss of fill factor: a signature of D/A phase separation at high temperatures. The loss of performance at these temperatures forced us to limit the thermal treatment of devices to ~80 C, so as to reduce the dark shunt current without inducing undesired morphological changes to the blend.

4.6. Calculating recombination in PTB7:PCBM$_{70}$ BHJs

In many occasions, bulk heterojunction solar cells are modelled numerically by solving coupled transport equations, and fitting the calculated light or dark IV characteristics to measurement results (See ref. 58 for example). While this approach is precise in predicting device behavior, and provides great insight to device physics, the calculations involved are often cumbersome, and are handled by computer simulators. Analytical modeling, on the other hand, avoid these complication by making simplifying assumptions which pave the road to convenient closed-form expressions for approximating

device characteristics. This convenience is, of course, obtained at the expense of loss of precision, but it provides great insight to device physics and reasonable approximation for its behavior, yet avoiding complications arising from numerical methods.

In this work, we, therefore, choose an analytical approach to obtain a closed-form expression for approximating the recombination rate in PTB7 cells. The significance of the model is that it relies on basic parameters that are extracted from our fundamental electrical and optical studies reported earlier in this chapter. Moreover, as long as certain assumptions hold, the method can be applied to any BHJ. These assumptions are discussed later in the chapter.

Fig. 4.10 depicts the band structure of a disordered material. The energy difference between the edges of conduction (E_C) and valence (E_v) bands is the bandgap (E_g). In our case, E_C is the LUMO of acceptor, E_v is the HOMO of the polymer, and E_g corresponds to the D/A interfacial bandgap. From the subgap QE, we are already aware that $E_g \sim 1.35$ eV for PTB7:PCBM$_{70}$ blend. Below E_C and above E_v, there are exponential distributions of electronic tail states which obey the following equation:

$$N(E) = N_1 \cdot \exp\left(-\frac{|E - E_{edge}|}{E_0}\right) \tag{4.1}$$

Where E_{edge} is the edge of conduction/valence band; E_0 (Urbach energy) is ~33 meV from the subgap QE measurements; and N_1 is the concentration of electronic states at the band edges and is expected to be roughly 10^{20} cm^{-3} [130]. Our CF measurements in previous section showed that the deep defect states ($g(E)$) have an almost flat distribution with a
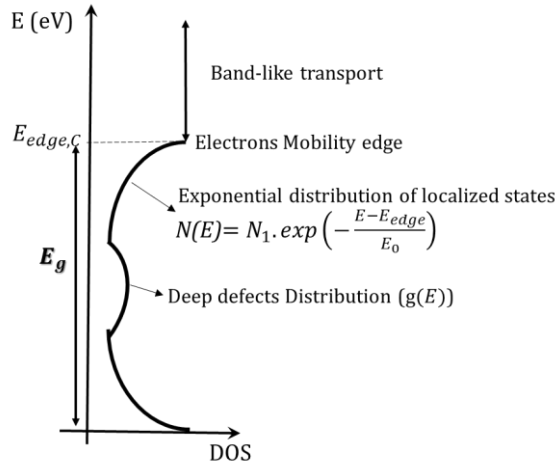
Fig. 4.10. Mobility Edge (ME) model of a disordered semiconductor.
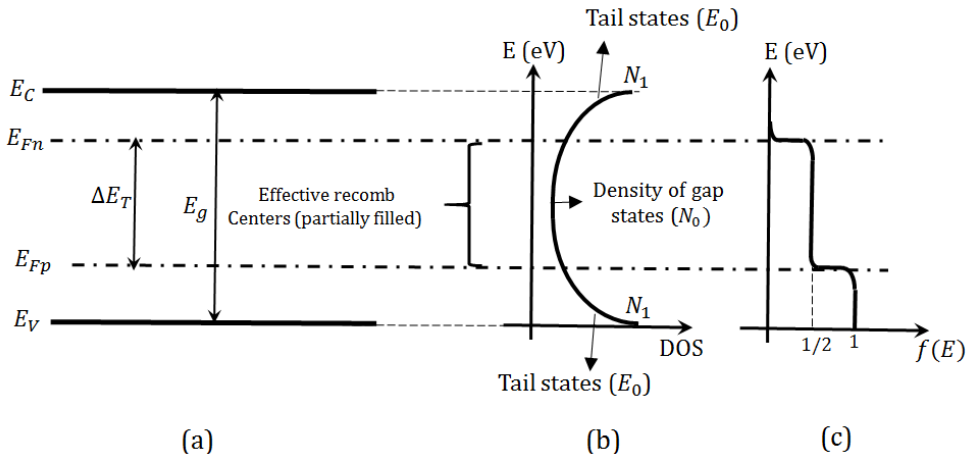
Fig. 4.11. Band diagram (a), DOS (b), and modulated Fermi function (c) in a disordered semiconductor under illumination.

density of $g(E)=N_0 \sim 10^{16}$ cm^{-3}.eV^{-1}. In this picture, we assume that transport follows the Mobility Edge (M. E.) model, i.e. above E_c, and below E_v the carrier transport is band-like, while in the tails electrons and holes move by hopping between delocalized states[130, 131].

The population of free charge carriers and occupation probability of electronic states are determined by the relative position of quasi-Fermi levels with respect to the band edges (Fig. 4.11 (a)).

The density of gap states (Fig. 4.11(b)) obeys the following equation:

$$N(E) = N_0 + \frac{N_1}{E_0} \cdot \left(\exp\left(-\frac{E_c - E}{E_0}\right) + \exp\left(-\frac{E - E_V}{E_0}\right) \right) \tag{4.2}$$

Simmons and Taylor have shown[132] that in an i-layer with a symmetric DOS, all states that lay above the electron quasi-Fermi level (E_{fn}) are, to the first approximation, empty. On the other hand, states that fall below hole quasi Fermi level (E_{fp}) can be considered occupied. The probability of traps being occupied between E_{fn} and E_{fp} is roughly 0.5 when n~p. This is shown in Fig. 4.11(c). Here, *f(E)* is called the modulated Fermi function, and gives trap occupation under non-equilibrium conditions. A direct result of their work is that for an i-layer with symmetric separation of quasi-fermi levels, the effective recombination centers are limited to those half-filled states which are sandwiched between E_{fn} and E_{fp}. So, the total number of effective recombination centers is obtained by integrating the DOS (eq. (4.2)) between the two quasi-Fermi levels:

$$N_T = \int_{E_{Fp}}^{E_{Fn}} N(E).dE \approx N_0 \, \Delta E_T + 2.N_1 \cdot \exp\left(\frac{\Delta E_T - E_g}{E_0}\right) \tag{4.3}$$

where ΔE_T is the separation between the quasi Fermi levels ($E_{Fn} - E_{Fp}$).

The trap-assisted recombination rate is directly proportional to the population of the free charge carriers, and the number of available recombination centers.

$$R = f \times \gamma \times N_T \times n_f = \gamma.N_1.\left(0.5 \times N_0 \, \Delta E_T.\exp\left(\frac{\Delta E_T - E_g}{2kT}\right) + N_1.\exp\left(\frac{\Delta E_T - E_g}{nkT}\right) \right) \tag{4.4}$$

Where n_f is the concentration of free charge carriers, and is estimated by Boltzman approximation [133]:

$$n_f = N_1 \cdot \exp\left(-\frac{E_c - E}{kT}\right) \tag{4.5}$$

"n" is the ideality factor and is defined as:

$$n \equiv \frac{2}{1 + kT/E_0} \tag{4.6}$$

In equation (4.4), $f \sim 0.5$ is the trap occupancy, and γ is the proportionality coefficient. In numerical calculations of trap-assisted recombination, the process is considered as a two body reaction between free carriers on one hand and, on the other hand, trapped charge carriers of the opposite type. So, this parameter is typically approximated with Langevin coefficient [58]:

$$\gamma = \frac{q}{\varepsilon} \mu_n \tag{4.7}$$

Where μ_n is the free charge carrier mobility, and is of the order of 10^{-4} cm².V⁻¹.sec⁻¹ for PTB7:PCBM₇₀.

Now, we define:

$$f_1(N_0, E_g, \Delta E_T) = 0.5 \times N_0 . \Delta E_T . \exp\left(\frac{\Delta E_T - E_g}{2kT}\right) \tag{4.8}$$

$$f_2(E_0, E_g, \Delta E_T) = N_1 . \exp\left(\frac{\Delta E_T - E_g}{nkT}\right) \tag{4.9}$$

Hence:

$$R = \gamma . N_1 \left(f_1(N_0, E_g, \Delta E_T) + f_2(E_0, E_g, \Delta E_T) \right) \tag{4.10}$$

Eq. 4.10 is central to our interpretation of device data; it expresses the recombination rate as a competition between recombination at deep defects (represented by $f_1(N_0)$) and recombination at tail states (represented by $f_2(E_0)$).

4.7. Inferences from the multiple-level trap model

So far, we have measured the fundamental properties of the PTB7:PCBM₇₀ BHJ solar cells. Moreover, we developed an analytical expression for estimating recombination rate in the device. In this section, we examine the recombination rate equation in more detail,

and draw inferences for different illumination levels. The inferences will later be used to test the model against experimentation, and verify its validity for the blend under study.

4.7.1. Photo-voltage

A very important condition for studying device physics is when the device is under illumination in "open-circuit". The carriers are not extracted from the cell, and are instead forced to recombine with each other. Under open-circuit conditions, the recombination rate is equal to the generation rate, and the corresponding separation between quasi-Fermi levels gives rise to V_{OC}. Eq. 4.10, therefore, provides an opportunity to make theoretical estimates of the V_{OC} values. So, the first test is to calculate V_{OC}, and compare it with experimentally obtained values.

4.7.2. Photo-voltage as a function of light intensity

Now, we examine Eq. 4.10 more closely under open circuit conditions in the presence of light (when $\Delta E_T \gg kT$). Under such circumstances, we find by calculations that ($f_2 \gg f_1$) and therefore:

$$R \cong \gamma . N_1 . f_2\left(E_0, E_g, \Delta E_T \right) \tag{4.11}$$

Which states that recombination is dominated by the tail states and not deep defects. Assuming that the generation rate is directly proportional to light intensity ($G \propto I$), eq. (4.11) can be written as:

$$V_{OC} = c + n.\frac{kT}{q}.Ln(I) \tag{4.12}$$

Where c is a constant and n is the idealit factor, and is determined by Eq. 4.6. By using different methods, other groups have recently obtained similar expressions for V_OC and ideality factor[134, 135, 136].

4.7.3 Dark saturation current

For small values of ΔE_T (e.g. a few kTs), one finds that $f_1 >> f_2$, and therefore Eq. 4.10 reduces to:

$$R \cong \gamma . N_1 . f_1 \left(N_0, E_g, \Delta E_T \right) \tag{4.13}$$

Which states that under dark conditions recombination is dominated by the deep defects at small biases. Since the dark IV saturation current (I_0) is the recombination current extrapolated to zero, one can right:

$$I_0 = q.A. \int R.\,dx \propto \gamma . N_1 . N_0 . A.\ \Delta E_T . \exp \left(\frac{-E_g}{2\,kT} \right) \tag{4.14}$$

Where A is the device area.

Notice that the dark saturation current is directly proportional with the density of deep defects. Moreover:

$$I_0 \propto \exp \left(\frac{-E_g}{2\,kT} \right) \tag{4.15}$$

Hence, if recombination is dominated by deep defects, I_0 vs. $(kT)^{-1}$ is an Arrhenius diagram with an activation energy equal to half of the D/A bandgap, which is examined by measuring Dark IV vs. temperature.

In summary, deep defects are major recombination centers under near thermal equilibrium conditions. The separation of quasi-Fermi levels increases with illumination or applied bias, until they hit the Urbach tails, where they get pinned due to the exponential

nature of the tails. At this point, recombination is mostly through tail states, and the pinning will set an upper limit on the photo-voltage. This conclusion is well in agreement with the results reported by Blakesly et. al.[135] that energetic disorder leads to loss of photo-voltage.

4.8. Experimental results and discussion

In this chapter, we have so far derived an expression for approximating the recombination rate and, drew a set of inferences that can be tested against experiment. These experiments are:

- Calculating photo-voltage (V_{OC}), and comparing it with the experimental value.

- Photo-voltage vs. intensity

- Dark IV vs. temperature

- Coupled dark IV and CF measurements

4.8.1. Theoretical calculations of photo-voltage

The block diagram in Fig. 4.12 shows how photo-voltage is developed across the device upon exposure to light. The light-generated excess carriers cause the quasi-Fermi levels split. As a result, the population of effective recombination centers increases. This in-turn reduces carrier life-time and increases the rate of recombination (R). The splitting of quasi-Fermi levels and increase in R continue until under steady-state the rate of recombination (R) matches generation rate (G). At this point, the steady-state photo-

Fig. 4.12. Shining light on the cell will cause a photo-voltage to develop across the sample.

voltage is equal to the difference between electrons and holes quasi-Fermi levels $(\Delta E_T \sim V_{oc})$.

Knowing the photo-current, we can estimate the generation rate in the cell to be:

$$G = \frac{J_{ph}}{q.t} \sim 10^{22} \quad cm^{-3} . sec^{-1} \tag{4.16}$$

Where t is the device thickness and for our cells is ~100 nm from AFM and profilometry measurements. Also, under steady-state G=R. Hence, we can write:

$$G = R = f(E_g, E_0, N_0, V_{oc}) \tag{4.17}$$

Where f is given by Eq. 4.10, $E_g \sim 1.35$ eV, $E_0 \sim 33$ meV and $N_0 \sim 10^{16}$ cm^{-3}.eV^{-1}. Solving this nonlinear equation, one finds $V_{OC} \sim 0.78$-0.79 V. This is in good agreement with the observed V_{OC} values for thermally-treated PTB7:PCBM$_{70}$ (i.e. ~0.77 to 0.79 V).

An important conclusion of this calculation is that the loss due to trap-assisted recombination at D/A interface is big enough to count for all the loss in photo-voltage and explains why the actual V_{OC} ~0.8 V is so much smaller than the maximum theoretical value $(E_g \sim 1.4$ eV).

4.8.2. V_{oc} vs. Intensity

Fig. 4.13 shows the open circuit voltage measured at different light intensities. Fitting Eq. 4.12 to the experimental data points (solid line) yields an ideality factor ~1.1 to 1.2. This is in very close agreement with the theoretical value obtained from Eq. 4.6 (n~1.12 assuming $E_0 \sim 33$ meV). This observation states that trap-assisted recombination
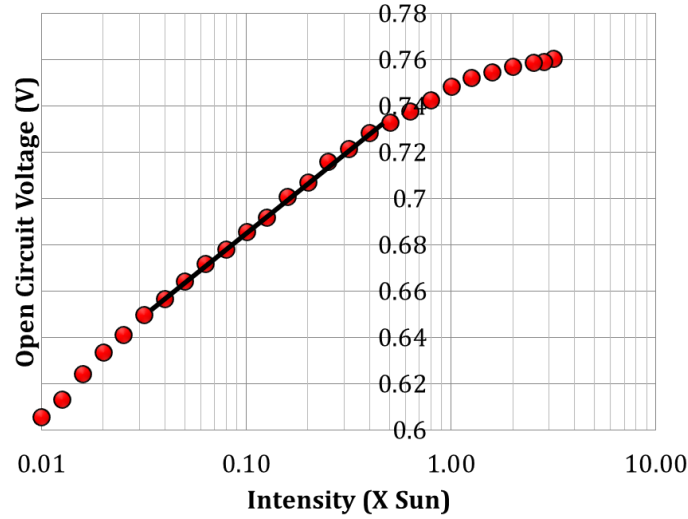
Fig. 4.13. V_{OC} vs. light intensity of a standard PTB7:PCBM$_{70}$ cell. The light ideality factor is extracted from the linear region and is about ~1.1-1.2.

can lead to light ideality factor of ~1, if the recombination is dominated by exponential tail states (vs. n~2 which is typically obtained for recombination in deep defects).

One has to be careful in interpreting this data, since band-to-band recombination could also result in a light ideality factor of ~1. However, if we calculate the recombination rate assuming that band-to-band recombination is the dominant source of loss, the calculated photo-voltage for a PTB7:PCBM$_{70}$ cell will be ~0.97 eV which is a big overestimation.

Saki et. al. [134] have also derived an analytical equation similar to Eq. 4.6., which leads to the same conclusions about V$_{OC}$ vs. light intensity curve. They have, however, stated that at very high intensities where the traps near the band edges are partially filled, the slope of the V$_{OC}$ vs. Intensity increases, yielding a light ideality factor of ~2. This is evidently not true at least in the case of PTB7:PCBM$_{70}$; At high intensities (> 2X Sun) there is a decrease in the slope of Fig. 4.13., which can be due to band-to-band and Auger recombination that become dominant at high carrier densities.

At very low intensity (<0.04 X Sun), the deviation from n~1 could be due to the taking over of recombination by deeper defects which leads to an increase in the slope of the curve.

This experiment suggests that tail state recombination (i.e. recombination of free carriers with trapped charged in the tails) is a major source of loss under illumination. Due to the exponential nature of tail states (Eq. 4.2), the major limiting factor for V_{OC} is the pinning the quasi-Fermi levels by the tails. This is a major conclusion of this study.

4.8.3. Dark IV analysis

When the effect of series resistance is negligible, the dark current of the cell is derived from Eq. 2.4 as:

$$I = \frac{V}{R_{sh}} + I_{01}\left(\exp^{\frac{qV}{n_1 kT}} - 1\right) + I_{02}\left(\exp^{\frac{qV}{n_2 kT}} - 1\right)$$ (4.18)

R_{sh} is the shunt resistance, and $I_{sh} = V/R_{sh}$ is the shunt current. I_{01} and I_{02} are the saturation currents, and measure the recombination rates. n_1 and n_2, on the other hand, are ideality factors and depend in the recombination mechanisms as discussed in chapter 2.

Fig. 4.14 (a) shows the room temperature dark IV of a PTB7:PCBM$_{70}$ BHJ before and after subtracting the shunt current. The device was annealed at 80 C during fabrication to keep I_{sh} at a minimum. We observe that the dark IV is very close to the classical picture; i.e. after subtracting I_{sh} from the data, the double diode behavior of Eq. 4.18 fits the data for over 7 orders of magnitude (Fig. 4.14(b)). The best fit is obtained for $n_1=2$ and $n_2=1.2$, which are signatures for deep and tail state recombination, respectively, as predicted by Eqs. 4.8 and 4.9. In Fig. 4.15, we plotted the recombination rates from these equations.
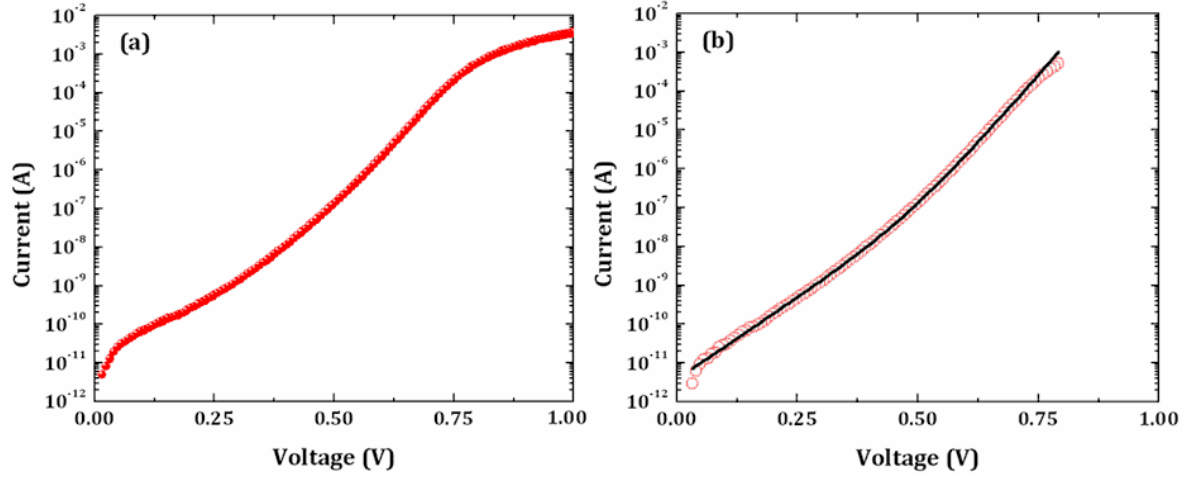
Fig. 4. 14 (a) Dark IV of PTB7:PCBM$_{70}$. By fitting Eq. 4.18 to the experimental data the shunt resistance is found to be 5×10^9 Ω. (b) Dark IV data after subtracting the shunt current. The best fit from Eq. 4.18 (solid line) is obtained for n$_1$=2, I$_{01}$=3.8×10^{-12}A, n$_2$=1.2, and I$_{02}$=5.6×10^{-15}A. These values are in agreement with those directly computed from recombination rate as estimated by Eq. 4.10.
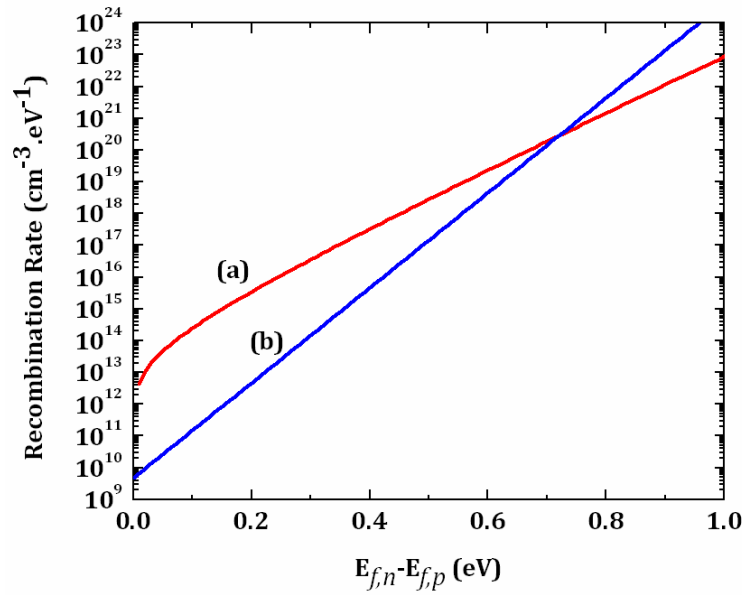
Fig. 4. 15. Recombination rate due to (a) deep defects, and (b) tail states as estimated by Eq. 4.10.

At zero bias, the calculated rate of recombination (R) is in 10^{13} s in deep defects, and 10^{10} s cm^{-3}.eV^{-1}.sec^{-1} at tail states.

Knowing that the dark saturation current is:

$$I_0 = Aq \int_{x=0}^{t} R \, . \, dx \approx q. R. t. A \tag{4.19}$$

with t ~ 100 nm and A~ 0.1 cm^2 is the area, one arrives at:

$I_{01} \sim (10^{-19} \text{ c}) \times (\sim 5 \times 10^{13} \text{ cm}^{-3}.\text{sec}^{-1}) \times (10^{-5} \text{ cm}) \times (10^{-1} \text{ cm}^2) \sim 5 \times 10^{-12} \text{ A}$ (4.20)

$I_{02} \sim (10^{-19} \text{ c}) \times (\sim 5 \times 10^{10} \text{ cm}^{-3}.\text{sec}^{-1}) \times (10^{-5} \text{ cm}) \times (10^{-1} \text{ cm}^2) \sim 5 \times 10^{-15} \text{ A}$ (4.21)

These values are in good agreement with those obtained from experimental data in Fig. 4.14(b): $I_{01}=4 \times 10^{-12}$ A and $I_{02}=6 \times 10^{-15}$ A. Our dark IV data, therefore, indicates that in a PTB7:PCBM$_{70}$ BHJ deep defects play a major role in recombination at low biases. At high forward currents, on the other hand, recombination at tail states dominate.

4.8.4. Dark IV vs. temperature

In the next experiment, we varied the temperature from 30C to 120C with steps of 10C, and measured the dark IV at each temperature. The dark IV curves are shown in Fig. 4.16 [54].
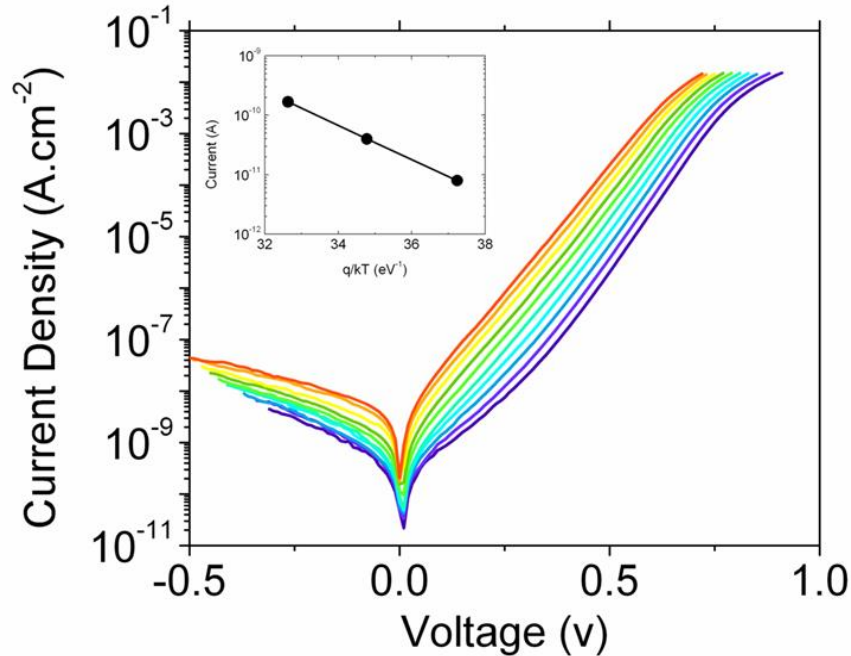
Fig. 4.16. Dark IV of a PTB7:PCBM$_{70}$ cell at different temperatures. The lowest curve (black) and the highest curve (red) are taken at 30 and 120 C, respectively. Each curve is 10C apart from in neighbors. Inset shows the Arrhenius diagram of I$_{01}$ with activation energy ~0.7 eV.

The dark current increases with temperature. The saturation current (I_{01}) shows a logarithmic dependence on $(kT)^{-1}$ (Fig. 4.16 inset). The activation energy of this Arrhenius

diagram is ~0.6-0.7 eV. This value is almost equal to half of the PTB7:PCBM$_{70}$ bandgap (E$_g$~1.35 eV), which is strongly suggestive of deep defect recombination. We should note that if we compute the recombination rate for a case when band-to-band recombination dominates, the theoretical activation energy of the Arrhenius diagram would emerge equal to the bandgap (~1.4 eV). It is therefore apparent that the results of our dark IV vs. temperature experiment rules out the significance of band-to-band loss in the cell.

4.8.5. Effect of irradiation

Photo-degradation is a major degradation pathway for organic BHJs. Many recent work have reported degradation of BHJs upon light exposure in inert atmosphere[137, 141]. In earlier works, we demonstrated that exposure to light in the absence of oxygen and moisture creates deep gap defects in P3HT:PCBM BHJs which leads to an increase in the dark saturation current, and loss of V$_{OC}$[137, 138]. This increase in dark recombination current is also observed by Kumar et. al. for P3HT:PCBM cells[139]. Moreover, Street et. al. have reported a similar phenomena by measuring subgap absorption for PCDTBT:PCBM BHJs when exposed to X-rays[140]. Peters et. al. also reported the creation of subgap states by exposure to simulated sunlight both for P3HT:PCBM and PCDTBT:PCBM$_{70}$ BHJs[141]. The literature collectively suggests that the photo-induced traps lead to increased SRH recombination and a consequent reduction in photo-voltage, and loss of performance. The issues we wanted to address in this experiment were the following:
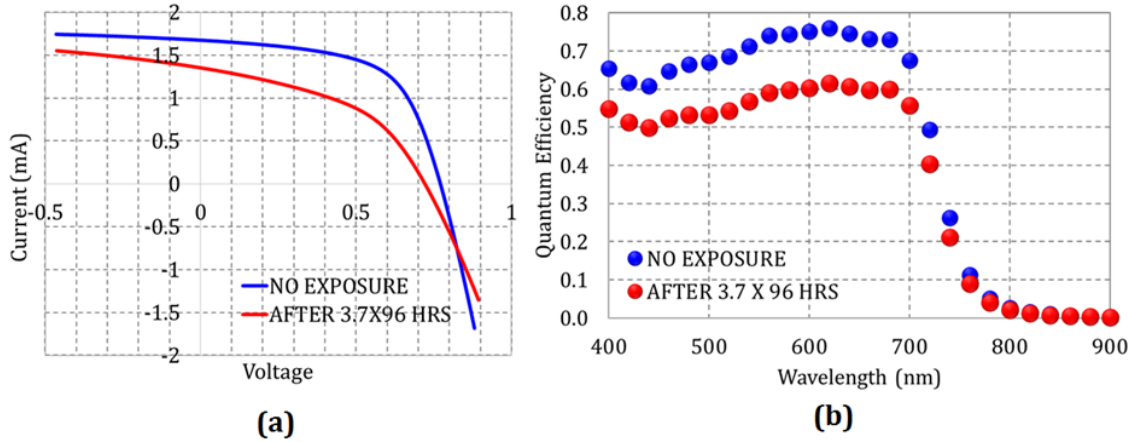
*Fig.4.17. Current-Voltage characteristics (a), and QE (b) of PTB7 cell
before and after exposure to 3.7X sun for 96 hrs.*

- Do PTB7:PCBM$_{70}$ cells degrade the same way under light? (in particular compared to the well-studied P3HT: PCBM cells).

- If yes, how do the light-induced changes lead to increased SRH recombination? Are we able to quantify the loss of photo-voltage using the multiple level trap model?

In order to address the above questions we conducted a photo-degradation experiment. We inserted a standard p-i-n sample in a N$_2$-filled glovebox to isolate moisture and oxygen. The sample was exposed to ~4X Sun intensity for 96 hours. Device characteristics were carefully measured before and after the exposure.

Fig. 4.17 shows the IV and QE curves of the degraded and control samples. Fig. 4.18 depicts the CF measurements before and after exposure. We observe that the exposure has increased the density of deep defects by a factor of ~6-7. An analysis of the corresponding dark IVs before and after light degradation (Fig 4.19) shows that recombination current has also increased by a factor of ~6 after the exposure. This agrees very well with the theory
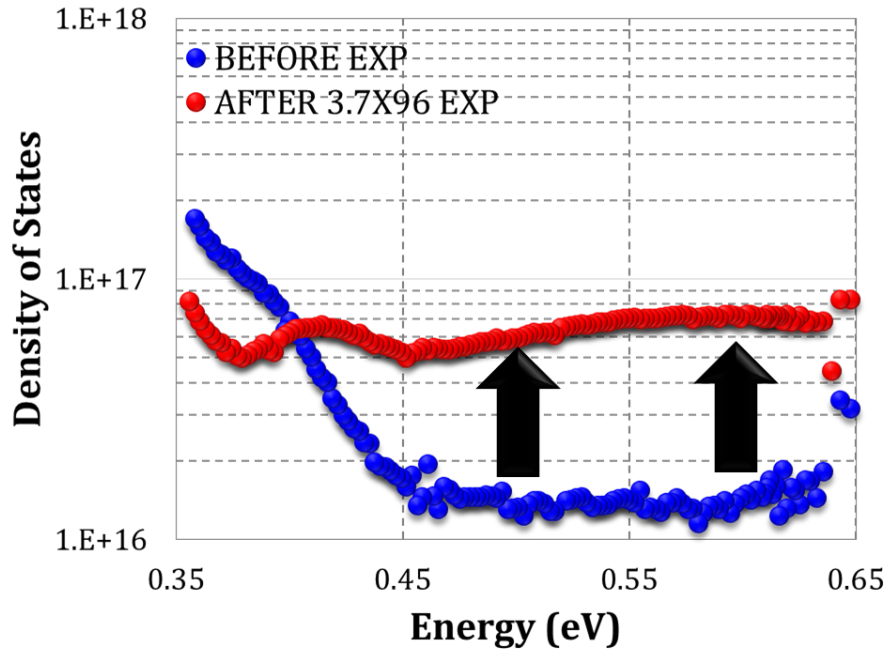
Fig. 4.18. Density of defects increase by a factor of ~5-6 after exposing the sample to 3.7X sun intensity for a period of 96 hours.

(Eq. 4.14) that an increase in deep defects leads to a similar increase in the dark saturation current. A similar correlation is reported for P3HT:PCBM cells [137].

It is also noteworthy that based on calculations, the rate equation (Eq. 4.10) predicts a drop of ~30-40 mV in photo-voltage for a 6 to 7 fold increase in the density of deep defects (N_0). This is in reasonable agreement with the experimentally-observed 40-50 mV drop in V_{oc} (Fig. 4.17).

Figs. 4.20 and 4.21 show, respectively, V_{oc} vs. Intensity and subgap spactra before and after exposure to light. Neither the ideality factor nor the Urbach energy change with exposure. This observation is consistent with the theory that ideality factor is determined by Urbach tail, and if the Urbach tail does not change with light exposure (Fig. 4.21), then the light ideality factor shouldn't change after exposure (Fig 4.20).
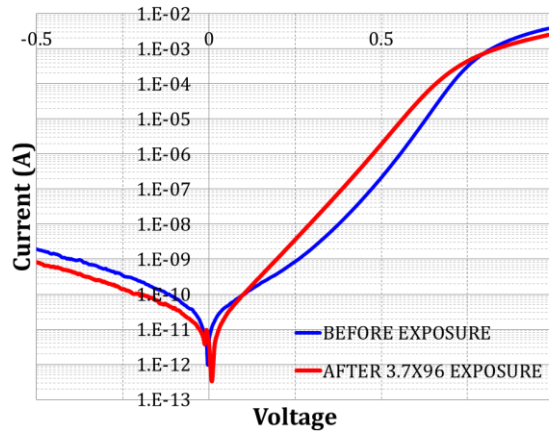
Fig. 4.19. Analysis of dark IV shows that I_0 increases from ~8×10⁻¹³ A before the exposure to ~4.8×10⁻¹²A after the exposure (enhance by a factor of ~6).
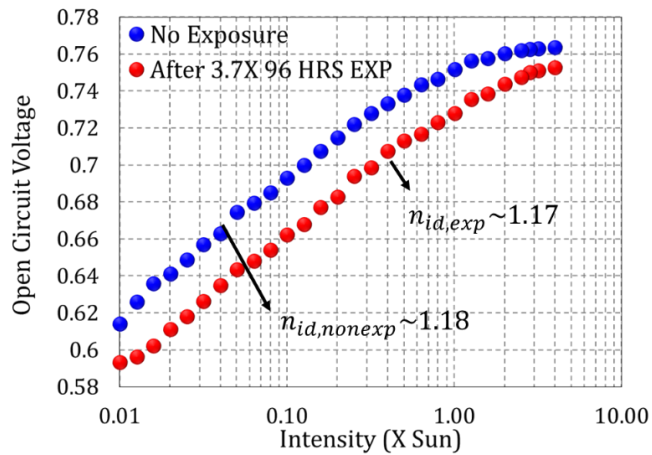
Fig. 4.20. V_{OC} vs. light intensity before and after light exposure. The light ideality factor remain unaltered (~1.2) after exposure.
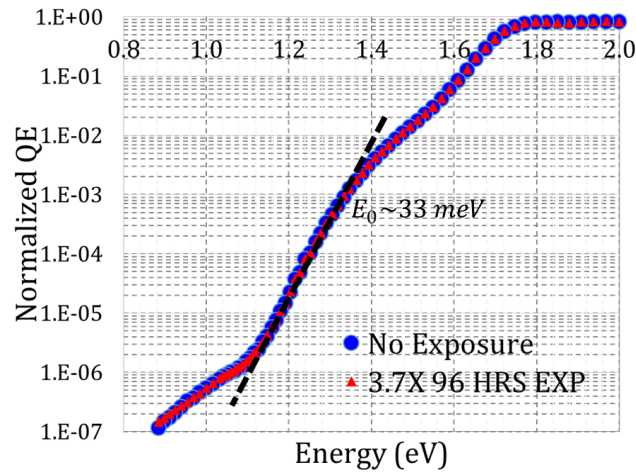
Fig. 4.21. The subgap characteristics (and therefore E_0) do not change with light exposure. This explains why the light ideality factor does not change by light exposure.

4.9. Estimating capture cross sections

A microscopic parameter of interest in device physics is the capture cross section of trap states (σ in cm^2). In this section, we present an approach for interpreting QE vs. bias data in BHJs which can be employed for getting estimates of capture cross section of the gap states. Fig. 4.22 shows the band diagram at the D/A interface.

In the QE vs. bias experiment, the collected current is what is left from generated current after taking the recombination current into account.

$$J_C = J_G - J_R \tag{4.22}$$

Where J_C, J_G and J_R are collected, generated and recombination currents, respectively. Assuming that geminate and band-to-band losses are negligible, the recombination current is mainly due to non-geminate trap-assisted recombination of carriers at the D/A interface. The flux of charge carriers that give rise to J_R are related to the density of excess charge carriers (Δn) through the following relation[142]:
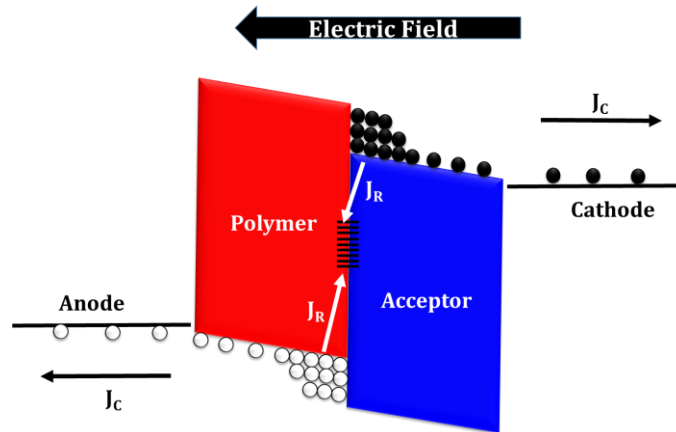
Fig. 4. 22. Energy band diagram of donor-acceptor interface.
Charge carriers that escape recombination (J_R) at the interface are collected at the contacts (J_C).

$$J_R = q. \Delta n. S \tag{4.23}$$

Where q=1.6×10⁻¹⁶ c is the unit charge, and S (cm/sec) is recombination velocity.

We also know that in QE vs. bias the sample current is dominantly due to drift:

$$J_C = q.\mu.\Delta n.\varepsilon \qquad (4.24)$$

where ε is the electric field, and μ is mobility. Combining the above equation, we obtain the ratio of collected to generated current:

$$\frac{J_C}{J_G} = \frac{\varepsilon}{\varepsilon + \frac{S}{\mu}} \qquad (4.25)$$

Which is normalized QE as a function of voltage (or electric field), the very same quantity that we measure in the QE vs. bias experiment.

The electric field is approximated by:

$$\varepsilon = \frac{V_{bi} - V}{t} \qquad (4.26)$$

Where V_{bi} is the built-in potential, V is the bias voltage and t is film thickness.

The quantity "S/μ" in Eq. 4.25 has the dimension of electric field (V/cm). Eq. 4.25 therefore expresses collection as a competition between electric fields:

1. The electric field at the D/A interface (ε) which pulls the carriers away from the interface.

2. An imaginary Electric field (=S/μ) which forces the carrier to go back to the interface and get recombined. The magnitude of this imaginary field is a function of carrier mobility and surface recombination velocity, which is proportional to density and capture cross-section of interfacial states.
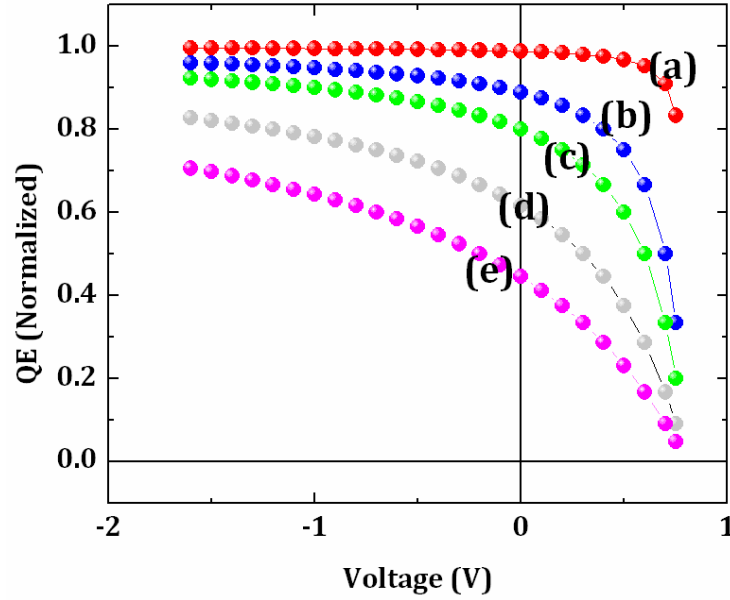
Fig. 4. 33. QE vs. bias as calculated by Eqs. 4.26 and 4.27 for S= (a) 0.1, (b) 1, (c) 2, (d) 5, and (e) 10 cm/sec, assuming μ=10⁻⁴ cm²/V.sec, V$_{bi}$=0.8 V, t=100 nm.

Fig. 4.23 shows normalized QE as a function of applied voltage for a wide range of surface recombination velocities. In this case, we assumed V_{bi}~0.8 V, μ~10^{-4} cm².V⁻¹.sec⁻¹ and device thickness of ~100 nm.

The surface recombination velocity (S) is[142]:

$$S = v_{th}.\sigma.N_{Ts} \tag{4.27}$$

Where v_{th} is the thermal velocity of carriers and is ~10^7 cm/sec[143], σ is the capture cross section of traps (in cm²) and N$_{Ts}$ is the surface density of states at the D/A interface (in cm⁻²). We can derive N_{Ts} from the DOS data measured by CF measurements:

$$N_{Ts} = \frac{\text{Domain volume}}{\text{Domain Surface}} \times \int_{midgap} N(E).dE \tag{4.28}$$

The volume to surface ratio is necessary to convert the bulk defect density (cm⁻³) to surface defect density (cm⁻²). Aassuming spherical domains this ratio is estimated to be:

$$\frac{\text{Volume}}{\text{Surface}} = \frac{\frac{4}{3}\pi r^3}{4\pi r^2} = \frac{r}{3} \tag{4.29}$$
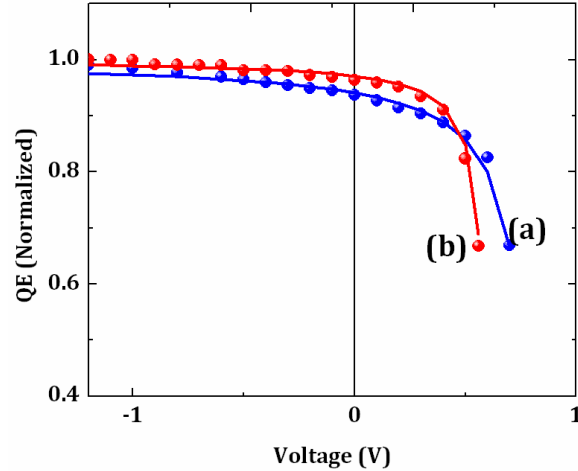
Fig. 4. 24. Experimental (circles) and theoretical (solid lines)
QE vs. Bias for PTB7:PCBM$_{70}$ (a) and P3HT:PCBM$_{60}$ (b).

With r being the domain radius, which for an optimized morphology is roughly equal to the exciton diffusion length (r~10 nm).

Thus, by measuring S from QE vs. bias and N_{Ts} from CF, one can get an estimate of capture cross section. Fig. 4.24 shows the QE vs bias for standard PTB7:PCBM$_{70}$ and P3HT:PCBM$_{60}$ cells. By fitting Eq. 4.25 to these result we find out that S is ~0.6 and ~2.5 cm/sec, respectively, for P3HT and PTB7 cells.

For the P3HT cells, knowing that $N(E)$~10^{15} cm^{-3}.eV^{-1} in the midgap region, we obtain: σ~ 10^{-16} cm^2, which is almost exactly what MacKenzie et. al.[144] have obtained for electron capture cross section in P3HT: PCBM cells. In the case of PTB7, on the other hand, the density of defects in the midgap region is $N(E)$~10^{16} cm^{-3}.eV^{-1}. Assuming S=2.5 cm/sec, this will result in σ~10^{-16} cm^2. Carr et. al. have also obtained similar values for P3HT and PTB7 blends from their capacitance spectroscopy measurements [145].

4.10. Summary of chapter 4

In short:

- We report on fundamental electronic properties of PTB7:PCBM$_{70}$ BHJs. CF measurements show that the blend has a deep defect density of $\sim 10^{16}$ eV^{-1}.cm^{-3}. Moreover, subgap QE reveals an interfacial bandgap of ~ 1.35 eV, and band tails with an Urbach energy of 33 meV.

- We used an analytical approach based on a multiple-level trap model to compute recombination rates in PTB7:PCBM$_{70}$ devices. The computations match the experimental data with reasonable accuracy, and the model can explains fundamental device characteristics.

- A high shunt is observed in the dark IV of un-annealed PTB7:PCBM$_{70}$ devices. This current could be due to shunt paths that are created by residual solvent in the film. The resulting parasitic shunt current obscures the information in dark IV.

- Proper heat treatment at low temperatures (~ 80 C) is essential in eliminating the parasitic shunt current in PTB7:PCBM$_{70}$ BHJs. Once shunt current is eliminated the multiple-level trap model precisely predicts ideality factors, the values of recombination current, and explains its dependence on temperature and density of deep defects.

- Trap-assisted non-geminate recombination is the dominant recombination mechanism.

- Quasi-fermi level pinning to the band tails under illumination is the main limiting factor for the photo-voltage.

- We made a few assumptions that limit the application of our multiple-level model to D/A blends for which the assumptions hold. The most important of these conditions are:

  1. Balanced transport, i.e. we assumed that electron and hole mobilities are close, and are roughly 10^{-4} cm^2/V.sec. This means the current model cannot be applied to a blend such as P3HT:ICTA, where mobility of electrons in ICTA is ~2 orders of magnitude less than hole mobility in P3HT [146, 147]. This difference leads to build-up of holes in the device, and the n~p assumption does not hold under equilibrium. More importantly, the charge build-up distorts the internal electric field. The QE vs. Bias method for estimating capture cross-sections will, therefore, be invalid because charge accumulation modifies the distribution of electric field, and the linear approximation of Eq. 4.26 cannot be used anymore.

  2. DOS is assumed to be symmetric with respect to the mid-gap point.

  3. Geminate loss is negligible. Some studies on blends such as PCPDTBT:PCBM [148, 149] have suggested that geminate loss may constitute a significant part of total recombination in those device. In that case, the model we presented here ought to be modified to include an additional term to count for bias dependence of charge generation.

CHAPTER V

HYBRID STRUCTURES FOR IMPROVED STABILITY

5.1. a-Si as electron transport layer for improving photo-stability

In the previous chapter, we showed that prolonged exposure to light creates deep defects inside the bandgap of the bulk heterojunction. It is proposed that these defects are created when more energetic photons arrive at the main layer, and cause the weaker bonds (probably primarily C-H bonds) to break[140, 150] . The increased recombination due to these light-induced defects reduces open-circuit voltage and degrades carrier collection [137, 138, 140, 150].

One approach to enhance the stability of the cells is, therefore, to prevent the highly energetic photons in the blue region of the spectrum to reach the organic layer. UV and blue filters are employed to block the blue photons which has resulted in enhanced photo-stability[151].

An alternative approach is to improve photo-stability by modifying device structure such that highly energetic photons are blocked at the front contact before reaching the organic layer. A wide bandgap material whose energy levels are suitable for extracting charge carriers from the photo-active layer has to be used for this purpose. Hydrogenated amorphous silicon (a-Si:H) is one candidate that matches this description. It has a bandgap of ~1.8 eV, which is capable of absorbing UV and blue lights (See, for example, ref. 69). Moreover, its electron affinity of ~4.0 eV[152, 153] almost perfectly matches PCBM LUMO. An n+/a-Si can, therefore, be used as ETL for P3HT:PCBM BHJ. Fig. 5.1 shows our proposed device structure[154], and relevant energy levels of materials. MoOx/Al and ZnO interlayers
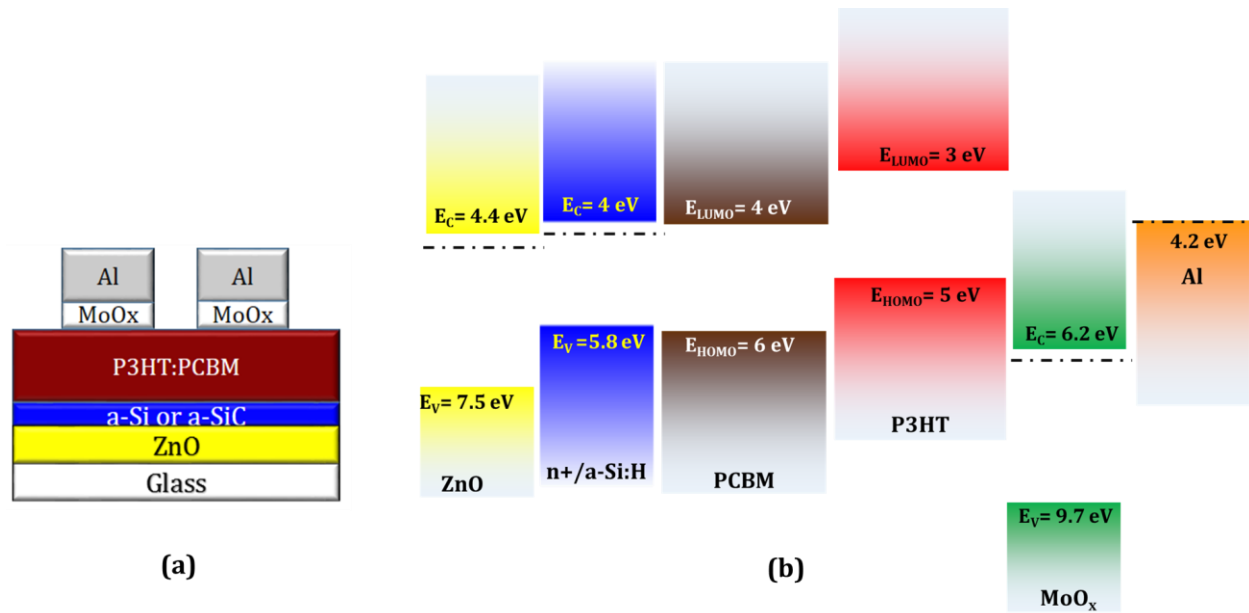
Fig. 5. 1. Device structure (a) and energy levels of the materials (b) in the hybrid n-i-p device for improved stability. Values taken from[152, 153, 155].

are used to make ohmic contacts to P3HT and n^+/a-Si, respectively. Hereafter, we will refer to this structure as "hybrid cell".

Another advantage of using an a-Si interlayer is that it is role-to-role compatible[156]. Moreover, since it is relatively inert to oxygen and moisture, a-Si helps eliminating stability issues arising from commonly used organic interlayers (For instance, PEDOT:PSS etching ITO substrate resulting in diffusion of tin and indium into the main layer and thereby degrading the cell[157]. Another example is diffusion of Cs into organic layer[158, 159] when using Cs_2CO_3 as ETL). Another advantage of a-Si is the possibility of carbon incorporation to form amorphous silicon carbide (a-(Si,C)) with higher bandgaps[160, 161]. By changing the carbon content we can tune the bandgap of the interlayer which determines the cut-off wavelength for blocking photons.

5.1.1. Device Fabrication

Fig 5.1 (a) shows our proposed structure. First, 100 nm of ZnO was deposited on

clean glass substrate using RF plasma sputtering. Then a silane-hydrogen mixture was used in a Plasma Enhanced Chemical Vapor Deposition (PECVD) reactor to deposit a thin layer (20-30 nm) of a-Si:H on top of sputtered ZnO. Phosphine gas was introduced during a-Si:H deposition to dope it n+. The resulting n+/a-Si:H serves as ETL in the hybrid structure. Then the substrate was transferred into a N_2 glove-box, where P3HT:PCBM bulk heterojunction was deposited on top of a-Si:H by spin-coating at 500 rpm for 60 seconds. The precursor for the bulk heterojunction was a mixed solution of P3HT (17 mg/ml) and PCBM (17 mg/ml) in dichlorobenzene, stirred at 70C for 24 hrs before use. The deposited film was then slowly dried for 1 hour under a petri-dish. The device was then thermally annealed on hot-plate at 160 C for 2 min, followed by 110C for 20 mins. MoO_x (20 nm) and Aluminum (100 nm) were thermally evaporated through circular shadow masks to form the anode, and complete the device. The geometrical area of anode is 0.106 cm^2.

In order to compare the light stability of our hybrid cell with standard organic cells in the literature, a reference n-i-p device was made on ITO-coated glass substrate for comparison. The structure of this cell, which has Cs_2CO_3 as ETL, is depicted in Fig. 5.2. ETL is deposited by spin-coating 2 wt% solution of Cs_2CO_3 in 2-Ethoxyethanol at 5000 rpm. The sample is then annealed at 180 C for 25 minutes in air before being transferred into N_2 glove-box. Rest of the fabrication process is same as in hybrid cell. Thicknesses of P3HT:PCBM layers are measured using profilometry and Atomic Force Microscopy (AFM), and are roughly 150 nm for both the reference and the hybrid cells.
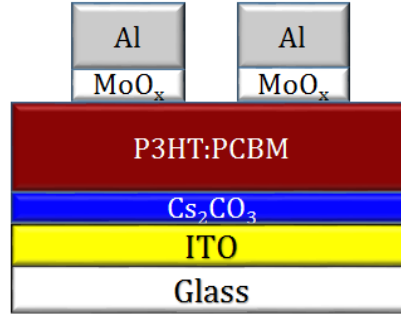
Fig. 5. 2. Reference n-i-p cell with Cs₂CO₃ as ETL.

5.1.2. Device Characteristics

The IV characteristics of the reference and the hybrid cells are shown in Fig 5.3 (left). The photo-voltage and fill factor of the hybrid cell is marginally higher compared to the standard cell. The short circuit current is, however, lower due to absorption of low wavelength photons in the a-Si:H cathode. This can be understood by comparing the QEs, depicted in Fig 5.3 (right).

The defect densities obtained from CF measurements (Fig. 5.4 - left) show that both cells are very similar in terms of density of deep defect. Moreover, the subgap QE spectra (Fig. 5.4 - right) reveal that the two morphologies possess identical D/A bandgaps and have
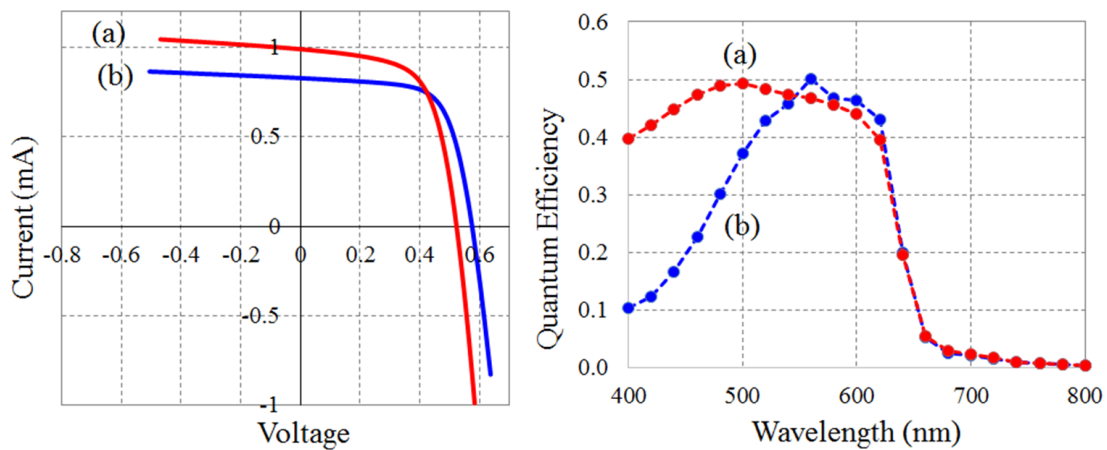
Fig. 5. 3. IV characteristics (left), and QE (right) of a standard (a), and hybrid (b) n-i-p organic solar cell.
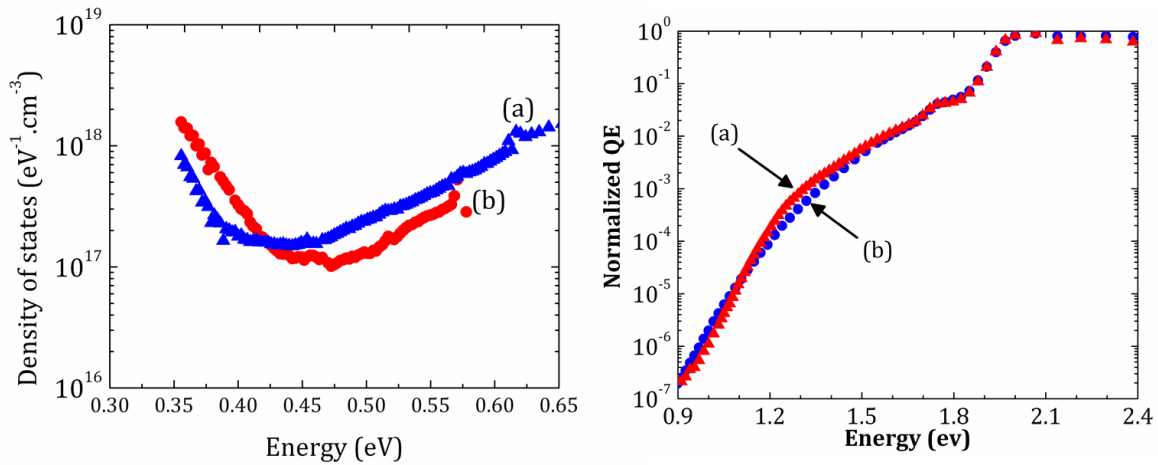
Fig. 5. 4. DOS (left) and subgap QE (right) of the hybrid (a) and standard (b) n-i-p solar cells.

similar Urbach tails. The P3HT:PCBM BHJs deposited on n+/a-Si and Cs2CO3 are, therefore, of similar fundamental electronic characteristic, and can be compared for their relative stability.

5.1.3 Stability Measurements

Cell stability is assessed by in-situ measurements of IV characteristics of the devices under accelerated degradation conditions (2X Sun for 48 hours). A N_2-filled environmental chamber is used to create an inert atmosphere, where the cells are exposed to 2X simulated sunlight, and IV characteristics are measures over the exposure period (48 hours). The structure of the environmental chamber, and standard operating procedure for loading/unloading samples into/out of this chamber are described in detail in our earlier works[162]. When measuring stability of the hybrid cell, the light intensity was increased slightly beyond 2X such that the initial short circuit current of the hybrid cell is equal to that of the standard cell. This is because a-Si:H ETL absorbs part of the incident light, and
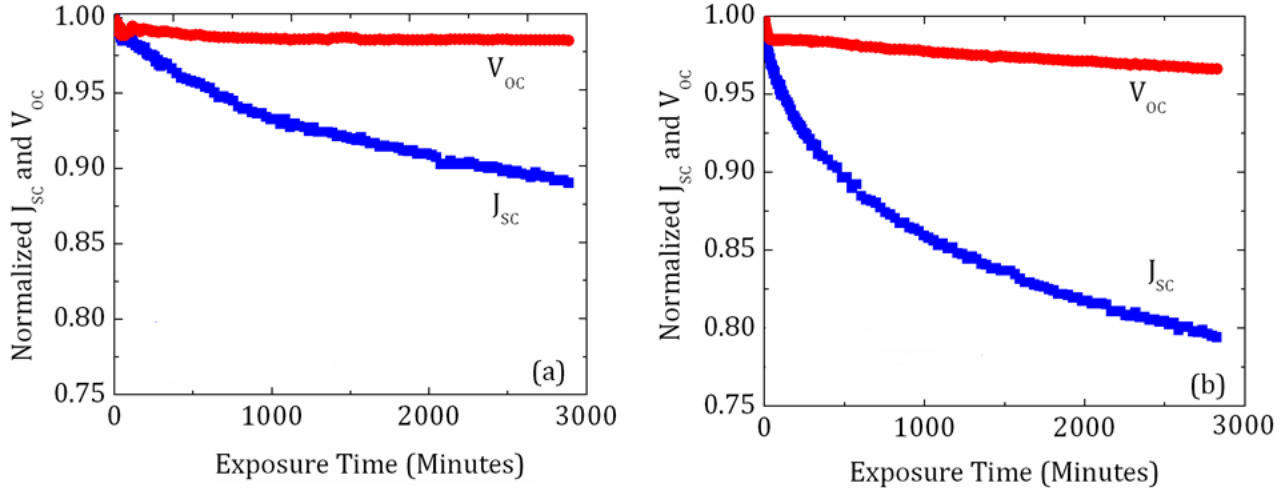
Fig. 5. 5. Normalized V_{oc} and J_{sc} of hybrid (a), and standard (b) n-i-p solar cells as a function of time upon exposure to 2X sun for 48 hours.

therefore photon flux in the P3HT:PCBM layer is higher in standard cell compared to the hybrid cell, if the intensity of incident light is equal for both of them. By increasing the light intensity about ~20% in the case of hybrid cell, we ensure that number of photons that are entering the light-absorbing blend is roughly the same in both cells. The in-situ IV characteristics were recorded, and the results are shown in Fig.5.5. The V_{oc} and J_{sc} of the hybrid cell exhibit significantly less deterioration compared to that of the standard cell. Moreover, unlike the standard cell, the photo-voltage stabilizes after a small initial drop when a-Si is used as ETL.

Fig. 5.6 shows the DOS of both cells before and after exposure to 2X sun light. While there is virtually no change in the DOS of hybrid cell, the increase in the electronic defect population in the standard n-i-p cell is evident.

Our results clearly demonstrate that using a stable inorganic material such as a-Si:H as ETL in organic solar cells yields an organic main layer with similar electronic properties. However, the highly energetic photons (blue and UV) are blocked when such material is
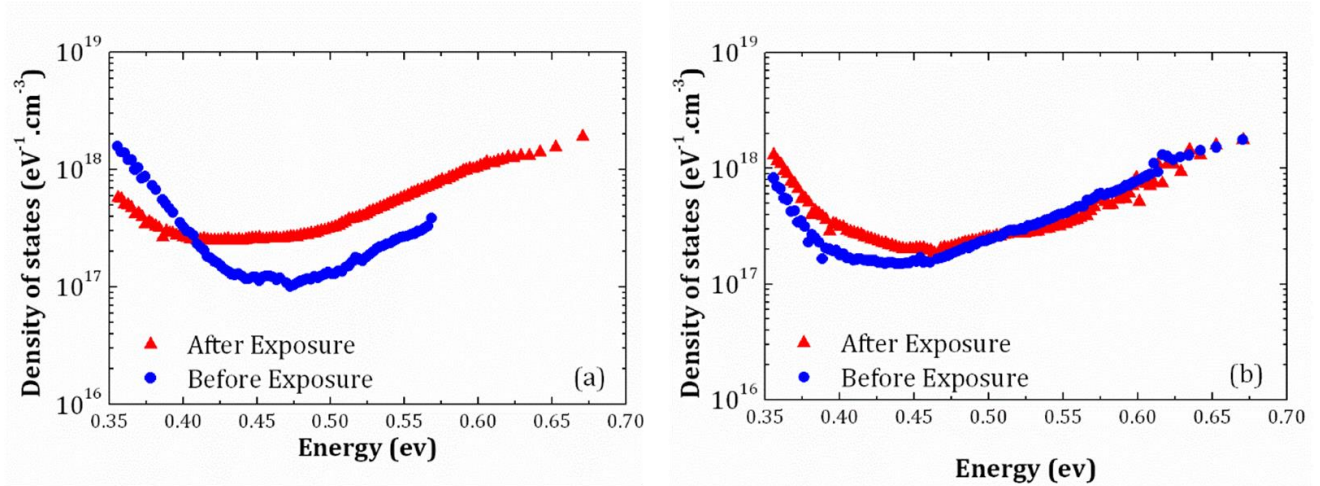
Fig. 5. 6. Density of defects for standard (a), and hybrid (b) n-i-p BHJ cells
before (blue), and after (red) 2X sun exposure for 48 hours.

used as front contact, hence less electronic defects are created in the material, and photo-stability is enhanced.

It is evident from the QE data (Fig. 5.3) that high-energy photons are lost to recombination in the n^+/a-Si layer, and thus do not contribute to the external current. One approach to reduce this loss could be to increase the bandgap of the ETL by, for example, incorporating carbon in a-Si:H, thus forming a-(Si,C):H (hydrogenated amorphous silicon-carbide). This is possible by simply introducing small amounts of CH_4 into the PECVD reactor when growing the ETL on ZnO substrate. The ETL bandgap widens as a result, thereby increasing QE at lower wavelengths. This is shown in on Fig.5.7 (left) for different amounts of incorporated carbon.

Unfortunately, however, with increasing CH_4, a non-ohmic behavior arises in the JV characteristics of the devices (Fig. 5.7–right), which is probably due to lowered incorporation of dopants in the amorphous layer at increased CH_4 flow[154], leading to development of a barrier in the front contact.
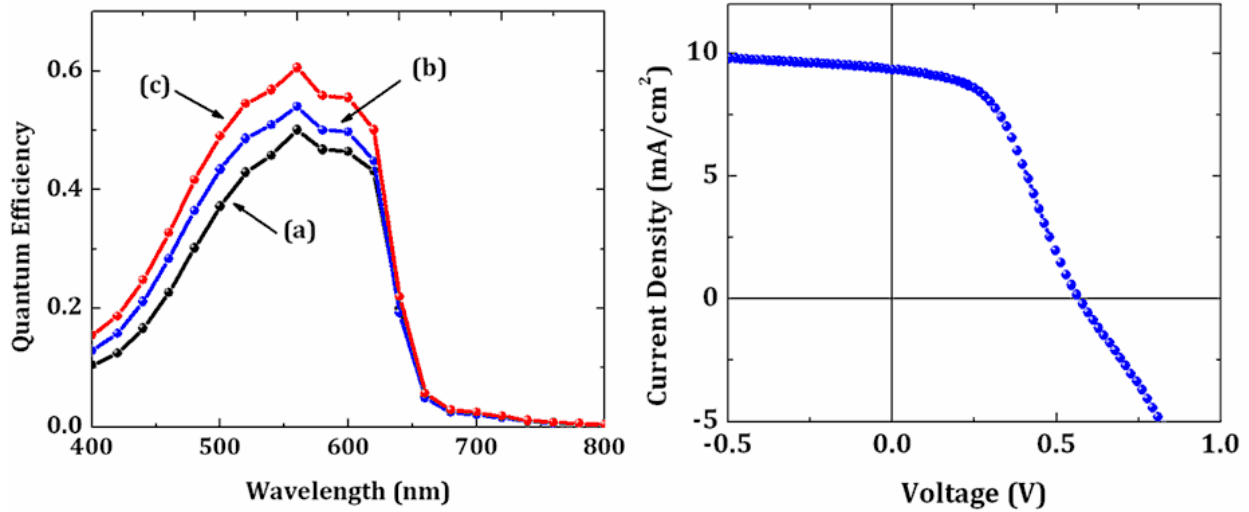
Fig. 5. 7. Left–QE of hybrid P3HT:PCBM cells for different CH_4 flow during growth of ETL in PECVD reactor: (a) 0, (b) 3, and (c) 6 sccm. Right–With 6 sccm CH_4 flowing during ETL growth a barrier emerges in in the JV characteristic.

Nonetheless, this approach can be utilized for tuning the bandgap of ETL, and achieving higher currents in other organic cells with hybrid interfaces. We repeated a similar set of experiments on PTB7:$PCBM_{70}$ blend. JV and QE of the optimized device with a-(Si,C) ETL is shown in Fig. 5.8. The PCE of the optimized cell is ~4.2%, which is ~3% less
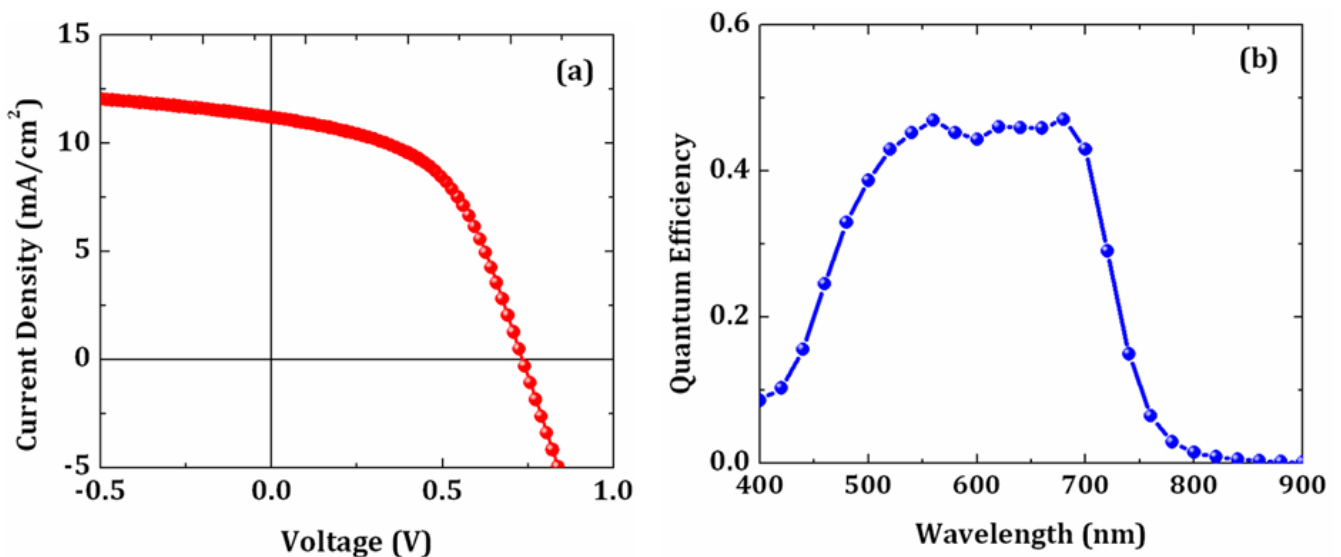
Fig. 5. 8. (a) JV charcateristics, and (b) QE of a PTB7:PCBM70 hybrid cell with a-(Si,C):H ETL. The optimized performance was obtained for 6 sccm of CH4 flow during ETL growth.

than the efficiency expected from a standard PTB7:PCBM$_{70}$ BHJ (7%-8%). This loss of performance due to front contact absorption could be compensated in a tandem structure, where the incoming light first filters through a higher band-gap inorganic cell (e.g. a-(Si,C):H cell)before entering the bulk heterojunction. This way the high energy photons are converted to current in the a-(Si,C):H front cell, and result in higher efficiencies. Such tandem devices are discussed in the next section.

5.2   Tandem Solar Cells

In chapter 1, we discussed thermodynamic and absorption losses, and further elaborated on how a compromise between the two sets an upper limit to the PCE of a single junction solar cell (SQ limit). In order to achieve efficiencies above SQ limit, more than one junction should be used. Such multi-junction devices are called tandem cells. In this section, we first provide a brief background on tandem devices, before moving forward and presenting our results on organic-inorganic hybrid tandems.

Fig. 5.9 (a) shows the idea of a multiple-junction tandem device[163]. A tandem cell is a stack of solar cells whose bandgaps are sorted such that the widest bandgap cell is at the front, and the smallest bandgap is in the back. The light enters the front cell where the high energy photons are harvested. The lower energy photons that pass through the first cell are absorbed in subsequent cells as they encounter smaller bandgaps in their travel through the structure. Fig. 5.9(b) shows an example of a double-junction tandem cell in more detail[164]. Both cells are p-i-n, and are electrically connected through a semi-transparent intermediate layer, which is an n$^+$/p$^+$ tunnel junction. Ideally, light absorption in the two cells is complementary, i.e. the front cell absorbs shorter wavelengths, and the back cell
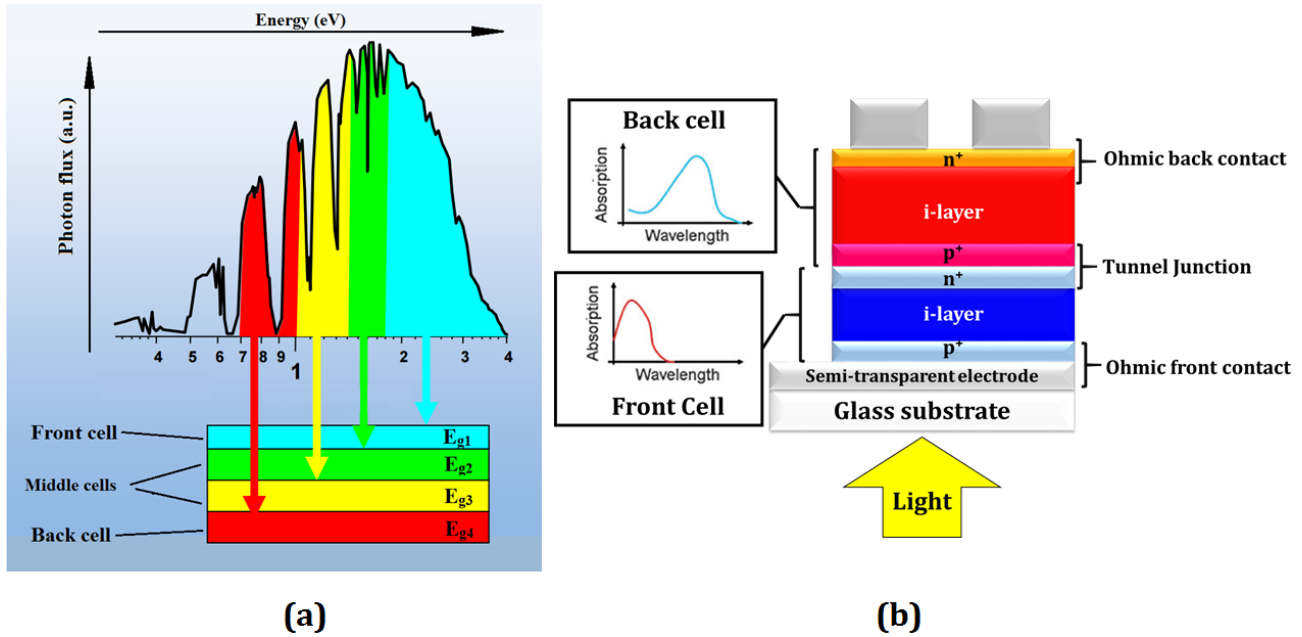
Fig. 5. 9. (a) Solar spectrum (top) gets absorbed in a multi-junction tandem solar cell (bottom). The bandgaps are arranged such that $E_{g1} > E_{g2} > E_{g3} > E_{g4}$. (b) A double-junction solar cell with complementary absorption.

absorbs longer wavelengths. A sample band diagram of a double-junction tandem cell is depicted in Fig. 5.10[165]. The positive and negative charge carriers are collected in the front and back contacts, respectively. Electron current from the front cell and hole current from the back cell meet and recombine at the intermediate tunnel junction. Charge neutrality forces the device current to be equal to the smaller of the two. The photo-voltage is equal to the sum of V_{OC}s of the two cells.

In the case of organic BHJs, we showed that blocking high-energy photons reduces the photo-induced damage in D/A interface, and thereby improves light-stability. This can be achieved by using a higher bandgap cell (such as a-Si or a-(Si,C)) in tandem with an organic BHJ. In that case, the tandem structure is not only a pathway for higher efficiency, but could also be considered as an approach to improved photo-stability. The a-(Si,C)/BHJ tandem has, therefore, been under intensive investigation in the past few years.
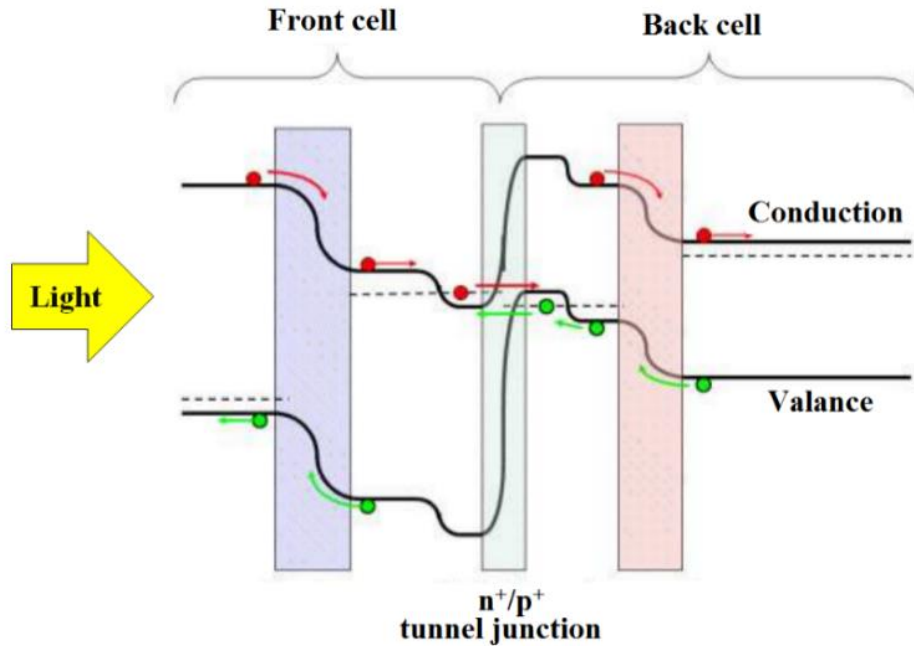
Fig. 5. 10. Example band diagram of a double-junction tandem solar cell. Adopted with modifications from.

In an earlier work in our group, Pattnaik et. al. made an a-(Si,C)/P3HT:PCBM tandem cell. By using P3HT:PCBM$_{60}$ BHJ, they could successfully harvest the solar spectrum upto a wavelength of ~700 nm, and achieve a PCE of ~5.7% [166]. In the next step towards higher performances, we selected PTB7:PCBM$_{70}$ BHJ as our back cell, which enables us to convert photons to current upto a wavelength of ~800 nm. In the next section, we discuss the fabrication details of an a-(Si,C):H/PTB7:PCBM$_{70}$ BHJ tandem cell.

5.2.1 Fabrication of a-(Si-C):H/PTB7:PCBM$_{70}$ tandem cell

The structure of the cell is shown in Fig. 5.11. First 100 nm of Al: ZnO was deposited on glass substrate using RF plasma sputtering. Then a p-i-n a-(Si,C):H cell was fabricated using PECVD technique. A ~70 nm ITO was then deposited using plasma sputtering to cap the front cell. Afterwards, a very thin layer of PEDOT:PSS (~30-40 nm) was deposited by
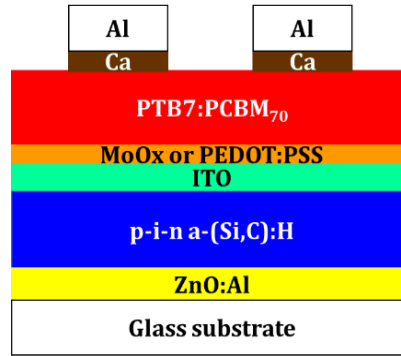
Fig. 5. 11. Device structure of a-(Si,C):H/PTB7:PCBM70 BHJ solar cell.

spin-coating at 4000 rpm for 60 sec. This was followed by thermal annealing at 150C for 20 minutes in air. Then the device was transferred in N_2-filled glovebox for making the back cell. The PTB7:PCBM$_{70}$ BHJ was deposited through spin-coating at 1000 rpm/60 sec inside the glovebox, and the sample was annealed at 80 C for 15 minutes. The device was completed by evaporating calcium (20 nm) and aluminum (100 nm) on top of the organic layer. Similar devices was made where the PEDOT:PSS interlayer was substituted with ~30 nm of thermally evaporated MoO_x as interlayer. The MoO_x- covered substrate was annealed at ~150C for 15 minutes in N_2-filled glovebox before deposition of PTB7:PCBM$_{70}$ blend.

5.2.2 Device characteristics of a-(Si-C):H/PTB7:PCBM$_{70}$ tandem cell

Fig. 5.12 (left) shows the JV characteristic of the front and the back cells. JV characteristics of the tandem is shown in Fig. 5.12 (right). The corresponding device characteristics are listed in table 5.1. The photo-voltage of the best tandem is almost equal to the sum of the photo-voltages of a-(Si,C):H and PTB7: PCBM$_{70}$ cells, indicating minimized loss due to shunt paths. A high PCE of ~7.6% is obtained, which is among the highest
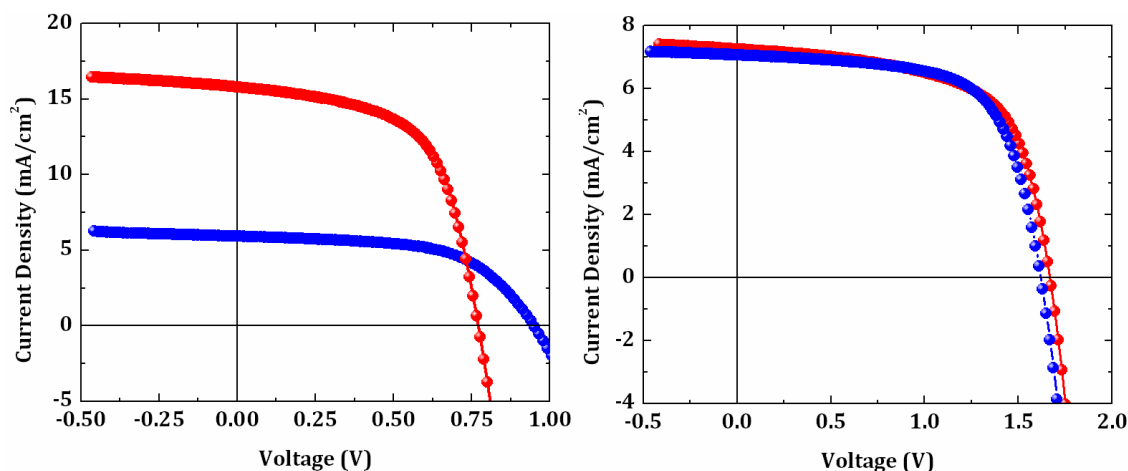
Fig. 5. 12. Left–JV characteristics of single junction p-i-n PTB7:PCBM70 (red) and a-(Si,C):H (blue) cells.
Right– JV characteristics of tandem cells of Fig. 5. 11 with MoOₓ (red) and PEDOT:PSS (blue) interlayers.

Table 5. 1. Cell performances for single junction and tandem cells shown in Fig. 5.12.

Cell	Structure	Voc (V)	Jsc (mA/cm²)	FF (%)	PCE (%)
PTB7:PCBM$_{70}$	ITO/PEDOT:PSS/PTB7:PCBM70/Ca/Al	0.77	15.8	59.9	7.3
a-(Si,C):H	Al:ZnO/p⁺– (a-Si,C):H/i–(a-Si,C):H/n⁺–(a-Si,C):H/ITO	0.94	7.58	59.4	4.2
Tandem	with PEDOT:PSS interlayer	1.62	7.04	66.5	7.6
Tandem	with MoOx interlayer	1.67	7.26	63	7.6
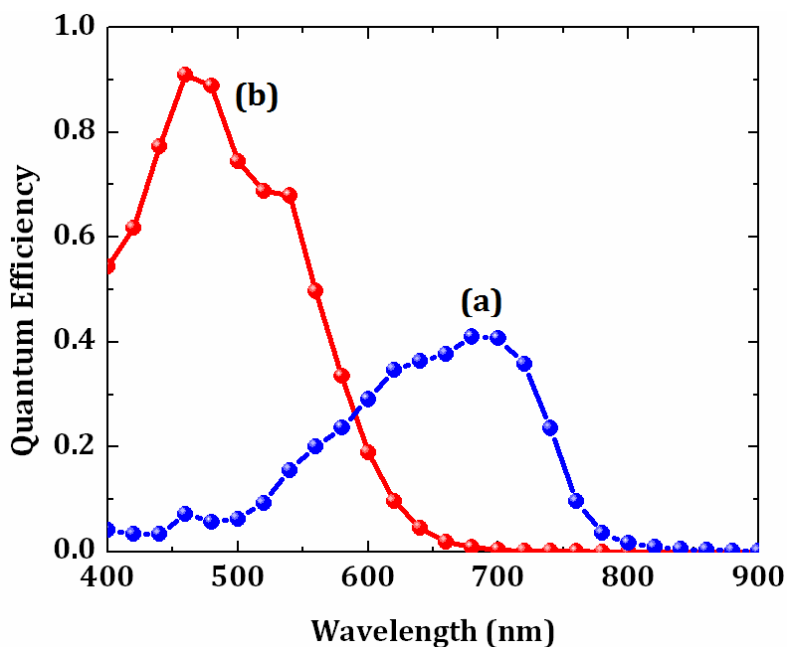
Fig. 5. 13. Quantum efficiency of tandem cell measured under blue (a), and red (b) bias lights.

reported in the literature.

Fig. 5.13 is the QE of the front and back cells. To measure the QE of the front cell (a-(Si,C):H), we first measured the sample's QE while it was flooded with red bias light. Under red light the PTB7:PCBM$_{70}$ BHJ is saturated, and the measured QE is that of the front cell. Then we measured QE under blue bias light, which saturates the a-(Si,C):H cell, and yields the QE of the back cell. The QE data indicates a current mismatch between the two cells, and demonstrates that the PTB7:PCBM$_{70}$ BHJ is limiting the current. In order to confirm this, we also measured the JV characteristics under blue- and red-shifted simulated sunlight. First, the JV characteristic was measured under simulated sunlight (1X intensity). Then, we added a red LED to the setup, and measured sample's JV while illuminated under both 1X sun white light and the red LED. We then replaced the red LED with a blue LED of the same photon flux, and measured the JV again while the sample was co-illuminated under 1X sun white light and the blue LED. The photon fluxes of the additional red and blue lights were set to be equal by using a reference crystalline silicon photodiode. The LEDs were adjusted such that the reference signal was equal under red and blue lights, while the white light intensity was kept at ~1X Sun at all times during the experiment. The measurement results are depicted in Fig 5. 14. We observe that while adding a known dose of blue photons to the incident light increases J_{SC} by only~5%, adding the same number of red photons to the spectrum leads to an enhancement of ~32% in J_{SC}. This is further evidence that the short circuit current in tandem cell is limited by the PTB7 cell. These results indicates that the pathway to improve cell's current and, thereby, performance is to use a lower bandgap which can absorb at higher wavelengths compared to PTB7.
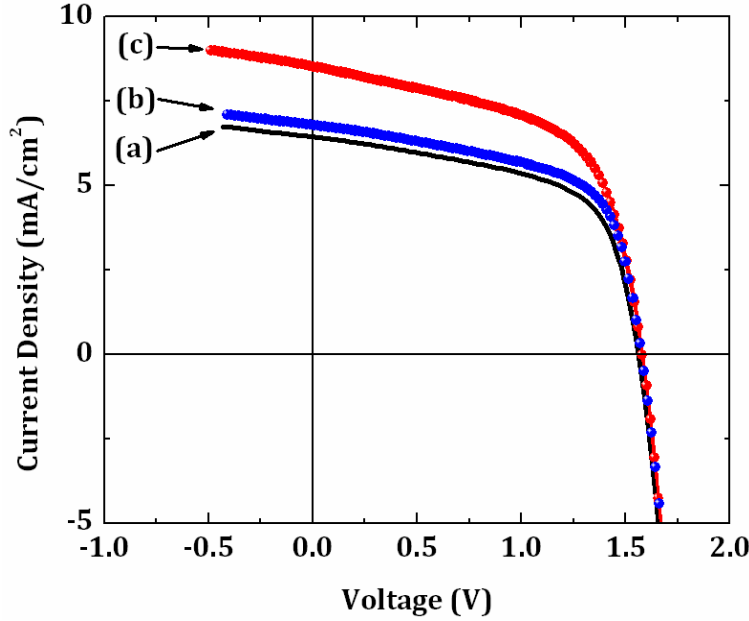
Fig. 5. 14. JV characteristics of the tandem cell measured under
(a) 1X simulated sun light, and with additional (b) blue, and (c) red LED light.

Table 5.2- Recent literature results on a-Si/BHJ hybrid tandem solar cells.

Authors	Structure	Voc (V)	Jsc (mA/cm²)	FF (%)	PCE (%)	Reference
Kim et. al.	a-Si/PDTP-DFBT:fullerene	1.54	9.8	69.2	10.5	167
Dalal et. al.	**a-Si/PTB7:PCBM$_{70}$**	**1.67**	**7.26**	**63**	**7.6**	**168**
Albrecht et. al.	a-Si/Si-PCPDTBT:PCBM$_{70}$	1.47	7.5	69	7.6	169
Qin et. al.	a-Si/PDPP3T:PCBM$_{70}$	1.5	6.5	72.3	7.5	170
Pattnaik et. al.	a-Si/P3HT:PCBM$_{60}$	1.5	5	77	5.7	166
Seo et. al.	a-Si/PBDTTT:PCBM	1.42	6.8	58	5.7	171
Kim et. al.	a-Si/PCPDTBT:PCBM$_{70}$	1.51	4.9	44.1	3.3	172
Park et. al.	a-Si/PSBTBT-co-PCDTBT:PCBM$_{70}$	1.15	3.9	70	3.1	173

Table 5. 2 summarizes the reported efficiencies for a-Si/BHJ hybrid tandem solar cells in literature. In the most recent work, Kim et. al. used the exact same device structure as we report here (Fig. 5.11) to achieve higher efficiencies[167]. Instead of PTB7, however, they used a lower bandgap polymer (PDTP-DFBT) as the main light-absorber in the back

cell. This material has a bandgap of 1.38 eV and can absorb light up to 900 nm[174]. Using this lower bandgap polymer, they improved J_{SC} to 9.8 mA/cm^2, and achieved an overall PCE of ~10.5%.

CHAPTER VI

FUNDAMENTAL DEVICE PROPERTIES OF LEAD HALIDE PEROVSKITE SOLAR CELLS

6.1   Introduction

Lead-halide perovskites have attracted significant attention from the photovoltaic community in the past few years. Their efficiencies have rapidly climbed from 3.8% in 2009 [175], to 20.1% in 2014 [12]. They offer very high absorption coefficients ($\sim 10^5$ cm^{-1})[176] comparable to that of organic compounds. However, unlike organics, high dielectric constants of perovskites[177] limit exciton binding energy to ~ 50 meV [178,179], ensuring thermal decomposition of excitons. Moreover, large carrier diffusion lengths (100 of nanometers) are measured for both electrons and holes in these materials[180,181,182]. Overall, perovskite-based solar cells combine high light absorption of organic cells with superior carrier transport properties of traditional inorganic thin-film solar cells.

In this chapter, we investigated the fundamental electronic and device properties of methyl-ammonium lead iodide perovskite solar cells. QE and subgap QE techniques are used to obtain the bandgap and Urbach energy of tail states, respectively. Then we used CF to measure DOS. CFT measurements were used to reveal the defect bands, and determines the attempt-to-escape-frequency of the traps. This work provides insight into fundamental device properties of perovskite cells, which is essential in understanding device physics and modeling.

6.2.   Crystal and band structures of lead halide perovskites

Fig. 6.1 shows the cubic perovskite structure[183]. In this figure, A and B are cations, and C is
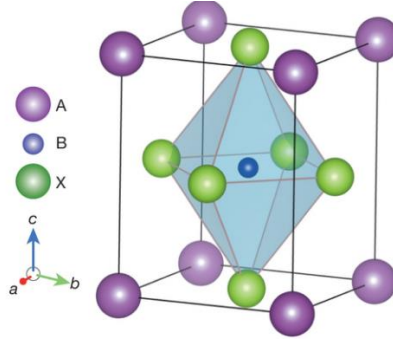
Fig. 6. 7. Perovskite structure has a general formula of ABX₃, where A and B are anions, and X is a cation.
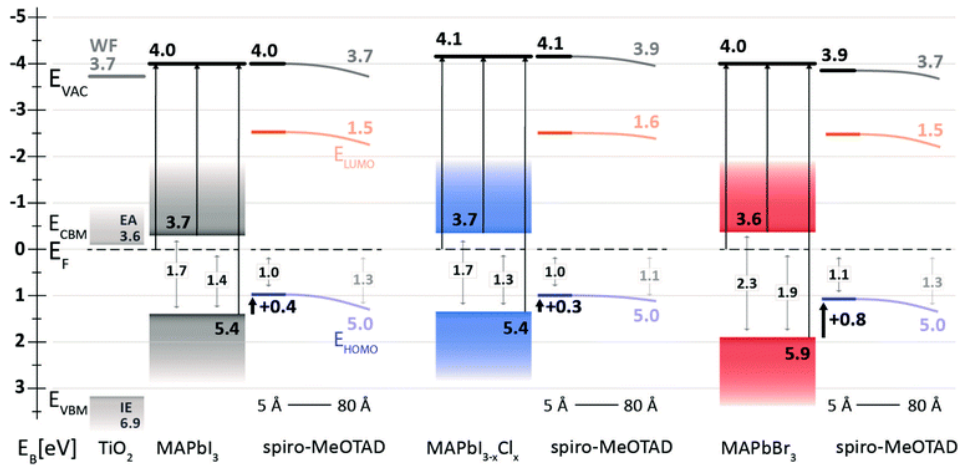
Fig. 6. 8. Energy levels of MAPbI₃, MAPbI₃₋ₓClₓ, and MAPbBr₃ given with measured to vacuum level (E_vac). The dashed line is the Fermi level. Energy levels of TiO₂ (ETL) and Spiro-MeOTAD (HTL) are also shown.

anion. The general chemical formula for perovskites is ABX_3 (example: calcium titanium oxide ($CaTiO_3$)).

In photovoltaics perovskites, A and B are, respectively, methyl ammonium ($CH_3NH_3^+$ denoted by MA) and lead (Pb) cations, and X is a halide (I^-, Br^-, or Cl^-). The resulting compounds are $MAPbI_3$, $MAPbBr_3$, and $MAPbI_{3-x}Cl_x$. Experimentally obtained energy levels of these compounds are depicted in Fig. 6.2 [184]. We observe that the energy levels of $MAPbI_3$ and $MAPbI_{3-x}Cl_x$ are almost identical. This is due to the fact that x is very small (up to 3 to 4%), because during perovskite formation most of chlorine leaves the film in form of

methyl-ammonium chloride (MACl)[185]. It is shown that the residual chlorine could help with the quality of carrier transfer across the heterojunction interfaces.

Also shown in Fig. 6.2 are the energy levels of TiO_2. TiO_2 is among the most frequently used contact materials in perovskite photovoltaics[186,187,188]. The conduction band of TiO_2 is almost perfect match to that of the n-type perovskites, and hence forms an ohmic contact and extracts the electrons from the device. Other materials that are used as ETL in perovskite cells include PCBM[189,190], CdS[191] and ZnO[192,193] .

A commonly used HTL for making junction with perovskites is Spiro-MeOTAD, whose energy levels are also shown in Fig. 6.2. Due to its high LUMO level, this molecule also blocks electrons, and thereby reduces recombination in the anode. Other HTLs in perovskite photovoltaics include PEDOT:PSS[189], P3HT[194], and NiO_x [190, 195,196].

The band structures of photovoltaic perovskites are shown in Fig.6.3. Studies have shown that these bandgaps are direct[197,198], which make them potentially attractive for Light Emitting Diode (LED) applications. In fact, such LEDs are already reported in the
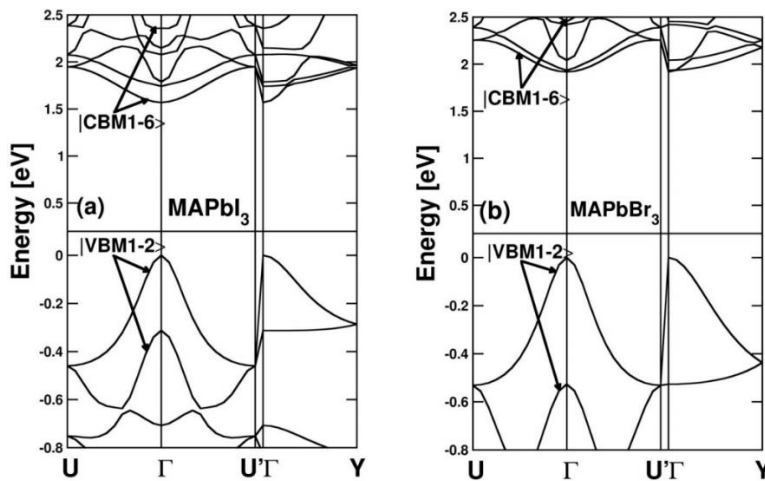
Fig. 6. 9. Band structure of MAPbI₃ and MAPbBr₃, calculated using Density Functional Theory (DFT)[197].
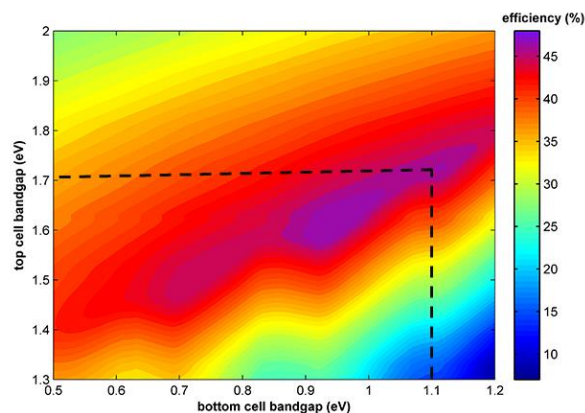
Fig. 6. 10. Perovskites (E_g=1.7 eV) when used in tandem with silicon (E_g=1.1 eV) are potential pathways to achieving high efficiencies.

literature: Tan et. al. have fabricated bright green and infrared (754 nm) LEDs made of $MAPbBr_3$ and $MAPbI_{3-x}Cl_x$, respectively. Moreover, they used Br and I mixture to tune the perovskite's bandgap and obtained red LED (630 nm)[199].

In addition to LEDs, the bandgap of organo-lead-halide perovskites makes them suitable for making tandem solar cells. Fig. 6.4 shows the theoretical efficiencies for an ideal double-junction tandem[200]. When perovskite is used in tandem with silicon (E_g=1.1 eV), these calculations forecast a tandem efficiency of >45%. In practice, however, the performance is reduced due to parasitic parameters such as absorption at the interlayers, and unwanted series and shunt resistances. These parasitic parameters are taken into account in recent simulations by Filipic et. al. Their results predict a silicon/perovskite tandem efficiency of ~30%[201].

6.3.   Fabrication of perovskite devices

One advantage of lead halide perovskites is that they can be synthesized using inexpensive raw materials. These ingredients usually include an organic compound and a lead salt. For synthesizing methyl ammonium lead iodide ($CH_3NH_3PbI_3$), the most
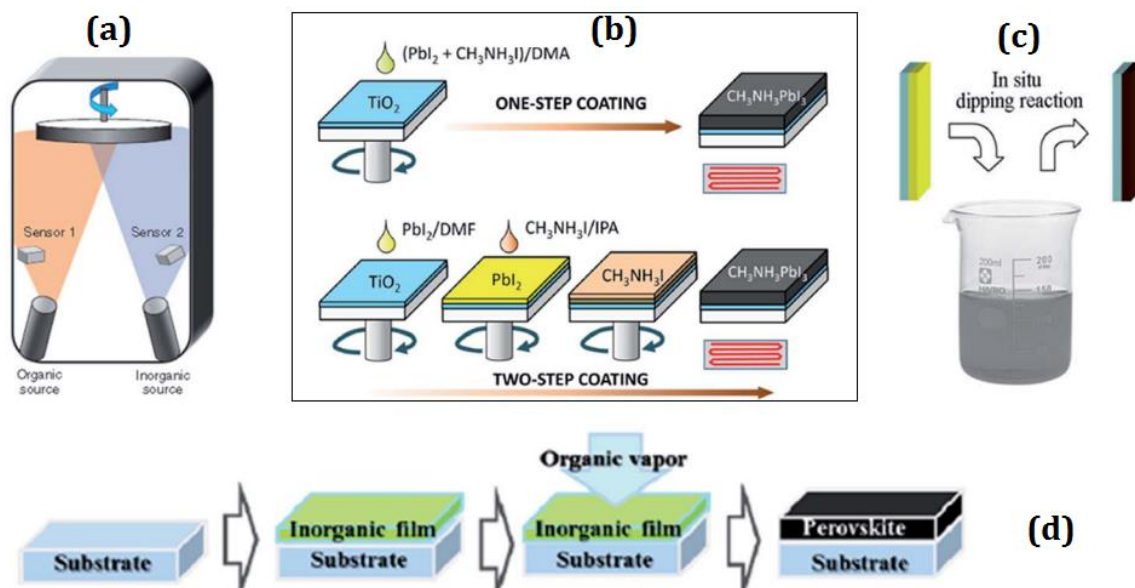
Fig. 6. 11. Methods for synthesizing perovskite thin films for solar cells: (a)Dual-source evaporation, (b) one-step (top) and two-step (bottom) spin-coating, (c) in-situ dipping, , and (d) vapor-assisted deposition.

frequently used organic compound is methyl ammonium iodide (MAI), and the lead salt is typically PbI_2 or $PbCl_2$. It is also shown that other salts such as $Pb(NO_3)_2$ or $Pb(SCN)_2$ can also be used to form $CH_3NH_3PbI_3$ [202].

Fig. 6.5 schematically shows perovskite synthesis methods[203]. One technique is dual-source evaporation, in which the organic compound and the salt (e.g. MAI and PbI_2) are co-evaporated simultaneously, and form perovskite on the substrate (Fig. 6.1(a)):

$$PbI_2 + CH_3NH_3I \rightarrow CH_3NH_3PbI_3 \tag{6.1}$$

Co-deposition of ingredients can also be done in liquid phase in a one-step spin-coating process (Fig. 6.5(b)-top). In this method, a liquid solution which contains both ingredients is spin-coated onto the substrate. The constituents react after deposition during a thermal annealing process, and form perovskite.
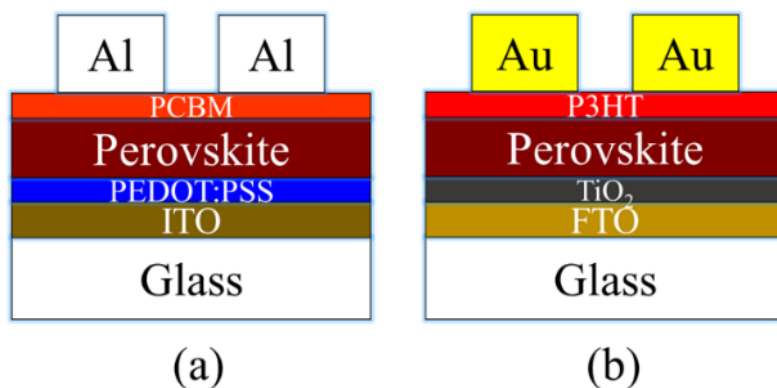
Fig. 6. 12. Device structures used in this study (a) p-i-n, (b) n-i-p.

Another way of depositing perovskite is to deposit the lead salt first, and then expose the substrate to MAI, which reacts with the salt and form perovskite. This can be done by dipping the lead salt film in a dilute solution of MAI (Fig. 6.5(c)), or by exposing the lead salt film to MAI vapors (Fig. 6.5(d)). An alternative way is to spin-coat a thin film of MAI on top of a solution-processed lead salt film using orthogonal solvents (Fig. 6.5 (b)-bottom). The reaction is then thermally activated by annealing the substrate on a hot plate, resulting in the formation of perovskite.

For our studies, we made both n-i-p and p-i-n methyl-ammonium lead iodide cells. The n-i-p devices were fabricated using vapor-assisted deposition (Fig. 6.5(d)), and the p-i-n cells were made using one step spin-coating (Fig. 6.5(b)-top). These device structures are shown in Fig. 6.6[204]. The remainder of this section is dedicated to describing our fabrication process in detail. After that, we move forward and report our results in device characteristics.

6.3.1. "p-i-n" solution-processed devices [204]

Fig. 6.6(a) shows the structure of our p-i-n cells. ITO-covered glass substrates were
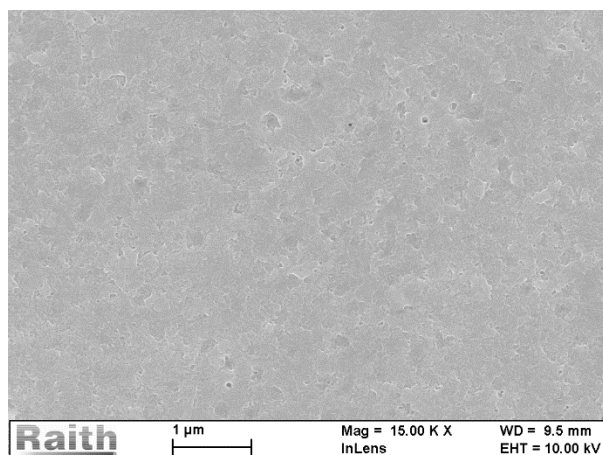
Fig. 6. 13. SEM micrograph of perovskite prepared by one-step spin-coating on PEDOT:PSS-coated ITO substrate. The film appears uniform and pinhole-free in micro-meter scale.

cleaned by boiling in acetone, followed by sonication in methanol for 20 minutes. Then the substrates were blow-dried with N_2, and cleaned in air plasma for 10 min. PEDOT:PSS was spin-coated at 4000 rpm for 40 sec on the clean ITO surface to form the HTL. Then the substrates were annealed in air for 20 min at 150C, and transferred into a Nitrogen-filled glove-box for deposition of the main layer.

A perovskite precursor was spin-coated on PEDOT:PSS at 4000 rpm for 60 sec, and annealed at 80C for 90 min on a hotplate until a dark brown perovskite layer is formed. Fig. 6.7 is the SEM micrograph of the film morphology, and shows that a uniform pinhole-free film is formed. Profilometry indicates that the final film thickness is ~150nm. The perovskite precursor was made by dissolving 212 mg of methyl-ammonium iodide (MAI) and 122 mg of lead chloride ($PbCl_2$) in 1 ml Dimethylformamide (DMF). The solution was stirred overnight at room temperature before use.

After the formation of perovskite the ETL was formed by spinning $PCBM_{60}$ at a rate of 2000 rpm, and then drying the device at 50C for 20 min. The cells were then finished by depositing 100 nm of aluminum through circular shadow masks (0.106 cm^2) in thermal
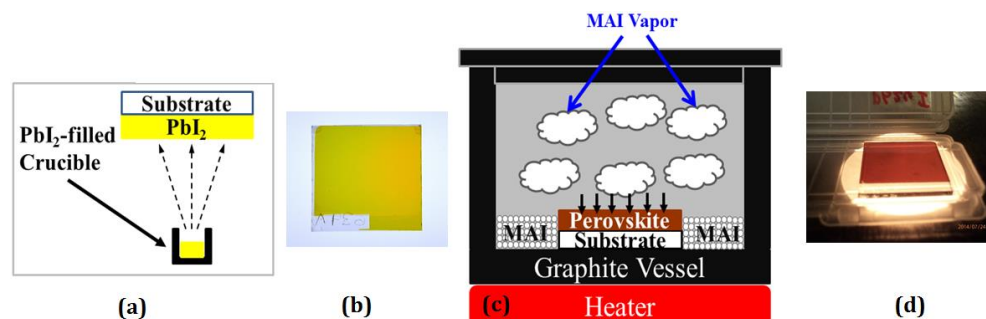
Fig. 6. 14. Vapor-assisted perovskite growth: (a) Thermal evaporation of PbI₂ resulting in (b) a transparent yellow film, (c) exposure of the PbI₂ film to MAI vapors in an enclosed heated graphite vessel leads to the formation of (d) dark brown methyl-ammonium lead iodide.

evaporator. The aluminum contacts were 0.106 cm². Fig. 6.6(a) schematically shows the structure of these p-i-n cells.

6.3.2 "n-i-p" sequential-vapor phase deposition[205]

The structure of n-i-p cell is depicted in Fig. 6.6(b). FTO-coated glass substrates were cleaned by boiling in acetone, followed by sonication in methanol for 20 minutes. TiO_2 ETL was deposited on FTO by spin-coating titanium di-isopropoxide acetylacetonate solution (0.3 M in 1-butanol). The substrate was dried at 125C for 10 min, and then sintered at 550C for 15 min. A thin layer of TiO_2 was subsequently deposited using chemical bath by submerging the substrate in 50 mM solution of Ti-tetrachloride in DI water at 75C for 30 minutes. Afterwards, the sample was washed in DI water and isopropanol, and sintered at 550C for 30 minutes to complete the ETL.

The perovskite layer was grown on top of TiO_2 using a sequential growth method, schematically depicted in Fig. 6.8[205]. First ~200 nm of PbI₂ is deposited by thermal evaporation at a rate of ~1 A/sec. Then the PbI₂ film is exposed to MAI vapor in an enclosed heated petri-dish or a graphite vessel. As a result of the gas-solid reaction, the yellow PbI₂ film converts to dark brown $CH_3NH_3PbI_3$ (Fig. 6.8(d)). The final thickness of the
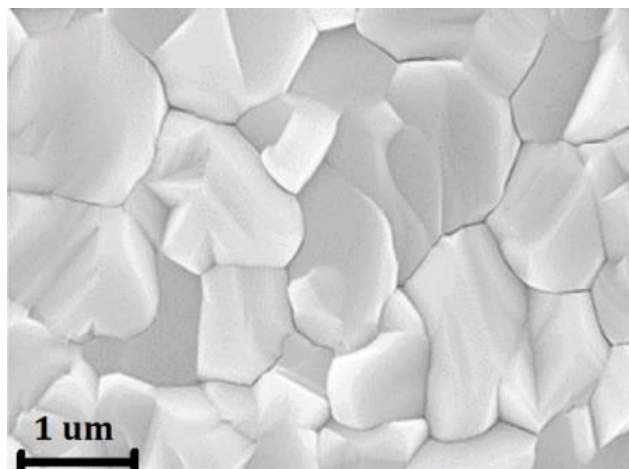
Fig. 6. 15. SEM micrograph of perovskite film deposited by vapor-assisted growth on top of TiO₂-coated FTO substrate. A compact arrangement of large grains is observed.
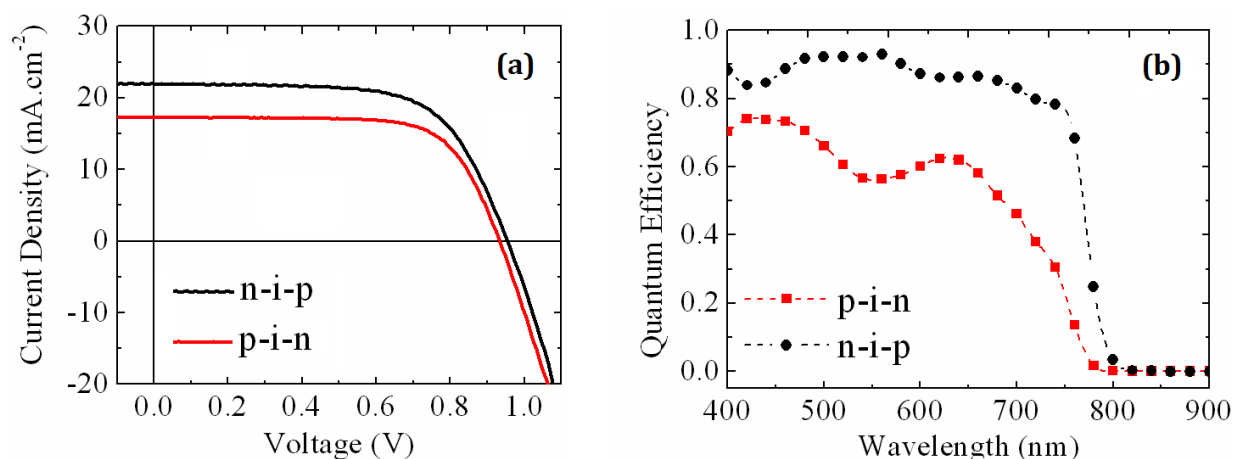
Fig. 6. 16. IV characteristics (a), and QE spectra (b) of n-i-p (black) and p-i-n (red) CH₃NH₃PbI₃ solar cells.

perovskite layer is ~500 nm from profilometry measurements. SEM micrograph of the film (Fig. 6.9) indicates the formation of large grains.

The HTL was deposited by spin-coating a 12 mg/ml solution of P3HT in chlorobenzene at 4000 rpm. The device was then finished by depositing 80nm thick gold contacts by thermal evaporation.

6.4. Results and discussion

The IV and QE of devices are plotted in Fig. 6.10. The power conversion efficiencies
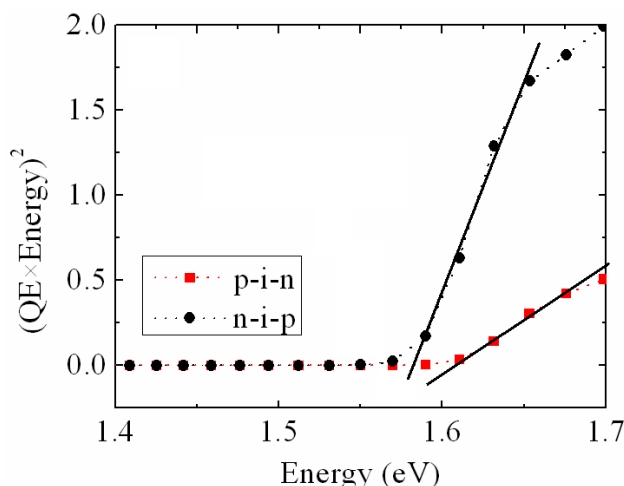
Fig. 6. 17. Perovskite bandgaps in n-i-p and p-i-n cells of Fig. 6.10 are ~1.57 eV.

are 11% and 14% for p-i-n and n-i-p cells, respectively. The lower short-circuit current in the p-i-n cell is due to reduced absorption in its comparably thinner perovskite layer, which manifests itself as a drop in QE at long wavelengths (>650 nm). In order to measure the optical bandgaps, we plotted $(QE \times Energy)^2$ vs. energy for each cell (Fig. 6.11). The bandgaps for our samples are ~1.57 eV, which is in agreement with the values obtained from Tauc plots reported elsewhere[206] in the literature.

Next, we measure subgap QE (Fig. 6.12(a)). It shows the presence of band tails with an Urbach energy of ~ 16 meV for both the n-i-p and p-i-n devices. Farther from the band edge (E<1.5 eV), we observe a heavy distribution of deep defects which extend towards a midgap region. We used capacitance spectroscopy to evaluate the density of deep defects (DOS) for both devices. The results are shown in Fig. 6.12(b). Both the n-i-p and p-i-n devices show identical density of defects with a major peak at ~0.62 eV. Moreover, upon closer examination, we observe that this peak obeys a Gaussian distribution (inset). These result show that our vapor-grown and solution-processed perovskites are very similar in
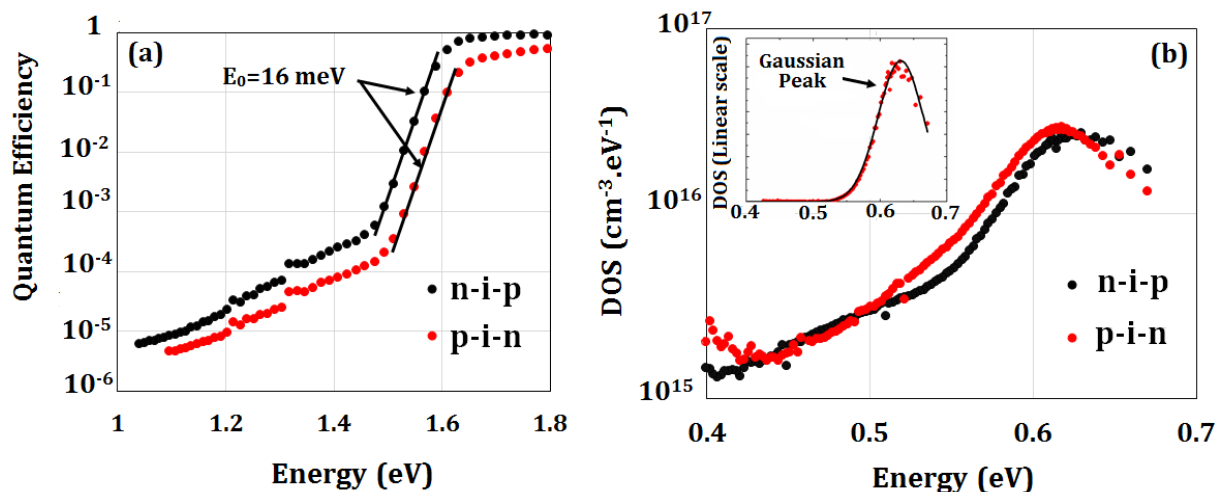
Fig. 6. 18. Similar distribution of electronic states in n-i-p and p-i-n cells: (a) subgap QE shows identical Urbach energy of tail states (16 meV) for both cells, and (b) CF indicates a Gaussian peak in DOS at ~0.62 eV. The solid line in the inset is a Gaussian fit to the DOS data of n-i-p cell.
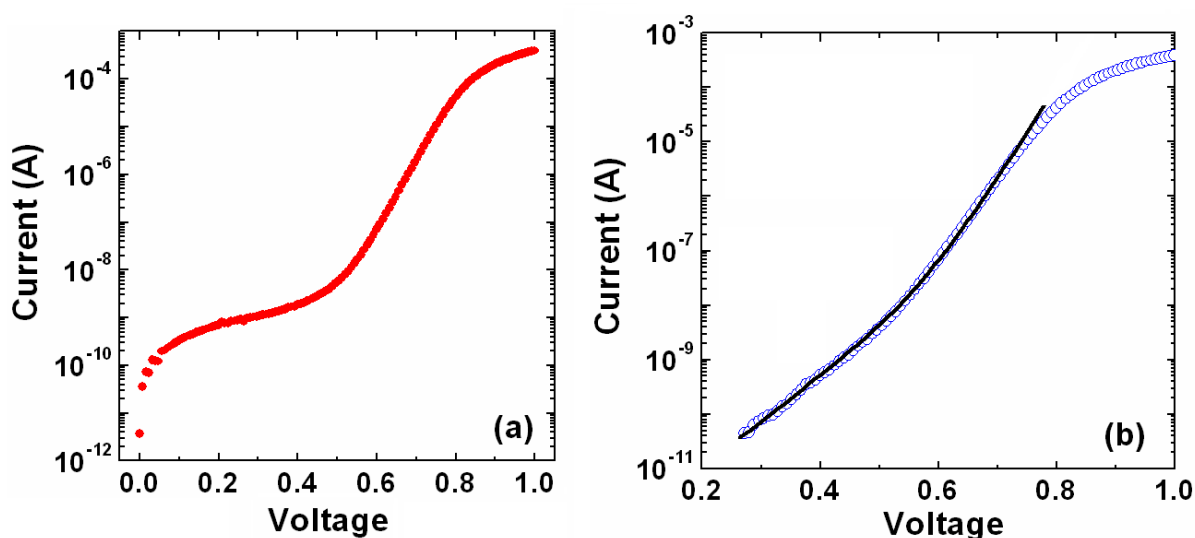
Fig. 6. 19. Dark IV of the p-i-n cell (a) before, and (b) after subtracting shunt current. Solid line in (b) is the fit of double diode model to the data points (open circles) for $n_1=2$, $I_{01}=2.2 \times 10^{-13}A$, $n_2=1$, and $I_{02}=3.1 \times 10^{-18}A$.

terms of electronic properties such as band-gap, Urbach tails, and defect density.

The dark IV of the p-i-n device is shown in Fig. 6.13. After subtracting the shunt current (Fig. 6.13(b)), a two diode model fits the data over six orders of magnitude (solid line) before the effect of series resistance come into play at voltages greater than ~0.8V. At low biases, the ideality factor is 2, showing the significance of SRH recombination at low injection levels. As the carrier injection increases, the rate of band-to-band recombination
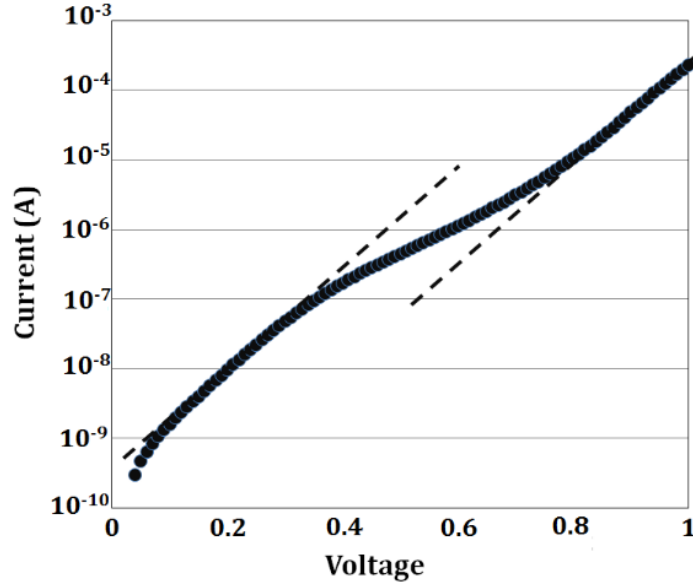
Fig. 6. 20. Dark IV of the n-i-p cell shows single slope. I_0 decreasing from 4×10^{-10} A to 3×10^{-11} A at higher biases.

goes up as a quadratic function of carrier concentration ($\propto n^2$), until it dominates recombination, and results in an ideality factor of 1. A theoretical value for V_{OC} can be obtained using the equivalent circuit of Fig. 2.2 assuming $n_2 \sim 1$, $I_L = 1.7$ mA, $I_{02} \sim 10^{-18}$A:

$$V_{OC} = \frac{kT}{q} Ln\left(\frac{I_L}{I_0}\right) \sim 0.91 \, V \tag{6.2}$$

Which is in fair agreement with the measured value of ~ 0.94V (Fig. 6.10(a)).

Notice that the narrow distribution of Urbach tails ($E_0 \sim 16$ meV) demands an ideality factor of 0.76 (Eq. 4.6) for tail state recombination in these cells. The measured ideality factors, therefore, strongly suggest that band tail recombination has negligible effect on carrier lifetimes in our devices.

Fig. 6.14 shows the dark IV of an n-i-p cell. The curve shows a single slope with a shift of roughly one order of magnitude in saturation current (I_0) at high voltage. This can be attributed to the voltage dependence of surface recombination velocity at one of the contacts[207]. Since thiophenes are suggested to have a passivating effect on perovskite
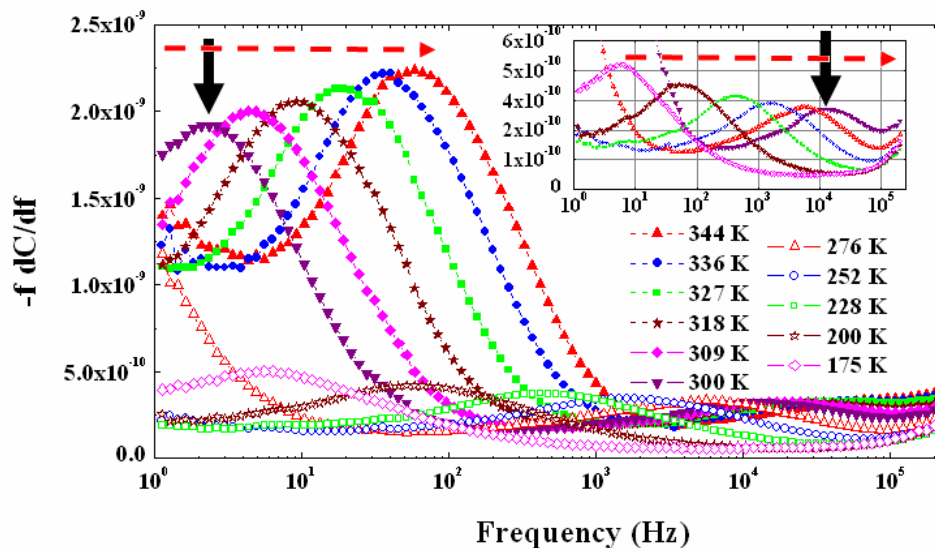
Fig. 6. 21. fxdC/df vs. frequency data at different temperatures. The inset magnifies the peak due to shallow defect band. Solid arrows are the peaks at room temperature. Dashed arrows indicate the direction at which the peaks shift as temperature increases.

surface states[208], an educated guess is that this surface recombination is probably at the TiO_2 interface as opposed to the P3HT/Perovskite interface. Nevertheless, the dark IV is obscured (likely) by surface recombination phenomena, and does not reflect the bias-dependence of bulk recombination.

In order to obtain more information about electronic defect states in perovskite cells, we performed CFT measurements on n-i-p devices. Fig. 6.15 is (-f×dC/df) vs. frequency spectra measured between 175 K and 344 K[204]. At room temperature, two peaks are observed (solid arrows). These peaks occur at ~2 Hz and ~10^4 Hz, and correspond to a deep and a shallow defect level, respectively. As the temperature increases, traps are more activated, and the peaks shift towards higher frequencies (dashed arrows). By tracking the peak frequencies, and plotting them in the Arrhenius diagram described in section 2.8, we obtain the activation energy related to each defect band. The lower frequency peaks shows an activation energy of 0.66 eV (Fig. 6.16(b)), which supports our earlier observation of a
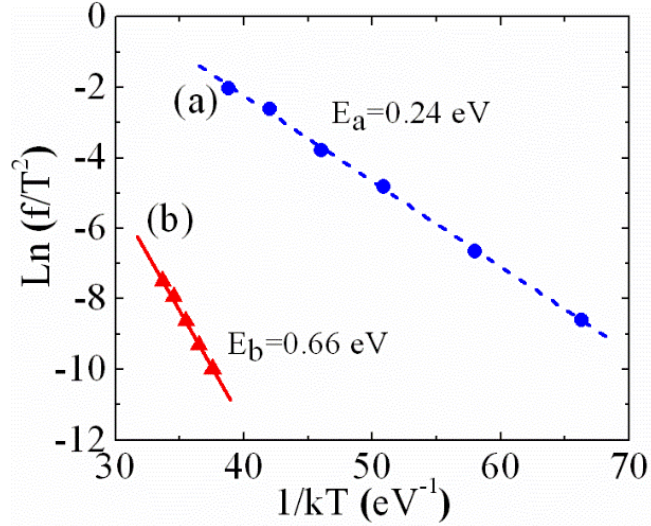
Fig. 6. 22. Two defect bands are obtained from the Arrhenius diagram: (a) 0.24 eV, and (b) 0.66 eV below the conduction band edge.

defect peak at that depth in the CF measurements (Fig. 6.12(b)). The activation energy of the higher frequency peak, on the other hand, indicates that a shallow defect band is located ~0.24 eV below the band edge. This is in fair agreement with observation by Duan et. al[209]. Moreover, we determine the attempt-to-escape-frequency to be ~2×10^{11} Hz at room temperature.

6.5. Conclusion

We report on the fundamental electronic properties of $CH_3NH_3PbI_3$ perovskite solar cells. The Urbach energy of methyl-ammonium lead iodide cells is determined by subgap QE, and is 16 meV. This narrow distribution of tail states eliminates the role of tail state recombination in the device. Instead, dark current ideality factors indicate that SRH and band-to-band recombination are dominant at, respectively, low and high biases. Moreover, the photo-voltage correlates well with the ideality factor and dark saturation current at high biases, indicating that band-to-band recombination is dominant at high excitations levels, and limits the photo-voltage.

A major band of defects is detected at ~0.62-0.66 eV below the conduction band edge of methyl-ammonium lead iodide perovskite. The band has a Gaussian distribution, and the peak defect density is obtained to be in the range of 10^{16}s $cm^{-3}.eV^{-1}$. We also detected a shallower defect band at ~0.24 eV away from the band-edge. The related attempt-to-escape-frequency is in the range of 10^{11} Hz.

CHAPTER VII

CONCLUSIONS

In summary, I have explored the fundamental electronic and optical properties of several new organic and hybrid photovoltaic materials. These properties are directly relevant to the performance and stability of solar cells made in these material systems. In the paragraphs below, I outline the major results of my research.

• We discovered how the various sub-gap optical absorption measurements were related to specific defect densities in organic materials such as PTB7. This is an important measurement, because it allowed us to deduce that there were subgap states at the donor-acceptor interface which controlled recombination and therefore fill factor in solar cells made from PTB7. Prior to this work, it was not clear how the various optical transitions corresponded to deep bulk and interfacial defects.

• We developed a new device structure using an inorganic electron transport layer in organic solar cells which then led to significantly lower degradation under light compared to the case when an organic layer was used as the electron transport layer.

• We developed a new model for recombination in organic solar cells, which matched almost perfectly the experimental data for dark I-V curves as well as the data for open circuit voltage vs. intensity of light. The model predicted the open-circuit voltage that one could obtain in such cells, and matched the experimental data very well. The model showed that under light, the dominating recombination was controlled by band tail states in the donor, and not by band-to-band recombination. This is a new model which is much more accurate in predicting the performance of the solar cells than previously existing models.

- We did the first experiments in the world to deduce deep and shallow defects in a new class of photovoltaic materials, Pb-halide perovskites. Knowledge of such defects is critical for understanding how the PV devices work in this new class of materials.

- We developed tandem cells employing an inorganic semiconductor (a-Si) and an organic one (PTB7) which improved the performance of organic cells.

REFERENCES

[1] J. Tsao, N. Lewis, and G. Crabtree, "Solar FAQs", Sandia National Laboratory, 2006. *Available at: http://www.sandia.gov/~jytsao/Solar%20FAQs.pdf*

[2] "Key World Energy Statistics", International Energy Agency (IEA), 2014. *Available at: http://www.iea.org/publications/freepublications/publication/keyworld2014.pdf*

[3] *https://en.wikipedia.org/wiki/World_energy_consumption*

[4] *http://www.firstsolar.com/en/About-Us/Corporate-Responsibility/Environmental-Impact.aspx*

[5] *https://en.wikipedia.org/wiki/Price_per_watt#/media/File:Price_history_of_silicon_PV_cells_since_1977.svg*

[6] *http://www1.eere.energy.gov/tribalenergy/guide/costs_solar_photovoltaics.html*

[7] *http://www.statista.com/statistics/280220/global-cumulative-installed-solar-pv-capacity/*

[8] Adopted with modifications from: *https://conservativecritic.wordpress.com/2012/02/22/is-solar-energy-cost-effective/*

[9] *http://www.renewableenergyfocus.com/view/19395/sunshot-solar-pvs-falling-costs/*

[10] "Sunshot Vision Study" U.S. Department of Energy, February 2012. Available at: *http://www1.eere.energy.gov/solar/pdfs/47927_executive_summary.pdf*

[11] " $1/W Photovoltaic Systems, White paper to explore, A Grand Challenge for Electricity from Solar", Advanced Research Projects Agency, US Department of Energy. Available at: *http://www1.eere.energy.gov/solar/sunshot/pdfs/dpw_white_paper.pdf*

[12] NREL Efficiency Chart, July 2015. Available at: *http://www.nrel.gov/ncpv/*

[13] Ben G. Streetman, "Solid State Electronic Devices", page 97, Fourth Edition, Prentice Hall, 1995.

[14] A. Shah, "Thin Film Silicon Solar Cells", EPFL Press, 2010, Pages 43-44.

[15] J. Pankove, "Optical Processes in Semiconductors", Dover Publications, 1971, page 43.

[16] W. B. Jackson et. al., "Direct measurement of gap state absorption in hydrogenated amorphous silicon by photo-thermal deflection spectroscopy", Physical Review B, Vol. 25, No. 8, 1982.

[17] L. Luciani et. al., "Sub-gap absorption study of defects in ion-implanted and annealed Si layers", Applied Physics A, 50, 495-498, 1990.

[18] N. Wyrsch et. al., "How to reach more precise interpretation of subgap absorption spectra in terms of deep defect density in a-Si:H", Journal of Non-Crystalline Solids, 137 & 138 (1991) 347-350.

[19] Ben G. Streetman, "Solid State Electronic Devices", Fourth Edition, Prentice Hall, 1995, page 98.

[20] Ben G. Streetman, "Solid State Electronic Devices", Fourth Edition, Prentice Hall, 1995, page 103-106.

[21] D. Neaman, and D. Biswas, "Semiconductor physics and devices", Special Indian Edition, McGraw Hill, page 149-152.

[22] R. Pierret, "Advanced Semiconductor Fundamentals", Second Edition, Prentice Hall, 2003, pages 141-151.

[23] Gerhard Klimeck, "ECE606: Solid State Device Physics", Lecture 9, Purdue University, Fall 2012, Available at: *http://ee.sharif.edu/~sarvari/25798/purdue.edu-ECE606_f12_Lecture9 .pdf*

[24] R. Pierret, "Advanced Semiconductor Fundamentals", Second Edition, Prentice Hall, 2003, pages 135-137.

[25] R. Pierret, "Advanced Semiconductor Fundamentals", Second Edition, Prentice Hall, 2003, pages 165.

[26] V. Prajapati, "Advanced front-side technologies in crystalline silicon solar cells", PhD dissertation, Katholieke Universiteit Leuven, March 2013, page 95.

[27] A. McEvoy et. al.,"Solar cells: Materials, manufacture and operation", second edition, Elsevier, 2013, ISBN: 978-0-12-386964-7, page 45.

[28] http://www.pveducation.org/pvcdrom/characterisation/bulk-lifetime

[29] J. Pankove, "Optical Processes in Semiconductors", Dover Publications, 1971, page 114-124.

[30] A. M. Fox, "Optical properties of solids", Oxford University Press 2001, page 78.

[31] R. Hall, "Properties of Crystalline Silicon", Published by: INSPEC, 1999, ISBN 0852969333, page 392.

[32] M. Green, "Improved value for the silicon free exciton binding energy", AIP advances 3, 112104 (2013).

[33] S.-S. Sun, "Basic electronic structures and charge carrier generation in organic optoelectronic materials", Introduction to organic electronic and optoelectronic materials and devices, Chapter 3, page 73.

[34] M. Muntwiler, "Exciton formation and decay at surfaces and interfaces", Dynamic at solid state surfaces and interfaces: Volume 1- Current developments, Wiley-VCH Verlag & Co. KGaA, 2010, ISBN: 978-3-527-40937-2.

[35] M. Knupfer, "Exciton binding energies in organic semiconductors", Applied Physics A, 77, 623-626 (2003).

[36] V. Arkhipov et. al., "Exciton dissociation and charge photogeneration in pristine and doped conjugated polymers", Physica Status Solidi (a) 201, No. 6 (2004).

[37] M. Muntwiler et. al., "Coulomb barrier for charge separation at an organic semiconductor interface", Physical Review Letters 101, 196403 (2008).

[38] D. Neaman, and D. Biswas, "Semiconductor physics and devices", Special Indian Edition, McGraw Hill, page 155-169.

[39] J. E. Allen, "Investigation of carrier transport in semiconductor nanowires by scanning probe techniques", PhD dissertation, Northwestern University, December 2008, pages 75-79.

[40] A. McEvoy et. al.,"Solar cells: Materials, manufacture and operation", second edition, Elsevier, 2013, ISBN: 978-0-12-386964-7, page 183.

[41] X. Wang, et. al., "High efficiency solar cells: physics, materials and devices", Springer, 2014, ISBN: 978-3-319-01987-1, page 187.

[42] A. Shyam, "Fabrication of high quality, low bandgap amorphous Silicon and amorphous Silicon Germanium alloy solar cell by Chemical Annealing", PhD Dissertation, Iowa State University, 2011, page 9.

[43] L. G. Gerling et. al., "Straight forward determination of the effective mobility-lifetime product of small molecules organic solar cells", proceedings of IEEE 10th Spanish conference on Electron Devices (CED), DOI: 10.1109/CDE.2015.7087503

[44] T. Kirchartz et. al., "Understanding the thickness-dependent performance of organic bulk heterojunction solar cells: influence of mobility, lifetime and space charge", Journal of Physical Chemistry Letters, 2012, 3, 3470-3475.

[45] *Adopted with modifications from:* A. Shyam, "Fabrication of high quality, low bandgap amorphous Silicon and amorphous Silicon Germanium alloy solar cell by Chemical Annealing", PhD Dissertation, Iowa State University, 2011, page 22.

[46] Adopted with modifications from: https://en.wikipedia.org/wiki/Shockley%E2%80%93Queisser_limit

[47] W. Shockley et. al., "Detailed balance limit of efficiency of p-n junction solar cells", Journal of Applied Physics 32, 510 (1961)

[48] T. Kirchartz et. al., "Efficiency limits of organic bulk heterojunction solar cells", Journal of Physical Chemistry C, 2009, 113, 17958-17966.

[49] PV Performance Modeling Collaborative (PVPMC), Sandia National Laboratories, Available at: https://pvpmc.sandia.gov/modeling-steps/2-dc-module-iv/diode-equivalent-circuit-models/

[50] Adopted with modifications from: http://www.pveducation.org/pvcdrom/characterisation/double-diode-model

[51] H. Borchert, "Solar cells based on colloidal nanocrystals", Springer series in materials science, ISBN: 978-3-319-04387-6, 2014, page 140.

[52] I. F. Perepichka et. al., "Handbook of thiophene-based materials", John Wiley & Sons Inc., 2009, page 149.

[53] K.A. Emery, "Solar simulators and I-V measurement methods", Solar Cells 18 (1986) 251-260.

[54] M. Samiee et. al., "Measurements of defect densities and Urbach energies of tail states in PTB7 solar cells", Applied Physics Letters, 105, 133511 (2014)

[55] D. Neaman, and D. Biswas, "Semiconductor physics and devices", Special Indian Edition, McGraw Hill, page 225-230.

[56] Ben G. Streetman et. al., "Solid State Electronic Devices", Sixth Edition, Prentice Hall, 2009, page 221.

[57] http://www.pveducation.org/pvcdrom/solar-cell-operation/ideality-factor

[58] T. Kirchartz et. al., "Recombination via tail states in polythiophene:fullerene solar cells", Physical Review B 83, 115209 (2011).

[59] Ben G. Streetman et. al., "Solid State Electronic Devices", Sixth Edition, Prentice Hall, 2009, page 225.

[60] G. P. Smestad, "Optoelectronics of solar cells", SPIE Press, 2002, ISBN: 0-8194-4440-5, page 41.

[61] R. Brendel, "Thin film crystalline silicon solar cells: physics and technology", Wiley-VCH, 2003, ISBN:3-527-40376-0, page 53.

[62] A. L. Fahrenbruch et. al., "Fundamentals of solar cells", Academic Press, 1983, ISBN: 0-12-247680-8, page 81.

[63] http://www.pveducation.org/pvcdrom/solar-cell-operation/quantum-efficiency

[64] A. Shyam, "Fabrication of high quality, low bandgap amorphous Silicon and amorphous Silicon Germanium alloy solar cell by Chemical Annealing", PhD Dissertation, Iowa State University, 2011, page 5.

[65] Adopted with modifications from: A. Shyam, "Fabrication of high quality, low bandgap amorphous Silicon and amorphous Silicon Germanium alloy solar cell by Chemical Annealing", PhD Dissertation, Iowa State University, 2011, page 62.

[66] A. Shah, "Thin Film Silicon Solar Cells", EPFL Press, 2010, Pages 42.

[67] J. Pankove, "Optical Processes in Semiconductors", Dover Publications, 1971, page 34-40.

[68] E. A. Davis et. al., "Conduction in non-crystalline systems V. Conductivity, optical absorption and photoconductivity in amorphous semiconductors", Philosophical magazine, Vol. 22, Issue 179, 1970, pp. 903-922.

[69] X. Deng et. al., "Amorphous silicon-based solar cells", Handbook of Photovoltaic Science and Engineering, 2003 John Wiley & Sons Ltd., ISBN:0-471-49196-9., page 517.

[70] i.b.i.d., page 519.

[71] S. John et. al., "Theory of electron band tails and the Urbach optical absorption edge", Vol. 57, No. 14, 1986, pp. 1777-1780.

[72] F. Urbach, "The long wavelength-edge of photo-graphic sensitivity and of the electronic absorption of solids", Physical Review, 92, 1324, December 1953.

[73] V. Dalal et. al., "Device physics of nano-crystalline silicon solar cells", 34th IEEE Photovoltaic Specialists Conference (PVSC), 2009, pages 1667-1671.

[74] A. Shyam, "Fabrication of high quality, low bandgap amorphous Silicon and amorphous Silicon Germanium alloy solar cell by Chemical Annealing", PhD Dissertation, Iowa State University, 2011, page 36.

[75] R. A. Street, "Recombination through different types of localized states in organic solar cells", Adv. Funct. Mater. 2012, 22, 4608–4619.

[76] D. K. Schroder, "Semiconductor material and device characterization", Third edition, IEEE Press, John Wiley and Sons, 2006, page 261.

[77] R. Pierret, "Advanced Semiconductor Fundamentals", Second Edition, Prentice Hall, 2003, pages 145.

[78] R. Street, "Hydrogenated amorphous silicon", Cambridge University Press, 2005, page 118.

[79] I. D. French et. al., "Microcrystalline silicon TFTs for AMCLDs", Proceedings of Thin Film Transistor Technology V, The Electrochemical Society, 2001, page 50.

[80] Adopted with modifications from: Shantan Kajjam, "Influence of oxygen on electronic properties of nanocrystalline silicon", PhD thesis, Iowa State University, 2013, page 44.

[81] J. A. Carr et. al., "On the identification of deeper defect levels in organic photovoltaic devices", J. Appl. Phys. 114, 064509 (2013)

[82] 19. P. Boix et. al., "Determination of gap states in organic bulk heterojunction solar cells from capacitance measurements", Appl. Phys. Lett., 95, 233302 (2009).

[83] T. Walter et. al., "Determination of defect distributions from admittance measurements and application to Cu(In,Ga)Se2 based heterojunctions", Journal of Applied Physics 80, 4411 (1996).

[84] Shantan Kajjam, "Influence of oxygen on electronic properties of nanocrystalline silicon", PhD thesis, Iowa State University, 2013, pages 51-52.

[85] D. Congreve, "Calculation of defect densities in nano-crystalline and amorphous silicon devices using differential capacitance measurements", M.S. Theis, Iowa State University, 2011, page 30.

[86] D. Neaman, and D. Biswas, "Semiconductor physics and devices", Special Indian Edition, McGraw Hill, page 192.

[87] J. S. Yuan et. al., "Semiconductor device physics and simulation", Springer Science + Business Media New York, 1998, ISBN: 978-1-4899-1906-9.

[88] Ben G. Streetman, "Solid State Electronic Devices", Fourth Edition, Prentice Hall, 1995, pages 173-176.

[89] Vikram Dalal's group database, Microelectronic Research Center, Iowa State University, Sample #: 2-17871A3.

[90] V. Dalal et. al., "Defect density and diffusion length of holes in nanocrystalline silicon devices", Applied Physics Letters, 86:103510, (2005)

[91] L. C. Kimerling, "Influence of deep traps on the measurement of free carrier distributions in semiconductors by junction capacitance techniques", Journal of Applied Physics, Vol. 45, No. 4, April 1974.

[92] D. Basu, "Charge transport in polymer semiconductors", PhD Dissertation, University of Texas at Austin, 2007, page 33.

[93] W. Leigh, "Devices for optoelectronics", Marcel Dekker Inc., 1996, page 60.

[94] D. Neaman, and D. Biswas, "Semiconductor physics and devices", Special Indian Edition, McGraw Hill, page 80.

[95] R. Pierret, "Advanced Semiconductor Fundamentals", Second Edition, Prentice Hall, 2003, pages 112.

[96] R. Pierret, "Advanced Semiconductor Fundamentals", Second Edition, Prentice Hall, 2003, pages 152.

[97] J. A. Carr, "The identification and characterization of electronic defect bands in organic photovoltaic devices", PhD Dissertation, Iowa State University, page 110, 2014.

[98] Taken from Sigma-Aldrich catalogue. Available at: https://www.sigmaaldrich.com/catalog/AdvancedSearchPage.do

[99] S. H. Park et. al., "Bulk heterojunction solar cells with internal quantum efficiency approaching 100%", Nature Photonics 3, 297-302 (2009).

[100] U. Zhokhavets et. al., "Relation between absorption and crystallinity of poly(3-hexylthiophene)/fullerene films for plastic solar cells", Chemical Physics Letters 418 (2006) 347-350.

[101] Y. Lin et. al., "High-performance fullerene-free polymer solar cells with 6.31% efficiency", Energy and environmental science, 2015, 8, 610.

[102] T. Aernouts et. al., "Processing and production of large modules", Polymer Photovoltaics: A practical approach, Chapter 5. Pages 229-300, SPIE Press, 2008. ISBN: 978-0-8194-6781-2.

[103] C. Teng, "Two layer organic photovoltaic cell", Applied Physics Letters 48, 1986.

[104] C.-C. Chen, "An efficient triple-junction polymer solar cell having a power conversion efficiency exceeding 11%", Advanced Materials, 2014, 26, 5670-5677.

[105] C.-F. Lin et. al., "High photo-electric conversion efficiency of metal Phthalocyanine/fullerene heterojunction photovoltaic device", International Journal of Molecular Sciences, 2011, 12(1), 476-505.

[106] T. Wang et. al., "Correlating molecular morphology with optoelectronic function in solar cells based on low bandgap copolymer: fullerene blends", Journal of Materials Chemistry C, 2013, 1, 7266.

[107] *See for example:* S. Forrest, "The limits to organic photovoltaic cell efficiency", MRS Bulletin, Volume 30, Issue 1, January 2005, pp. 28-32.

[108] Y. Yao, "Nanomorphology control and novel materials studies in polymer/fullerene bulk heterojunction solar cells", PhD dissertation, University of California Los Angeles, 2008, page 10.

[109] S. R. Scully et. al., "Physics and material issues of organic photovoltaics", Flexible Electronics: Materials and applications", Springer Science + Business Media, 2009, pages 344-347.

[110] W. Beek et. al., "Hybrid polymer-Inorganic photovoltaic cells", Hybrid Nanocomposites for Nanotechnology: Electronic, Optical, Magnetic and Biomedical applications, Springer Science + Business media, 2009, page 324.

[111] G. Yu et. al., "Polmer photovoltaic cells: Enhanced efficiencies via a network of internal donor-acceptor heterojunctions", Science 270 (1995) 1789-1791.

[112]   http://www-ssrl.slac.stanford.edu/content/science/highlight/2011-01-31/effects-thermal-annealing-morphology-polymer%E2%80%93fullerene-blends-organic

[113] W. Tress, "Organic solar cells: Theory, experiment and device simulation", Springer series in materials science 208, 2014, page 236.

[114] H. Ohkita et. al., "Exciton and charge dynamics in polymer solar cells studied by transient absorption spectroscopy", Organic solar cells: Materials and device physics, Springer, ISBN: 978-1-4473-4822-7.

[115] R. Street et. al., "Experimental test for geminate recombination applied to organic solar cells", Physical Review B 82, 121301 (R), 2010.

[116] K. Steirer et. al., "Enhanced efficiency in plastic solar cells via energy matched solution processed NiO_X interlayer", Advanced Energy Materials, 2011, 1, 813-820.

[117] E. Ratcliff et. al., "Energy level alignment in $PCDTBT:PC_{70}BM$ solar cells: Solution processed NiO_X for improved hole collection and efficiency", 13 (2012) 744-749.

[118] C. Waldauf et. al., "Highly efficient inverted organic photovoltaics using solution based titanium oxide as electron selective contact", Applied Physics Letters 89, 233517 (2006).

[119] E. Itoh et. al., "Photovoltaic properties of Bulk-heterojunction organic solar cell with ultrathin titanium oxide nanosheet as electron selective layer", Japanese Journal of Applied Physics 52 (2013) 04CK05

[120] Y. Liang et. al., "For the bright future- Bulk heterojunction polymer solar cells with power conversion efficiency off 7.4%", Adv. Mater. 2010, 22, E135-E138.

[121] Z. He et. al., "Enhanced power conversion efficiency in polymer solar cells using an inverted device structure", Nature Photonics, Vol. 6, 591-595, September 2012.

[122] S. Ochiai, et al., Characteristics and the effect of additives on the nanomorphology of PTB7/PC71BM composite films, Current Applied Physics (2013), http://dx.doi.org/10.1016/j.cap.2013.01.010

[123] J. Guo et. al., "Structure, dynamics and power conversion efficiency correlations in a new low bandgap polymer:PCBM solar cell", J. Phys. Chem. B 2010, 114, 742-748.

[124] M. R. Hammond et. al., "Molecular order in high efficiency polymer fullerene bulk heterojunction solar cells", ACS Nano, Vol. 5, No. 10, 8248-8257, 2011.

[125] B. Collins et. al., "Absolute measurement of domain composition and nanoscale size distribution explains performance in PTB7:PCBM71 solar cells", Adv. Energy Mater., 2013, 3, 65-74.

[126] S. Lou et. al., "Effects of additives on the morphology of solution phase aggregates formed by active layer components of high efficiency organic solar cells", J. Am. Chem. Soc., 2011, 133, 20661-20663.

[127] A. Foertig et. al., "Nongeminate and geminate recombination in PTB7:PCBM solar cells", Adv. Funct. Mater., 2013, DOI: 10.1002/adfm.201302134.

[128] T. Agostinelli et. al., "Real-time investigation of crystallization and phase segregation dynamics in P3HT:PCBM solar cells during thermal annealing", Advanced Functional Materials, 2011, 21, 1701-1708.

[129] C-W Chu et. al., "Control of nano-scale crystallinity and phase separation in polymer solar cells", Applied Physics Letters 92, 103306 (2008).

[130] J. Rivenay et. al., "Structural origin of gap states in semicrystalline polymers and the implications for charge transport", Phys. Rev. B. 83, 121306(R), 2011.

[131] R. Street, "Hydrogenated Amorphous Silicon", Cambridge University Press, 2005.

[132] J. Simmons and G. Taylor, "Nonequilibrium steady state statistics and associated effects for insulators and semiconductors containing an arbitrary distribution of traps", Phys. Rev. B., Vol. 4, No. 2, 1971.

[133] B. G. Streetman and S. K. Banerjee, "Solid state electronic devices", sixth edition, Prentice Hall, pp. 90.

[134] K. Seki et. al., "Influence of Energetic disorder on the Open circuit voltage in organic bulkheterojunction composites", Jpn. J. Appl. Phys., August 2013.

[135] J. Blakesly et. al., "Relationship between energetic disorder and open circuit voltage in bulk heterojunction organic solar cells", Phys. Rev. B. 84, 075210 (2011).

[136] 28. T. Kirchartz et. al., "Meaning of reaction orders in polymer:fullerene solar cells", Phys. Rev. B, 86, 165201 (2012).

[137] J. Bhattacharya et. al., "Photo-induced changes in fundamental properties of organic solar cells", Appl. Phys. Lett., 100, 193501, 2012.

[138] V. Dalal et. al, "Stability of organic solar cells", IEEE International Reliability Physics Symposium (IRPS), 2012, pages 4.A.5.1-4.A.5.4.

[139] A. Kumar et. al., "Origin of radiation-induced degradation in polymer solar cells", 2010, 20, 2729-2736.

[140] R. A. Street, "Radiation induced recombination centers in organic solar cells", Phys. Rev. B, 85, 205211(2012).

[141] C. H. Peters et. al., "The mechanism of Burn-in Loss in a high efficiency polymer solar cell", Advanced Materials, 2012, 24, 663-668.

[142] R. Pierret, "Advanced Semiconductor Fundamentals", Second Edition, Prentice Hall, 2003, page 161.

[143] R. Pierret, "Advanced Semiconductor Fundamentals", Second Edition, Prentice Hall, 2003, page 152.

[144] R. C. MacKenzie et. al., "Extracting microscopic device parameters from transient photocurrent measurements of P3HT:PCBM solar cells", Advanced Energy Materials, 2012, 2, 662-669.

[145] J. A. Carr, "The identification and characterization of electronic defect bands in organic photovoltaic devices", PhD Dissertation, Iowa State University, page 127, 2014.

[146] H. Kang et. al., "Controlling number of Indene solubilizing groups in multiadduct fullerenes for tuning optoelectronic properties and open-circuit voltage in organic solar cells", 2012, 4, 110-116.

[147] A. Nardes et. al., "Beyond PCBM: Understanding the photovoltaic performance of blends of Indene-C 60 multiadducts with Poly(3-hexylthiophene)", Advanced Functional Materials, 2012, 22, 4115-4127.

[148] S. Albrecht et. al., "Fluorinated copolymer PCPDTBT with enhanced open-circuit voltage and reduced recombination for highly efficient polymer solar cells", Journal of the American Chemical Society, 2012, 134, 14932-14944.

[149] S. Albrecht et. al., "On the Field Dependence of Free Charge Carrier Generation and Recombination in Blends of PCPDTBT/PC70BM: Influence of Solvent Additives", Journal of Physical Chemistry Letters, 2012, 640-645.

[150] R. Street et. al., "Kinetics of light induced defect creation in organic solar cells", Applied Physics Letters 102, 043305 (2013).
[151] S. Pattnaik et. al., "Novel hybrid amorphous/organic tandem junction solar cell", IEEE Journal of Photovoltaics", Vol. 3, No. 1, Jan 2013.

[152] K. Gosh, "Modeling of amorphous silicon/crystalline silicon heterojunction by commercial simulator", Master's Thesis, University of Delaware, 2008, page 13.

[153] D. Diouf et. al., "Two Dimensional simulations of integrated back contact silicon heterojunction solar cells", Physics and Technology of Amorphous-Crystalline Heterostructure Silicon Solar Cells, Springer, 2012, 978-3-642-22274-0.

[154] M. Samiee et. al., "More stable hybrid organic solar cells deposited on amorphous Si electron transfer layer", Applied Physics Letters 104, 213909 (2014).

[155] E. Ratcliff et. al., "Selective interlayers and contacts in organic photovoltaic cells", Journal of Physical Chemistry Letters, 2011, 2(11), pp 1337-1350.

156 M. Izu et. al., "Continuous roll-to-roll amorphous silicon photovoltaic manufacturing technology", NREL Semi-anuual subcontract report, NREL/TP-411-6624, 1994. Available at: http://www.nrel.gov/docs/legosti/old/6624.pdf

157 M. de Jong et. al., "Stability of the interface between indium-tin-oxide and poly(3,4-ethylenedioxythiophene)/poly(styrenesulfonate) in polymer light-emitting diodes" , Applied Physics Letters 77, 2255 (2000).

158 W. Lindemann et. al., "An X-ray fluorescence study on the segregation of Cs and I in an inverted organic solar cell", Organic Electronics 14 (2013) 3190-3194.

159 W. Lindemann et. al., "The effect of cesium carbonate on 1-(3-methoxycarbonyl) propyl-1-phenyl[6,6]C61 aggregation in films", Applied Physics Letters 105, 191605 (2014).

160 A. Tabata et. al., "Band gap control of hydrogenated amorphous silicon carbide films prepared by hot-wire chemical vapor deposition", Journal of Non-crystalline Solids 338-340 (2004) 521-524.

161 A. Tabata et. al., "Properties of hydrogenated amorphous silicon carbide films prepared by a separately excited plasma CVD method", Journal of Physics D: Applied Physics 30 (1997) 194-201.

162 J. Bhattacharya, "Understanding the physics of degradation of polymer solar cells", PhD dissertation, 2013, pages 45-48.

163 Sarah Kurtz et. al., "High efficiency cells for large scale electricity generation", UC Merced solar symposium, September 2008.

164 With modifications from: T. Ameri et. al., "Organic tandem solar cells: A review", Energy and Environmental Science, 2009, 2, 347-363.

165 G. Sun et. al., "High efficiency thin-film crystalline Si/Ge tandem solar cell", Optics Express, Vol. 18, Issue 4, pp. 3746-3753 (2010).

166 S. Pattnaik et. al., "Novel hybrid amorphous/organic tandem junction solar cell", IEEE Journal of Photovoltaics", Vol. 3, No. 1, Jan 2013.

167 J. Kim et. al. , "10.5% efficient polymer and amorphous silicon hybrid tandem photovoltaic cell", Nature Communications, DOI: 10.1038/ncomms7391, 2015.

168 V. Dalal et.al., "Efficient Tandem Junction Organic/Inorganic Hybrid solar cells", 25th International conference on Amorphous and Nanocrystalline Semiconductors (ICANS 25), B3.4, Toronto, Canada, 2013.

169 S. Albrecht et. al., Efficient hybrid inorganic/organic tandem solar cells with tailored recombination contacts, Vol. 127, pp. 157-162, 2015.

170 W. Qin et. al., "High efficiency organic/a-Si tandem solar cells with complementary light absorption", J. Mater. Chem. A, 2014, 2, 15303.

171 J. H. Seo et. al., "High efficiency inorganic/organic hybrid tandem solar cells", Adv. Mater. 2012, 24, 4523-4527.

172 T. Kim et. al., "Reversed organic–inorganic hybrid tandem solar cells for improved interfacial series resistances and balanced photocurrents", Synthetic Metals, 175 (2013) 103-107.

173 S. H. Park, "Tandem solar cells made from amorphous silicon and polymer bulk heterojunction sub-cells", Adv. Mat. 2015, 27, 298-302.

174 L. Duo et. al., "Synthesis of 5H‑Dithieno[3,2‑b:2′,3′‑d]pyran as an electron-rich building block for donor–acceptor type low-bandgap polymers", Macromolecules, 2013, 46, 3384-3390.

175 A. Kojima et. al., "Organometal halide perovskites as visible-light sensitizers for photovoltaic cells", Journal of the American Chemical Society, 2009, 131(17), pp 6050-6051.

176 M. A. Green et. al., "The emergence of perovskite solar cells", Nature Photonics 8, 506-514 (2014).

177 E. J. Juarez-Perez et. al., "Photoinduced giant dielectric constant in lead halide perovskite solar cells", Journal of Physical Chemistry Letters, 2014, 5, 2390-2394.

178 V. D'Innocenzo et. al., "Excitons versus free charges in organo-lead tri-halide perovskite", Nature Communications, 5:3586, DOI: 10.1038/ncomms4586.

179 K. Tanaka et. al., "Comparative study on the excitons in lead-halide-based perovskite-type crystals $CH_3NH_3PbBr_3$ $CH_3NH_3PbI_3$", Solid State Communications 127 (2003) 619-623.

180 S. D. Stranks et. al., "Electron-hole diffusion lengths exceeding 1 micrometer in an organometal trihalide perovskite absorber", Science, Vol. 342, No. 6156, pp. 341-344.

181 G. Xing et. al., "Long-range balanced electron- and hole-transport lengths in Organic-Inorganic CH3NH3PbI3", Science, Vol. 342, No. 6156, pp. 344-347.

182 Y. Zhao et. al., "Solid-state mesostructured perovskite $CH_3NH_3PbI_3$ solar cells: charge transport, recombination, and diffusion length", Journal of Physical Chemistry Letters, 2014, 5(3), pp. 490-494.

[183] M. Liu et. al., "Efficient planar heterojunction perovskite solar cells by vapor deposition", Nature 501, 395-398.

[184] P. Schulz et. al., "Interface energetics in organo-metal halide perovskite-based photovoltaics", Energy and Environmental Science, 2014, 7, 1377-1381.

[185] H. Yu et. al., "The role of chlorine in the formation process of $CH_3NH_3PbI_{3-x}Cl_x$ perovskite", Advanced Functional Materials, 2014, 24, 7102-7108.

[186] J. –W. Lee et. al., "Rutile TiO_2-based perovskite solar cells", Journal of Material Chemistry A, 2014, 2, 9251-9259.

[187] M. M. Lee et. al., "Efficient Hybrid Solar Cells Based on Meso-Superstructured Organometal Halide Perovskites", Science, Vol. 338, No. 6107, pp. 643-647, 2012.

[188] K. Wojciechowski et. al., "Sub-150 °C processed meso-superstructured perovskite solar cells with enhanced efficiency", Energy and Environmental Science, 2014, 7, 1142-1147.

[189] J. You et. al., "Low-Temperature Solution-Processed Perovskite Solar Cells with High Efficiency and Flexibility", ACS Nano, 2014, 8(2), pp 1674-1680.

[190] J. –Y. Jeng et. al., "Nickel Oxide Electrode Interlayer in CH 3 NH 3 PbI 3 Perovskite/PCBM Planar-Heterojunction Hybrid Solar Cells", Advanced Materials, 2014, 26, 4107-4113.

[191] Z. Gu et. al., "Novel planar heterostructure perovskite solar cells with CdS nanorods array as electron transport layer", Solar Energy Materials and Solar Cells 140 (2015) 396-404.

[192] D. Liu et. al., "Compact Layer Free Perovskite Solar Cells with 13.5% Efficiency", Journal of American Chemical Society, 2014, 136, 17116-17122.

[193] K. Mahmood et. al., "Double-layered ZnO nanostructures for efficient perovskite solar cells", Nanoscale, 2014, 6, 14674-14678.

[194] Y. Guo et. al., "Enhancement in the efficiency of an organic–inorganic hybrid solar cell with a doped P3HT hole-transporting layer on a void-free perovskite active layer", Journal of Materials Chemistry A, 2014, 2, 13827.

[195] Z. Zhu et. al., "High-Performance Hole-Extraction Layer of Sol–Gel-Processed NiO Nanocrystals for Inverted Planar Perovskite Solar Cells", Angewandte Chemie, 2014, 126, 12779-12783.

[196] J. Kim et. al., "High-Performance and Environmentally Stable Planar Heterojunction Perovskite Solar Cells Based on a Solution-Processed Copper-Doped Nickel Oxide Hole-Transporting Layer", Advanced Materials, 2015, 27, 695-701.

[197] J. Even et. al., "Importance of Spin–Orbit Coupling in Hybrid Organic/Inorganic Perovskites for Photovoltaic Applications", Journal of Physical Chemistry Letters, 2013, 4(17), pp. 2999-3005.

[198] E. Mosconi et. al., "First-Principles Modeling of Mixed Halide Organometal Perovskites for Photovoltaic Applications", Journal of Physical Chemistry C, 2013, 117(27), pp. 13902-13913.

[199] Z. -K. Tan et. al., "Bright light-emitting diodes based on organometal halide perovskite", Nature Nanotechnology 9, 687-692 (2014).

[200] http://www.pveducation.org/pvcdrom/solar-cell-operation/tandem-cells

[201] M. Filipic et. al., "CH3NH3PbI3 perovskite / silicon tandem solar cells: characterization based optical simulations", Optics Express, Vol. 23, Issue 7, pp. A263-A278 (2015).

[202] G. Balaji, P. Joshi, H. A. Abbas, L. Zhang, R. Kottokkaran, M. Samiee, M. Noack, V. L. Dalal, "CH3NH3PbI3 from non-iodide lead salts for perovskite solar cells via formation of PbI2", Physical Chemistry Chemical Physics, 2015, 17, 10369.

[203] T. –B. Song et. al., "Perovskite solar cells: film formation and properties", Journal of Materials Chemistry A, 2015, 3, 9032-9050.

[204] M. Samiee, S. Konduri, B. Ganapathy, R. Kottokkaran, H. A. Abbas, A. Kitahara, P. Joshi, L. Zhang, M. Noack, and V. Dalal, "Defect density and dielectric constant in perovskite solar cells", Applied Physics Letters, 105, 153502 (2014).

[205] H. Abbas, R. Kottokaran, B. Ganapathy, M. Samiee, L. Zhang, A. Kitahara, M. Noack, and V. Dalal, "High efficiency sequentially vapor grown CH3NH3PbI3 perovskite solar cells", APL Materials 3, 016105 (2015).

[206] S. Colella et. al., "MAPbI$_{3-x}$Cl$_x$ mixed halide perovskite for hybrid solar cells: The role of chlorine as dopant on the transport and structural properties", Chemistry of Materials, 2013, 25, 4613-4618.

[207] J. Zhao et. al., "Improvements in silicon solar cell performance", Conference Record of the 2nd IEEE Photovoltaic Specialists Conference (PVSC) 1991.

[208] N. Noel et. al., "Enhanced Photoluminescence and Solar Cell Performance via Lewis Base Passivation of Organic Inorganic Lead Halide Perovskites", Vol. 8, No. 10, 9815-9821, 2014.

[209] H. -S. Duan et. al., "The identification and characterization of defect states in hybrid organic–inorganic perovskite photovoltaics", Physical Chemistry Chemical Physics, 2015, 17, 112-116.

APPENDIX A
MEASUREMENT OF DEFECT DENSITIES AND URBACH ENERGIES OF TAIL STATES IN PTB7 SOLAR CELLS

Mehran Samiee,[1] Pranav Joshi,[1] Damir Aidarkhanov,[2] and Vikram Dalal[1]

[1]Department of Electrical and Computer Engineering, Iowa State University, Ames, Iowa 50011, USA.

[2] Nazarbayev University, Astana, Kazakhstan

Abstract- Poly[[4,8-bis[(2 ethylhexyl)oxy]benzo[1,2-b:4,5-b$^{'}$]dithiophene-2,6-diyl] [3-fluoro 2[(2ethylhexyl)carbonyl] Thieno[3,4-b]thiophenediyl]] (PTB7) is an important material for solar cells. We report on measurement of bulk and interfacial defects in PTB7 devices and measurement of Urbach energies of tail states near the HOMO and LUMO levels. The bulk defects and Urbach energies were measured using sub-gap quantum efficiency techniques and the donor/acceptor interfacial defects using capacitance techniques. Interfacial defects were found to peak at ~0.7 eV above the HOMO level. Dark current-voltage curve indicated both interfacial and bulk recombination. Urbach energy for tail states near the HOMO level of PTB7 is 33 meV and near the LUMO level 55 meV. © 2014. *AIP Publishing LLC.* [http://dx.doi.org/10.1063/1.4896782]

Organic solar cells are an increasingly important photovoltaic technology. Recently, efficiency of >9% has been achieved in bulk heterojunction solar cells fabricated from the heterojunction material system Poly[[4,8-bis[(2-ethylhexyl)oxy] benzo[1,2-b:4,5-b0]dithiophene-2,6-diyl][3-fluoro-2-[(2-ethylhexyl)carbonyl]thieno[3,4 b]thiophenediyl]] (PTB7)/ [Phenyl-C71- Butyric-Acid-Methyl Ester] (PCBM).[1,2] The electronic performance of

this material, in common with other organic solar cell materials,[3–8] depends critically upon fundamental material parameters such as interfacial defects at the donor/ acceptor interface, tail state, and midgap defects in PTB7, and Urbach energy of tail states near the HOMO and LUMO levels of PTB7. In this paper, we measure these fundamental parameters in the PTB7/PCBM solar cell. We also show that a careful analysis of the dark current measured at various temperatures reveals two distinct recombination mechanisms, an interface controlled and a bulk controlled recombination.

The solar cell samples were standard donor/acceptor solar cells deposited on ITO coated glass. The donor material was PTB7, and the acceptor was either PCBM70 or idene-C60 bisadduct (ICBA).[9] The basic device structure is shown as an inset in Fig. 1(a). It consists of a hole transfer layer poly (3,4-ethylenedioxythiophene):poly(styrenesulfonate) (PEDOT:PSS), a mixed hetero-junction layer of PTB7/ PCBM prepared by spin-coating form a dichlorobenzene solution, and an evaporated Ca/Al contact. The samples were annealed after deposition at varying temperatures between 80 and 150 C. It was found that annealing above 110 C resulted in poorer performance. A major benefit of the annealing process was that the shunt leakage conductance of the devices decreased by orders of magnitude after annealing. This fact is of significant importance when one tries to fit dark I-V curves to device models, as explained later. In Fig. 1(a), we show the illuminated I-V curves for the samples annealed at 80 C and 110 C. The solar conversion efficiency is approximately 7.5% for the sample annealed at 80 C.

For measuring deep defects, a subgap quantum efficiency (QE) technique was employed.[7,8] Fig. 2 (left panel), shows the band diagram of the heterojunction solar cell with the various states and potential optical transitions, labeled as (a)–(h). Note that there is likely to be a continuous density of states (DOS) throughout the bandgap of the donor and acceptor; hence,
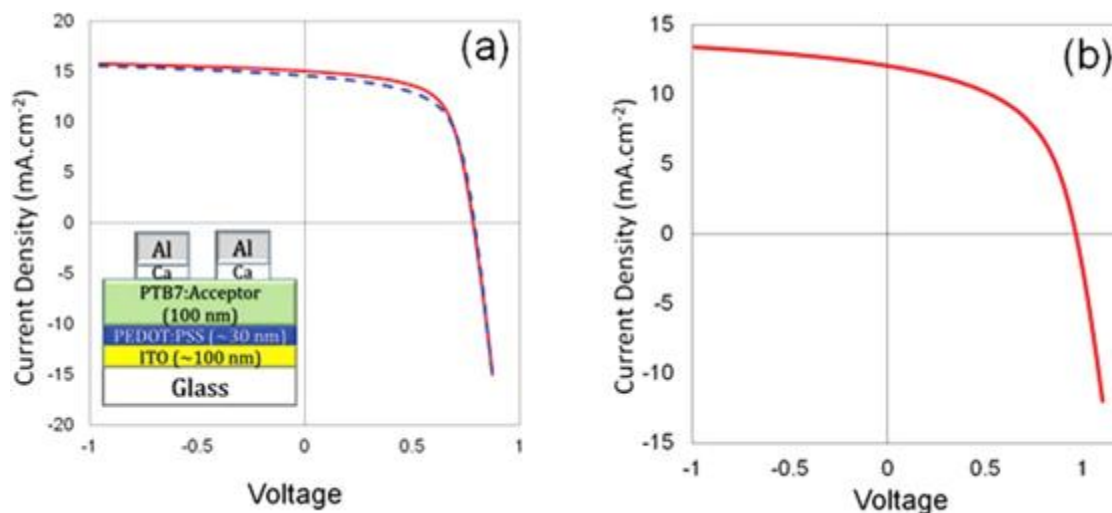
FIG.1.. I-V curve under AM1.5 illumination for two PTB7/PCBM70 solar cells annealed at different temperatures; (a) is for the cell prepared with a PCBM acceptor and (b) with an ICBA acceptor. The solid line is for a cell annealed at 80 C after growth, and the dotted line for a cell annealed at 110 C. Inset in (a) shows a schematic diagram of the cell.
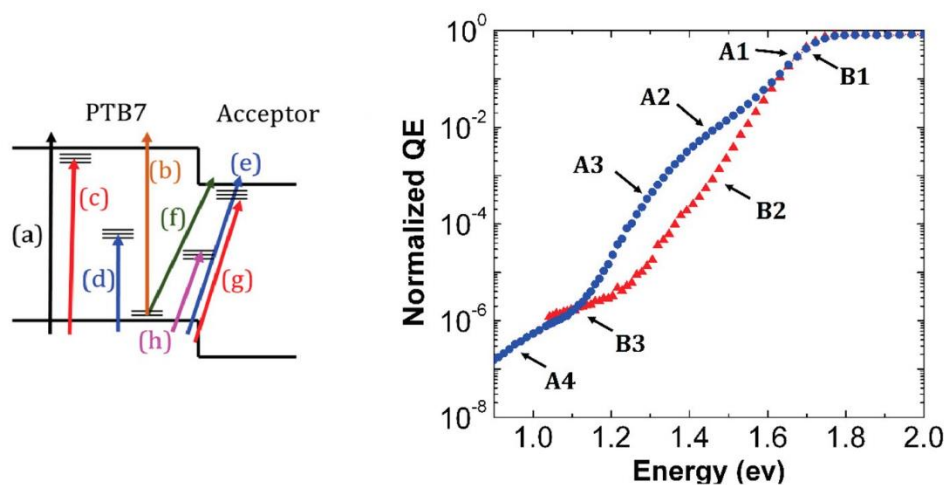

FIG. 2. Schematic diagram showing various states and possible optical tran- sitions (top panel) and measured subgap QE data (bottom panel). The two subgap QE data are for PTB7/PCBM cell (dots) and PTB7/ICBA cell (trian- gles). The heterojunction bandgap increases by 0.2 eV when ICBA is used as the acceptor as opposed to when PCBM70 is used as the acceptor. A com- parison of the two curves allows one to distinguish between tail states in PTB7 near the HOMO level and near the LUMO level. The fact that curves A3 and B2 are parallel indicates that they represent transitions from the same states, namely, tail states near the HOMO level.

the DOS shown is only meant to be illustrative of major categories of states. Transition (a) is due

to band-to-band (excitonic) transition in the donor. Arrow (b) represents excitation from

the tail states near the HOMO level of donor to the LUMO level of the donor. Transition (c) is from the HOMO level of the donor to the tail states near the LUMO level of the donor. Transition (d) is from the HOMO level of the donor to midgap states in the donor. Transition (e) is from HOMO level of donor to the LUMO level of the acceptor. Arrow (f) represents transition from tail states near the HOMO of donor to the LUMO of acceptor. Arrow (g) represents transition from HOMO of donor to tail states near the LUMO of acceptor. Arrow (h) represents transition from the HOMO level of the donor to midgap states at the interface. These optical assignments are similar to the assignments by Street et al.[7] for other polymers, except that we also include interfacial transitions. Note that there will be additional exci- tonic transitions within the donor due to the presence of an exciton; however, these transitions are submerged within the disorder-governed transitions. The presence of disorder is precisely why one does not see an excitonic peak in optical absorption, unlike, for example, in GaAs where at low temperatures, there is a prominent excitonic peak.

The experimental subgap QE curve for the PTB7/PCBM device is shown in Fig. 2 (right panel) as curve A. It shows a band-to-band excitonic excitation at energies >1.8 eV, corresponding to transitions marked (a) in the left panel, and then a rapid fall-off in excitation down to 1.37 eV (labeled A1 and A2 in the right panel), at which point there is a distinct change in slope with a sharper fall-off in QE (curve labeled A3). It is reasonable to assume that the sharp change in slope below 1.37 eV corresponds to transitions from filled tail states near the HOMO level of donor to the LUMO of the acceptor (transition (f)), and its exponential slope is a measure of the decreasing tail state density near the HOMO level of the donor. In inorganic materials, this would be called the Urbach energy

of tail states. In organic polymer materials, because of the significant structural disorder (poly-dispersity), one also expects and finds a tail state distribution and an Urbach energy, as pointed out by Street et al.,[3,7]Kirchartz et al.,[10] and Foertig et al.[11] Urbach tail has also been observed in small molecule solar cells.[12]

Since the heterojunction bandgap is about 1.35–1.4 eV, the initial rapid decrease in QE (absorption) at energies below 1.8 eV must correspond to either transitions from tail states near the HOMO level of donor to the LUMO level of donor (transition labeled (b)), or from HOMO level of donor to tail states near the LUMO level of donor (transition labeled (c)). To separate these two phenomena, we prepared device samples using an alternative acceptor, ICBA. The I-V curve for this device is shown in Fig. 1(b). It shows a higher open circuit voltage (~0.98 V) compared to the device prepared using PCBM70 whose voltage was 0.78 V, but the current and the fill factor are poor. It is believed that the enhanced voltage is due to a higher LUMO level in ICBA compared to PCBM70 with a resultant higher heterojunction bandgap. [9,13]

The data for subgap QE of the PTB7/ICBA heterojunction cell are also shown in Fig. 2 (right panel) as curve labeled B. Looking at the two subgap QE data carefully (curves A and B), the QE for both starts dropping at 1.8 eV, and the curves for PCBM70 and ICBA coincide down to 1.6 eV. Below that energy, the curves diverge. It is believed that the LUMO level in ICBA is higher than in PCBM70, hence the higher voltage. [9,13] Fig. 2 confirms this observation, showing a shift in subgap QE curve for ICBA of to higher energies by about 0.2 eV.

To understand the subgap QE data, we refer back to Fig. 2 (top panel). Using that figure, one can now say that the data for curve labeled A1 from slightly below 1.8 eV

down to 1.37 eV correspond to transitions from the HOMO level of PTB7 to the empty tail states near the LUMO level of PTB7 (transition labeled (c) in left panel of Fig. 2). Below 1.37 eV, the curve A3, with a different slope, corresponds to transitions from the tail states near the HOMO level of PTB7 to the LUMO level of the acceptor PCBM70 (transition labeled (f) in top panel).

In the case of ICBA acceptor, the initial part of the decrease in QE (curve B1), which matches curve A1, corresponds to the same transitions in PTB7 as found with PCBM acceptor. However, at energies below 1.6 eV, an alternative path becomes possible for samples with ICBA acceptor, namely, from the tail states near HOMO level of donor to the LUMO level of acceptor (transition labeled (f) in left panel of Fig. 2). This part of the ICBA device QE curve is labeled B2. If this is the case, the QE curve for PTB7/PCBM70 device below 1.37 eV (curve A3) must be parallel to the QE curve for the PTB7/ICBA device below 1.6 eV (curve B2), since they correspond to transitions from the same tail states. From Fig. 2(right), it is apparent that the curves A3 and B2 are indeed parallel to each other. The QE curve for ICBA (curve B2) continues down to ~1.3 eV as an approximate straight line on a log plot, until transitions to midgap states of PTB7 become important at ~1.3 eV (curve B3). Based on this analysis, we can calculate the Urbach energy for tail states near the LUMO level of PTB7, using curve A2, as being ~55 meV, and for tail states near the HOMO level of PTB7, using curve A3, as being ~33 meV. Note also that the poor fill factor for PTB7/ICBA device implies that there is much more recombination in this material, presumably a result of higher defect density, than in the PTB7/PCBM cell. A higher defect
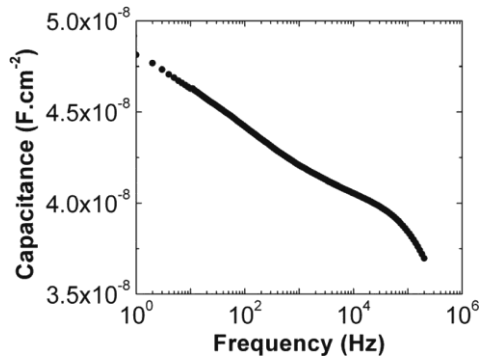
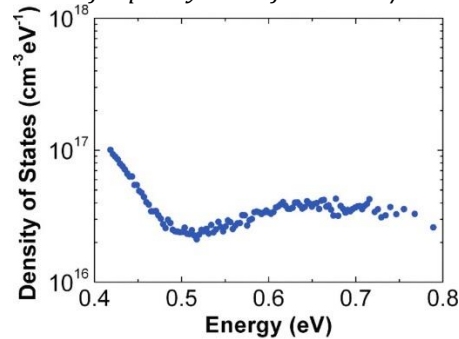FIG. 3 *Capacitance-frequency curve for a PTB7/PCBM70 cell.*

FIG. 4. Density of defects plotted vs. energy. Note the peak at 0.7 eV, approximately the midgap region of the interfacial gap. The initial falloff is due to filling and emptying of tail states. While the density is plotted as #/cm3, the midgap density can be changed to #/cm2 by assuming spherical domains and multiplying by d/3, where d is the domain diameter.

density would imply the subgap QE curve for ICBA acceptor (curve B3) to bend over at higher energies and have higher values when compared to the PCBM acceptor case (curve B3 vs. curve A4), which is indeed the case as shown in Fig. 2(right).

We measured deep defect densities using capacitance-frequency techniques.[8,14–17] The method used is capacitance-frequency measurements where the defect density at a particular energy level is determined from the slope dC/df of the capacitance-frequency data, and the energy level determined by assigning an attempt to escape frequency.[8,14–17]

The data for capacitance vs. frequency for PTB7/PCBM cell are shown in Fig. 3, and the derived defect densities vs. energy of the mid-gap states in Fig. 4. Note that the defects

appear to peak at around 0.7 eV, approximate midgap of the heterojunction bandgap. The sharp drop in density near 0.4–0.5 eV represents trapping in the tail states of PTB7. Note that we also measured interfacial defect densities in PTB7/ICBA cells, and they were found to be higher than for PTB7/PCBM cell, as expected from the worse I-V curve for such devices shown in Fig. 1 and from subgap QE data for such cells shown in Fig. 3.

We measured diode dark current at various temperatures for the PTB7/PCBM cell. The data for various temperatures are shown in Fig. 5(a), and it shows a classical two region dark I-V relationship,[18] obviously apparent at low temperatures. The data at all temperatures can be deconvoluted into three parts, given by the following equation:

$$I = \frac{V}{R_{sh}} + I_{01}\left(e^{\left(\frac{qV}{n_1 kT}\right)} - 1\right) + I_{02}\left(e^{\left(\frac{qV}{n_2 kT}\right)} - 1\right) \tag{1}$$
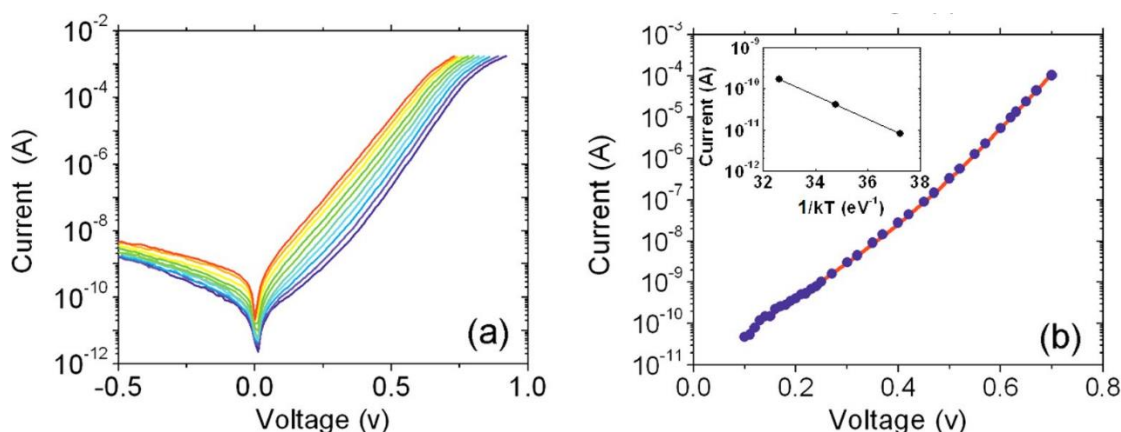

FIG. 5. Dark I-V curves measured at varying temperatures from 28 C to 100 C for a PTB7/PCBM70 cell (left panel). As the temperature increases, the dark current increases. The bottom panel is a fit of the dark current vs. voltage measured at 38 C (red dots) after subtracting the shunt resistance of 1×10^9 Ω, fitted against calculated total current (solid line) calculated with addition of two currents, $I_1 = I_{o1}[exp(qV/n_1kT)-1]$ and $I_2 = I_{o2}[exp(qV/n_2kT)-1]$, with $n_1 = 2.0$ and $n_2 = 1.18$. The values for n_1 and n_2 indicate recombination through midgap interfacial states, and through band-band states (modified by the large tail state density near the band edges), respectively. The inset in the right figure shows a plot of log (I_{o1}) vs. (1/kT), yielding a value of activation energy of 0.65 eV, close to midgap value of the interfacial gap, showing that midgap states at the interface are dominating this part of the current.

After subtracting for the current due to shunt resistance (fit from the forward I-V data to be 1×10^9 Ω, same value obtained at all temperatures), we obtain the curve shown in Fig. Fig. 5(b) for the sample measured at 38 C, and obtain a value of $I_{o1} = 8 \times 10^{-12}$ A and $n_1 = 2$; $I_{o2} = 3.5 \times 10^{-14}$ A and $n_2 = 1.18$. Note that one cannot use the current at reverse voltages to estimate true shunt resistance, because under reverse bias, when the fields are very high, one can also get emission from deep states because of the Frankel-Poole tunneling effect.[19] The values for n_1 and n_2 are close to the classical values of 2 and 1. The n_1 and n_2 values for all other temperatures are very similar to the values obtained at 38C. The n1 value of 2 implies a mid-gap state dominated generation-recombination current[18]—in this case, due to the interfacial states. The reason the dark current at higher temperatures appears to tend to a single exponential is because the band-band excitation across the heterojunction is proportional to n_i^2, where n_i is the intrinsic concentration in whichever material has the lower doping (in this case, the donor), whereas the current generated by recombination at the interface is proportional to n_i. The ratio of n_i^2 to n_i is proportional to exp $(-E_g/2kT)$, where E_g is the interfacial bandgap, and the ratio increases with temperature, thus leading to an apparent single exponential at higher temperatures.

One can obtain further information about the energetic location of the states controlling I_{o1} by plotting the measured dark current prefactor I_{o1} vs. temperature. This is shown as an inset in Fig. 5(b), which shows an activation energy of 0.65 eV, showing that it is indeed the midgap region of the heterojunction interface that is dominating recombination-generation in the dark. This observation agrees with the assignment of ~0.7 eV peak in defect density observed by capacitance measurement, thereby confirming that both measurements refer to interfacial states at the donor/acceptor interface.

In summary, we have measured several significant material parameters related to the operation of high performance PTB7-based solar cells. We have found values for the Urbach energy of tail states in PTB7 near both the HOMO and LUMO levels of the donor. We have also measured the defect densities at the interface, and shown that they play a role in determining recombination in the dark and the dark current.

References:

[1] Y. Liang, Z. Xu, J. Xia, S.-T. Tsai, Y. Wu, G. Li, C. Ray, and L. Yu, Adv. Mater. 22, E135 (2010).

[2] Z. He, C. Zhong, S. Su, M. Xu, H. Wu, and Y. Cao, Nat. Photonics 6, 591(2012).

[3] R. A. Street, A. Krakaris, and S. R. Cowan, Adv. Funct. Mater. 22, 4608 (2012).

[4] R. A. Street, Phys. Rev. B 84, 075208 (2011).

[5] R. A. Street, J. E. Northrup, and B. S. Krusor, Phys. Rev. B 85, 205211 (2012).

[6] R. A. Street, Science 341, 1072 (2013).

[7] R. A. Street, K. W. Song, J. E. Northrup, and S. J. Cowan, Phys. Rev. B 83, 165207 (2011).

[8] J. Bhattacharya, R. W. Mayer, M. Samiee, and V. L. Dalal, Appl. Phys. Lett. 100, 193501 (2012).

[9] Y. He, H. Y. Chen, J. Hou, and Y. Li, J. Am. Chem. Soc. 132, 1377 (2010).

[10] T. Kirchartz, B. E. Pieters, J. Kirkpatrick, U. Rau, and J. Nelson, Phys. Rev. B 83, 115209 (2011).

[11] A. Foertig, J. Rauh, V. Dyakonov, and C. Deibel, Phys. Rev. B 86, 115302 (2012).

[12] B. Song, C. Rolin, J. D. Zimmerman, and S. R. Forrest, Adv. Mater. 26, 2914 (2014).

[13] Y.-J. Cheng, C.-H. Hsieh, Y. He, C.-S. Hsu, and Y. Li, J. Am. Chem. Soc. 132, 17381 (2010).

[14] T. R. Walter, T. R. Herberholz, C. Muller, and H. W. Schock, J. Appl. Phys. 80, 4411 (1996).

[15] P. P. Boix, G. Garcia-Belmonte, U. Munecas, M. Neophytou, C. Waldauf, and R. Pacios, Appl. Phys. Lett. 95, 233302 (2009).

[16] J. A. Carr and S. Chaudhary, Appl. Phys. Lett. 100, 213902 (2012).

[17] G. Balaji, M. S. Esfahani, P. Joshi, J. Bhattacharya, M. Jefferies-El, and V. Dalal, Eur. Polym. J. 49(12), 3921 (2013).

[18] J. L. Moll, Physics of Semiconductors (McGraw Hill, 1964).

[19] V. L. Dalal, R. Knox, and B. Moradi, Sol. Energy Mater. Sol. Cells 31, 349 (1993).

APPENDIX B
MORE STABLE HYBRID ORGANIC SOLAR CELLS DEPOSITED ON AMORPHOUS Si ELECTRON TRANSFER LAYER

Mehran Samiee,[1] Brian Modtland,[1] Damir Aidarkhanov,[2] and Vikram L. Dalal[1].

[1]Iowa State University, Dept. of Electrical and Computer Engineering, Ames, Iowa 50011, USA

[2]Nazarbayev University, Astana, Kazakhstan

Abstract- We report on defect densities, performance, and stability of organic/inorganic hybrid solar cells produced using n-doped inorganic amorphous silicon-carbide layers as the electron transport layer (ETL). The organic material was poly-3-hexyl-thiophene (P3HT) and heterojunction was formed using phenyl-C71-Butyric-Acid-Methyl Ester (PCBM). For comparison, inverted solar cells fabricated using Cs_2CO_3 as ETL were fabricated. Defect densities and subgap quantum efficiency curves were found to be nearly identical for both types of cells. The cells were subjected to 2X sun illumination and it was found that the cells produced using doped a-Si as ETL were much more stable than the cells produced using Cs_2CO_3. © 2014 AIP Publishing LLC. [http://dx.doi.org/10.1063/1.4878405]

Organic solar cells are generally fabricated using oxide or metallic layers as electron transport layers. For example, the ubiquitous P3HT/PCBM system of cells is fabricated in either the normal mode (p-i-n configuration), where light enters first through the hole transport layer (HTL) into the active bulk hetero-junction,[1–5] or in the inverted mode[6,7] (n-i-p configuration) where light enters through an electron injecting layer (ETL). Typical materials which are used as HTL are PEDOT:PSS or MoO_3, and for ETL, Cs_2CO_3, or ZnO.[8] Some of the materials, such as PEDOT:PSS, are hygroscopic and release oxygen upon UV

illumination, leading to instability of the organic cell. In general, for optimum performance, the electron affinities of the inorganic electron-transporting layers should be matched to the LUMO level of the electron acceptor (PCBM in this case), and also similarly, the HOMO level of the donor material (P3HT in this case) should be close to the valence band of the hole transport layer. This is often difficult to do with large bandgap oxide layers such as MoO_3 or Cs_2CO_3 or ZnO. In contrast, doped thin film semiconductors offer a very wide choice in bandgap and electron affinities and can be utilized for both hole and electron injecting contacts. In this paper, we report on the use of one such material, n-doped a-Si:H (amorphous Si) and a-(Si,C):H (amorphous Silicon-Carbide) alloys as electron transporting layers (ETL) for producing high quality P3HT/PCBM solar cells. This system offers unique advantages in being able to dope the electron transporting layer heavily, thereby assuring an ohmic tunnel-junction contact with the transparent conducting layer such as ZnO, and also systematically change the positions of the conduction and valence bands by mixing Si with Ge and C. In general, adding C will tend to move up the conduction band and move down the valence band, increasing the bandgap,[9] whereas adding Ge will primarily move up the valence band and decrease the bandgap.[10] A feature of adding C is that the increase in bandgap allows for less absorption of blue and UV photons in the electron transporting layer. A further significant advantage is that a-Si is almost completely inert to moisture or oxygen ingress,[11] and thereby prevents these atmospheric contaminants from affecting the performance of the solar cell.[12,13] Other doped inorganic material systems are also possible to use as ETL, but one must be careful to make sure that the organic cells, whose properties depend so strongly on the morphology of the cell, have good electronic properties when deposited on doped inorganic materials. In this paper, we show

Samiee et. al., Appl. Phys. Lett. 105, 213909 (2014)

experimentally that indeed, when a-Si is used as the doped inorganic ETL, the fundamental properties of the P3HT/PCBM cell are very similar to the traditional cells deposited on Cs_2CO_3 ETL. The configuration of the n-i-p or inverted solar cell is shown in Fig 1. It consists of an Al-doped ZnO film, deposited on a glass substrate, on which ETL of n-doped a-Si:H or a-(Si,C):H is deposited using plasma-enhanced CVD process.[14] Silane, hydrogen, and phosphine gas are used to deposit the n+ layer. For depositing a-(Si,C):H layer, methane is added to the gas mixture. Typical Tauc bandgap for the a-Si:H layer is 1.8 V and for a-(Si,C):H layer, 1.9 eV. The ETL is followed by spin-coating of bulk heterojunction cell using procedures described previously.[1–5] This is followed by evaporation of MoO_3 as the hole transport layer and then evaporating Al as the ohmic contact. The comparison cell used spin-coated Cs_2CO_3 as the electron transporting layer.
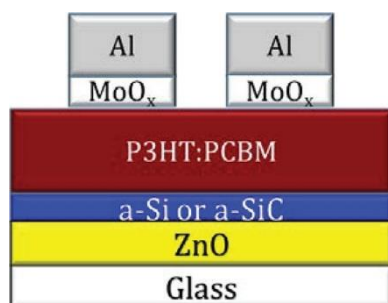

FIG. 1. Schematic diagram of inverted solar cell structure with an n-type doped a-Silicon ETL.

In Fig. 2, we show the illuminated I-V curves for both types of cells, the hybrid a-Si/P3HT/PCBM cell and the Cs2CO3/P3HT/PCBM cell. Both types of cells show similar high fill factors (65%) and open-circuit voltages, with the voltage for the cell deposited on a-Si:H layer being slightly higher. However, the short-circuit current for the cell with aSi:H ETL
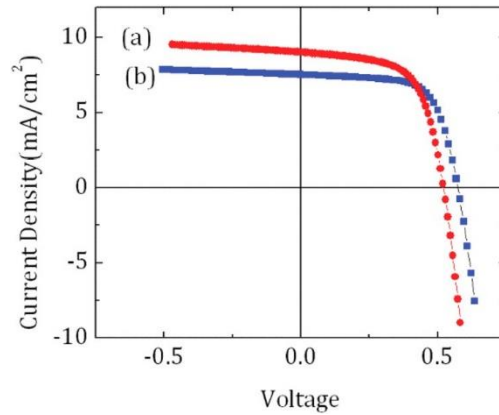
FIG. 2. Illuminated J-V curves of inverted cells deposited on Cs₂CO₃ (curve a) and on n-doped a-Si (curve b). Note how the current density is lower when a-Si is used as the electron transport layer, but the voltage and fill factor are higher. The voltage on Cs₂CO₃ substrate is 0.53 V, and on a-Si, 0.57 V, and the respective fill factors were 0.63 and 0.67.
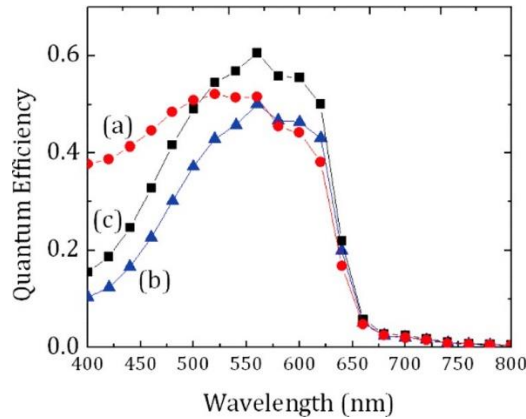

FIG. 3. Quantum efficiency for cells deposited on Cs₂CO₃ (curve a), a-Si (curve b) and a-(Si,C) (curve c). Note how the quantum efficiency in the blue region increases when a-(Si,C) is used as the electron transport layer as opposed to a-Si.

layer is significantly lower. The reason for this is because of the absorption of UV and blue photons by the a-Si:H n⁺ layer, which is reflected as a reduction in quantum efficiency of the cell at shorter wavelengths, as shown in Fig. 3. It is possible to reduce the quantum efficiency loss at short wavelengths in the hybrid cell by using a larger bandgap for a-(Si,C):H, as shown in Fig. 3. However, it becomes difficult to dope larger gap a-(Si,C):H layers, and this difficulty leads to poor tunnel junctions between doped ZnO and the doped a-(Si,C):H ETL, and thereby leads to a kink in I-V curves, as shown in Fig. 4.
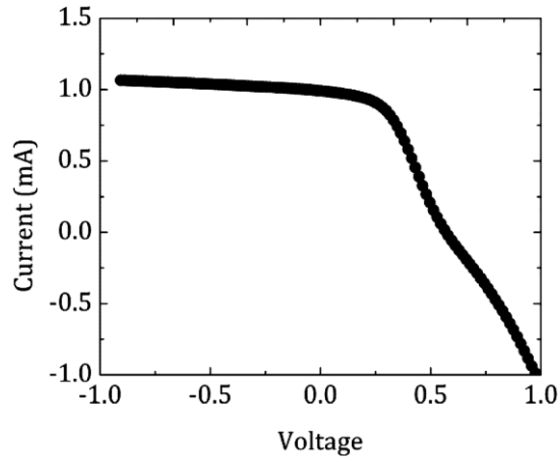
Samiee et. al., Appl. Phys. Lett. 105, 213909 (2014)

FIG. 4. Illuminated I-V curve when the cell is deposited on a doped a-(Si,C) layer. A slight non-ohmic behavior is evident, probably related to the difficulty of doping a-(Si,C) as methane content of a-(Si,C):H increases.
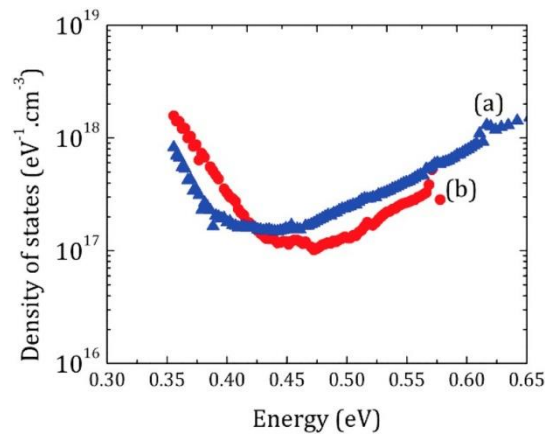

FIG. 5. Density of states at the interface between P3HT and PCBM measured using capacitance-frequency techniques for the two cells, one deposited on Cs2CO3 (curve b) and one on a-Si (curve a). The results are very similar.

In Fig. 5, we show the defect density for the hybrid and Cs_2CO_3 based cells, determined using capacitance-frequency techniques described earlier.[15] The defect density curves are very similar for both cases, showing that the fundamental bulk heterojunction layer (P3HT/PCBM) in both cases is very similar. We also measured subgap quantum efficiency (QE) for the cell deposited on a-Si and compared it with the subgap QE of a normal P3HT/PCBM Cell. As shown previously,[16,17] subgap QE probes deeper states in the donor material and at interfaces. The subgap QE curves shown in Fig. 6 are also very similar for
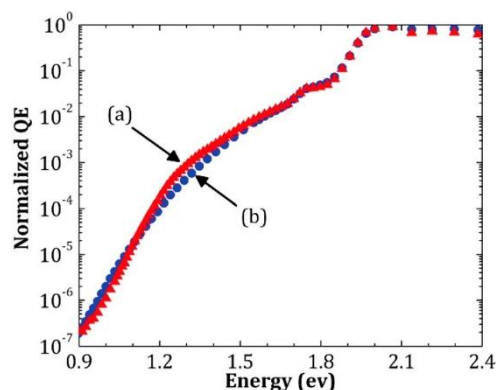
FIG. 6. Subgap quantum efficiency data for cells deposited on a-(Si,C) (curve a)and a normal P3HT/PCBM cell deposited on PEDOT:PSS (curve b). The results are very similar, indicating similar material properties.
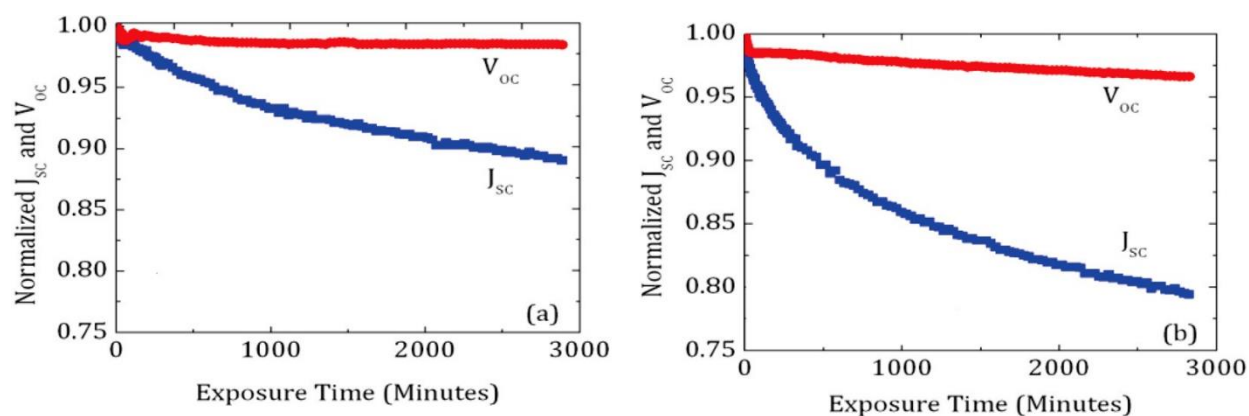

FIG. 7. Changes in open circuit voltage and short circuit current vs. exposure time for cells deposited on Cs_2CO_3 (bottom panel) and on a-(Si,C) (top panel) upon exposure to 2X solar intensity. The data were taken in a vacuum chamber filled with nitrogen to avoid changes due to oxygen or moisture. After light soaking, the fill factor of cell on Cs_2CO_3 degraded by 11%, and for the cell on a-Si, by 4%.

both these types of cells, further proving that the organic cell materials are very similar.

We next measured the stability of the two cells by subjecting them to 2X solar intensity (200 mW/cm²) from a full spectrum ABET solar simulator. Since the cell on a-Si produces less current, we increased the intensity of light falling on this cell using a lens so as to produce exactly the same current as in the inverted cell deposited on Cs_2CO_3. This was done to eliminate any differences that may arise in degradation between the two cells due to differences in photon flux and current-induced instability. The data are shown in Fig. 7 as changes in current and voltage after degradation for the two types of cells, and in Fig. 8

for changes in defect density for the two cells. It is very clear from these figures that the cell deposited on a-(Si,C):H n$^+$ layer is much more stable compared to the cell deposited on Cs_2CO_3. We believe this improvement in stability is a direct consequence of the fact that the a-Si-based ETL absorbs the UV and blue photons, and that these photons are breaking more bonds and creating more intrinsic defects in the material than longer wavelength (green and red) photons. Note that the intensity of longer wavelength photons shining on the hybrid cell was higher than on the standard cell (so as to produce the same short circuit currents in both cells). In spite of this higher intensity of green and red photons, the degradation in the hybrid cell was significantly lower.
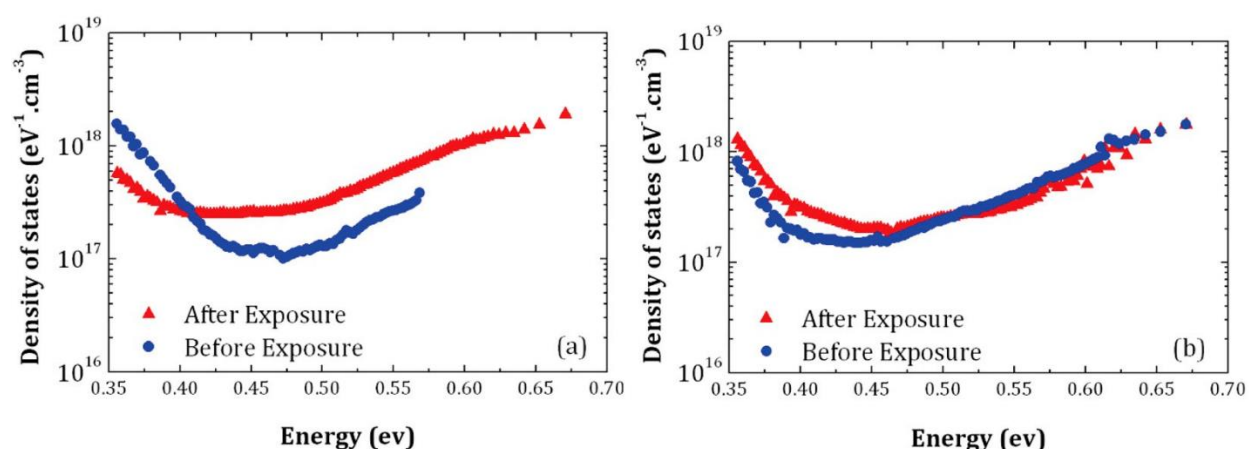

FIG. 8. Changes in defect density before and after exposure for cells deposited on Cs_2CO_3 (panel a) and on a-(Si,C) (panel b).

In summary, we have shown that it is feasible to use a hybrid approach, where one uses a doped inorganic semiconductor with well-controlled doping and matching electron affinities as electron transport layer, and still deposit an organic material with the same quality as deposited on standard ETLs. Another major result we have obtained is that having a UV and blue photon absorbing layer in front of the active layer significantly reduces degradation. This fact brings forth the importance of fabricating hybrid tandem-

junction solar cells,[18] where the first cell receiving light can be a larger gap inorganic cell, which will absorb the UV and blue photons and generate power, rather than wasting these photons as would be the case if a filter was used to block the higher energy photons.

References:

[1]Organic Photovoltaics: Materials, Device Physics, and Manufacturing Technologies edited by C. Brabec, U. Scherf, and V. Dyakonov (Wiley, VCH, 2009).
[2]F. Krebs, Sol. Energy Mater. Sol. Cells 93, 394 (2009).
[3]S. Gunes, H. Neugebauer, and N. Sariciftci, Chem. Rev. 107, 1324 (2007).
[4]S. H. Park, A. Roy, S. Beaupre, S. Cho, N. Coates, J. S. Moon, D. Moses, M. Leclerc, K. Lee, and A. J. Heeger, Nat. Photonics 3, 297 (2009).
[5]T. Xiao, W. Cui, J. Andregg, R. Shinar, and J. Shinar, Org. Electron. 12,257 (2011).
[6]Z. C. He, C. M. Zhong, S. J. Su, M. Xu, H. B. Wu, and Y. Cao, Nat. Photonics 6, 591 (2012).
[7]G. Li, C.-W. Chu, V. Shrotriya, J. Huang, and Y. Yang, Appl. Phys. Lett. 88, 253503 (2006).
[8]J.-C. Wang, W.-T. Weng, M.-Y. Tsai, M.-K. Lee, S. -Fu. Horng, T.-P. Perng, C.-C. Kei, C.-C. Yu, and H.-F. Meng, J. Mater. Chem. 20, 862 (2010).
[9]A. Tabata, Y. Kuno, Y. Suzuoki, and T. Mizutani, J. Phys. D. 30, 194 (1997).
[10]V. L. Dalal, S. Haroon, Z. Zhou, T. Maxson, and K. Han, J. Non-Cryst. Solids 266–269, 675 (2000).
[11]Y.-B. Park, S. K. Lee, O. Kim, and S.-W. Rhee, Jpn. J. Appl. Phys., Part 237, L77 (1998).
[12]M. O. Reese, A. J. Morfa, M. S. White, N. Kopidakis, S. E. Shaheen, G. Rumbles, and D. S. Ginley, Sol. Energy Mater. Sol. Cells 92, 746–752 (2008).
[13]F. C. Krebs and K. Norrman, Prog. Photovoltaics 15, 697 (2007).
[14]See, for example, W. A. Luft and Y. Simon Tsuo, Hydrogenated Amorphous Si Alloy Deposition Processes (Dekker, NY, 1993).
[15]K. S. Nalwa, R. C. Mahadevapuram, and S. Chaudhary, Appl. Phys. Lett.98, 093306 (2011).
[16]R. A. Street, A. Krakaris, and S. R. Cowan, Adv. Funct. Mater. 22, 4608 (2012).
[17]J. Bhattacharya, R. W. Mayer, M. Samiee, and V. L. Dalal, Appl. Phys. Lett. 100, 193501 (2012).
[18]S. Pattnaik, T. Xiao, R. Shinar, J. Shinar, and V. L. Dalal, IEEE J. Photovolt. 3, 295 (2013).

APPENDIX C
DEFECT DENSITY AND DIELECTRIC CONSTANT IN PEROVSKITE SOLAR CELLS

Mehran Samiee,[1] Siva Konduri,[1] Balaji Ganapathy,[2] Ranjith Kottokkaran,[2] Hisham A. Abbas,[1] Andrew Kitahara,[3] Pranav Joshi,[1] Liang Zhang,[1] Max Noack,[2] and Vikram Dalal[1]

[1]Department of Electrical and Computer Engineering, Iowa State University, Ames, Iowa 50011, USA

[2]Microelectronics Research Center, Iowa State University, Ames, Iowa 50011, USA

[3]Department of Materials Science and Engineering, Iowa State University, Ames, Iowa 50011, USA.

Abstract- We report on measurement of dielectric constant, mid-gap defect density, Urbach energy of tail states in $CH_3NH_3PbI_xCl_{1-x}$ perovskite solar cells. Midgap defect densities were estimated by measuring capacitance vs. frequency at different temperatures and show two peaks, one at 0.66 eV below the conduction band and one at 0.24 eV below the conduction band. The attempt to escape frequency is in the range of $2x10^{11}$/s. Quantum efficiency data indicate a bandgap of 1.58 eV. Urbach energies of valence and conduction band are estimated to be 16 and 18 meV. Measurement of saturation capacitance indicates that the relative dielectric constant is 18. © 2014 AIP Publishing LLC. [*http://dx.doi.org/10.1063/1.4897329*]

Perovskite solar cells based on methyl amine lead iodide-chloride (MAX_3) system are a new and exciting tech- nology for solar energy conversion.[1-11] High solar conversion efficiencies have been obtained in this material system, with efficiencies exceeding 17% having been reported.[12-14]

This material, which is poly-crystalline, is remarkable in that it shows very high absorption coefficients, characteristic of organic dyes, and yet has a relatively small exciton binding energy of ~(55±20) meV,[15] thereby assuring that electrons and holes separate out

by thermal decomposition. For all practical purposes, the material behaves as an inorganic semiconductor with relatively large diffusion lengths approaching 1 μm for both carriers.[16] For device optimization, one needs to know fundamental properties such as defect densities in the material, tail state densities, and Urbach energies of tail states.

We used two types of device structures for our measurements: a p-i-n cell and a n-i-p cell. The intermediate base layer is designated "i" because it is not intentionally doped even though, in general, it is n-type. The p-i-n device was deposited on ITO substrates coated with PEDOT:PSS (Poly (3,4-ethyle-nedioxythiophene) Polystyrene sulfonate), and light entering the cell from the p side. The n-i-p structure consisted of the normally used TiO2/perovskite/p-heterojunction/gold structure, with TiO_2 deposited on FTO (Fluorine-doped Tin Oxide), and light entering the n side first. See Fig. 1 for a schematic diagram of the two structures. For p-i-n cell, a PEDOT:PSS layer was spin coated onto ITO substrates, followed by annealing at 110 C. Then, the perovskite layer was deposited on top of PEDOT:PSS using a single solvent method.[8] The films were then annealed at 90 C for 90 min until perovskite forms. The n+ PCBM (Phenyl-C61-Butyric acid Methyl ester) layer was then spin-coated on top of perovskite. The devices were then finished by thermally evaporating aluminium. For the n-i-p cell, TiO_2 was deposited on FTO using the method described by Chen et al.,[17] followed by vapour deposition of lead iodide and
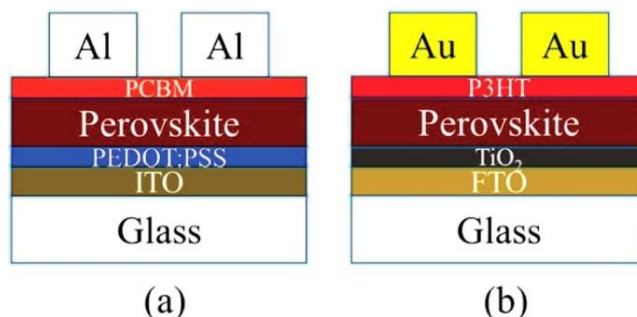
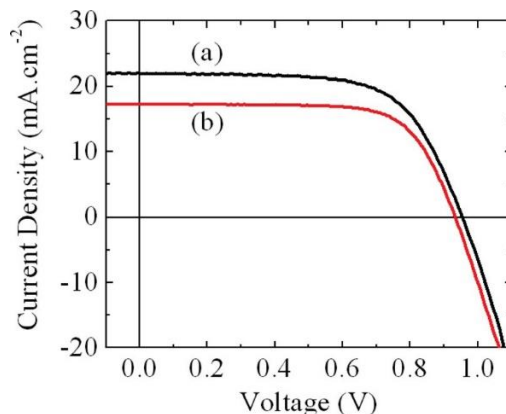FIG. 1. Schematic diagrams of n-i-p and p-i-n perovskite solar cells.

FIG. 2. Illuminated I-V curves of n-i-p (a) and p-i-n (b) cells measured using solar simulator. The conversion efficiencies are 11% for p-i-n cell and 14% for n-i-p cell.

methylammonium iodide. The hole-transporting layer was formed by spin-coating a layer of P3HT (Poly-3-Hexyl Thiophene) from solution, and the device was completed by thermally evaporating 80 nm of circular gold contacts.

The illuminated I-V curve for the two types of cells are shown in Fig.2. The p-i-n cell has a power conversion efficiency of ~11.5% and the n-i-p cell, ~14%. The thickness of the perovskite layer for the p-i-n cell was ~160 nm and for n-i-p cell, ~480 nm. The corresponding quantum efficiency (QE) curves are shown in Fig. 3(a),
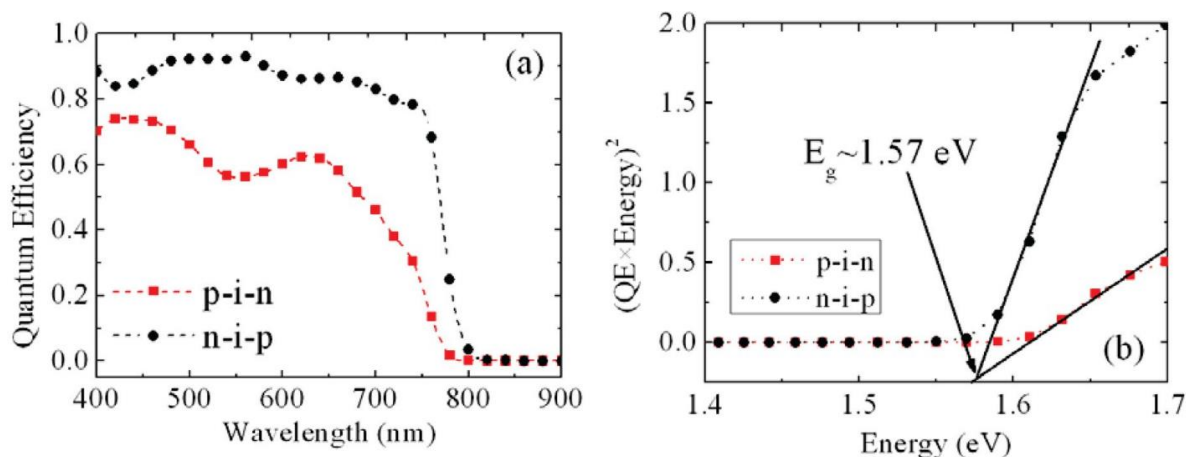
FIG. 3.. *Quantum efficiency (QE) vs. wavelength data (panel a) and (QE×E)² vs. photon energy E data in (panel b) for both n-i-p and p-i-n cells. The intercept on the energy axis in (b) indicates a bandgap of 1.58 eV for both types of cells.*
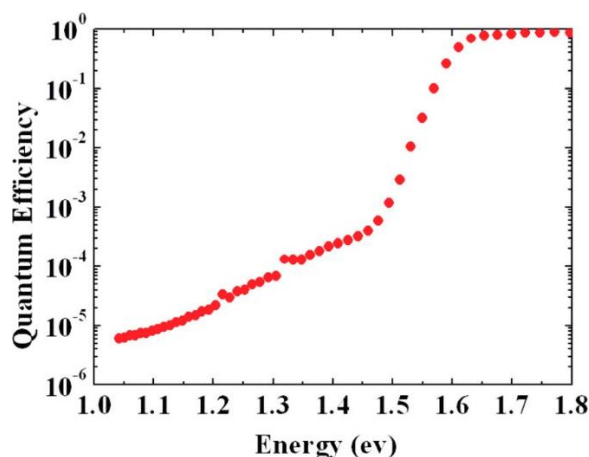

FIG. 4. Subgap QE data for the n-i-p cell showing an Urbach energy of 16 meV for valence band edge, and defect states extending to mid-gap region.

and they show QE extending out to 800 nm. One can calculate the bandgap by plotting $[(QE){\times}E]^2$ vs. photon energy E, and the intercept gives the bandgap. The chart in Fig. 3(b) shows a bandgap of 1.6 eV.

Subgap quantum efficiency was also measured in these devices and the curve for a n-i-p cell is shown in Fig. 4. The data shows a fall off below ~1.65 ev, with an exponential tail below ~1.6 eV indicating the presence of tail states. The Urbach energy for valence band states is 16 meV. The data below 1.5 eV indicates the presence of midgap states.

Assuming the usual value for the density of conduction band states in inorganic semiconductors to be ∼ 10^{21}/cm³.eV, [18] the midgap state density is found to be in the range of ∼10^{16}/cm³-eV, in good agreement with the capacitance data which are discussed later.

We next measured the deep defects using capacitance(C)-frequency (f) techniques [19-24] at various temperatures. In this method, as the frequency decreases, deeper traps participate in capacitance, and hence, capacitance increases. Walters et. al.[19] showed that the defect density at a given energy is proportional to f x dC/df. They also show that distinct peaks arise in [f x dC/df] vs. frequency data when the measurements are done at different temperatures. These peaks arise because the emission rate from a trap responding at a given frequency depends very strongly on the energy of the trap and the measurement temperature. The emission rate for a given trap position is given by [22]:

$$e_n = N_c \langle v_{th} \rangle \sigma_n \exp\left(\frac{-E_T}{k_B T}\right) \qquad (1)$$

where N_c is the effective conduction band density of states, $\langle v_{th} \rangle$ the RMS thermal velocity of electrons, σ_n the capture cross section, E_T the trap activation energy, k_B the Boltzmann constant and T the temperature. Eq. (1) is an Arrhenius equation, in which the emission rate is heavily dependent on the trap depth, the sample temperature and the pre-exponential factor $N_c \langle v_{th} \rangle \sigma_n$. It is this prefactor that is commonly known as 'the attempt to escape frequency' (v_0), [19] and its characterization is essential if trapping dynamics are to be accurately described.

From eq. (1), a plot of ln(e_n), (e_n being the measurement frequency at which the peak occurs), vs. $1/k_B T$ will yield a value for the trap energy. Then, knowing the activation energy, one can calculate the attempt-to-escape-frequency form the peaked [f x dC/df]

curve. When making a plot vs. 1/kT, one must be mindful of the fact that $N_c \sim T^{3/2}$ [25], and $<v_{th}>$ is $\sim T^{1/2}$ [26]. Therefore, one must plot ln (e_n/T^2) vs. 1/kT, and then the slope gives a value for trap energy E_T.

In Fig. 5, we show the experimental data for [f x dC/df] vs. frequency, measured at various temperatures. The inset in the figure shows that the data indicates that there is a secondary peak related to a trap at a different energy in addition to the main peak. The trap energy plot deduced from the data of Fig. 5 are shown in Fig.6, and the slope indicates trap energies of 0.66 eV below the conduction band and 0.24 eV below the conduction band.
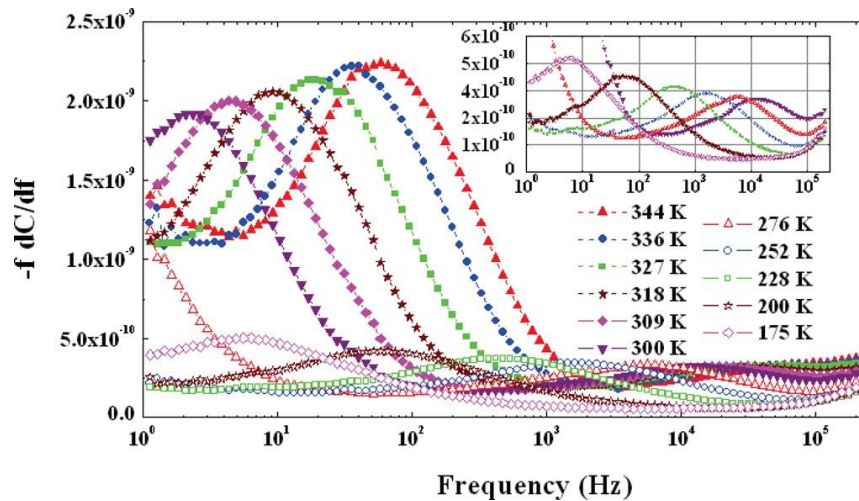

FIG. 5. Capacitance(C) vs. frequency (f) data, drawn as (C×dC/df) vs. frequency, for the n-i-p cell taken at various temperatures. The peaks correspond to attempt to escape frequencies at different temperatures. There are two distinct curves, a main set of curves corresponding to a major defect and a second curve shown in the inset indicating the presence of secondary peak in defect density.

The attempt-to-escape frequency υ_0 calculated from the peaks for the dominant trap is $\sim 2\times 10^{11}$/s, in the usual range for inorganic solids [19, 27, 28]. The defect density deduced from C-f plots at room temperature is plotted in Fig. 7(a) as a function of energy and shows a major peak at around 0.65 eV below conduction band, with a peak value of 3×10^{16}/cm^3.eV, in good agreement with the value estimated from the subgap QE data. The sharp decrease in density at low energies probably corresponds to tail states near the
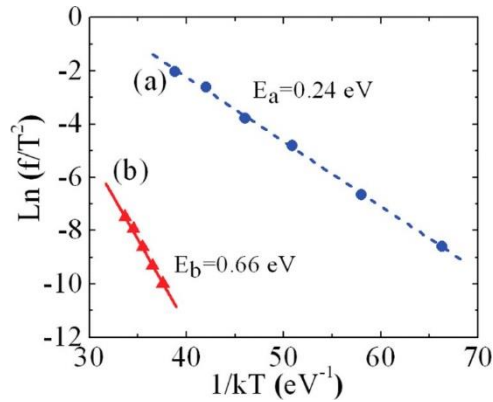
Samiee et. al., Appl. Phys. Lett. 105, 153502 (2014)

FIG. 6. Arrhenius curves of peak frequencies shown in Fig. 5 vs. 1/kT for both the primary and secondary curves shown in Fig. 5. The primary curve indicates a deep trap energy of 0.66 eV, and the secondary curve indicates a trap energy of 0.24 eV.
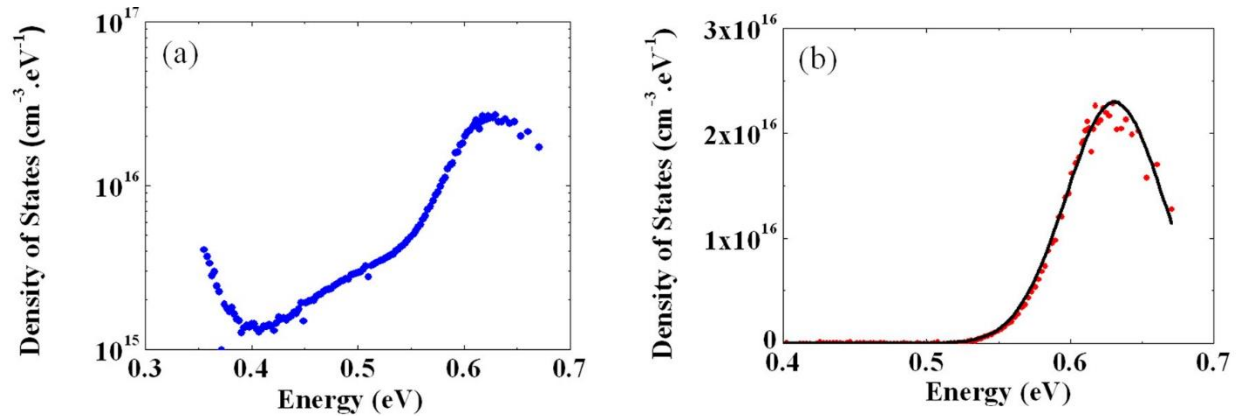

FIG. 7. Defect densities deduced from C-f data at 300K plotted vs. energy. The sharp drop-off at lower energies corresponds to an Urbach tail near the conduction band, with a value of Urbach energy of 18meV. The inset shows that the peak in defect density is well matched to a Gaussian shape centered at 0.65eV, in good agreement with the value of 0.66eV deduced for this defect from Arrhenius plot of Fig. 6.

conduction band with Urbach energy of ~18 meV. The defect density, when plotted on a linear plot, shows an excellent Gaussian shape, as shown in Fig. 7(b).

Capacitance measurements also provide a value for the relative dielectric constant of the perovskite. In Fig. 8, we plot the capacitance measured at low frequency where all traps respond vs. applied voltage. The saturation value for the capacitance indicates that the depletion layer has spread to the back doped contact layer. We independently
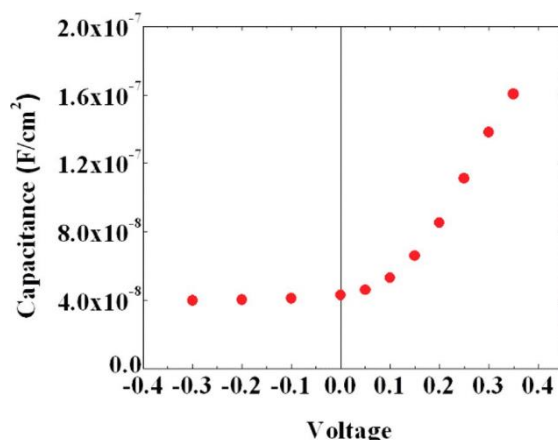
FIG. 8. Capacitance vs. voltage data in forward and reverse directions measured at low frequency. The saturation at reverse voltages corresponds to the depletion layer extending throughout the i layer. Knowing the independently-measured i-layer thickness of ~460nm, the saturated capacitance gives a value for the relative dielectric constant=18.

measured the physical thickness of the i layer in the perovskite n-i-p cell. By comparing the saturation capacitance, whose value is given by $\varepsilon A/t$, where t is the thickness, A the area and ε the dielectric constant, we determine that the relative dielectric constant is ~18. This result is in agreement with values derived from first-principle calculations for $CH_3NH_3PbI_3$ by Brivio et. al. [29].

In summary, we have measured the deep defect densities, attempt-to-escape frequency Urbach energies and relative dielectric constant in high quality Pb-halide based perovskite devices.

References:

[1] M. Liu, M. B. Johnston, H. J. Snaith, *Nature* **501**, 395 (2013)

[2] J. Burschka, N. Pellet, S.-J. Moon, R. Humphry-Baker, P. Gao, M. K. Nazeeruddin, M. Grätzel, *Nature* **499**, 316(2013)

[3] G. Hodes. *Science*, **342**, 317-318 (2013)

[4] H. J. Snaith, *J. Phys.Chem. Lett.* **4**, 3623 (2013)

[5] N. −G. Park, *J. Phys. Chem. Lett.* **4**, 2423-2429 (2013)

[6] N. K. Mohammad, P. Gao, M. Grätzel. *Energy Environ. Sci.* 2014, DOI: 10.1039/C4EE00942H.

[7] T. C. Sum, N. Mathews. *Energy Environ. Sci.* 2014, DOI: 10.1039/C4EE00673A.

[8] J. You, Z. Hong, Y. (Micheal) Yang, Q. Chen, M. Cai, T. Song, C. Chen, S. Lu, Y. Liu, H. Zhou, Y. Yang, *ACS Nano,*. **8**, No. 2, 1674-1680 (2014).

[9] V. Gonzalez-Pedro, E. J. Juarez-Perez, W. Arsyad, E. M. Barea, F. Fabregat-Santiago, I. Mora-Sero, J. Bisquert. *Nano Lett.*, **14**, 888-893(2014).

[10] G. E. Eperon, V. M. Burlakov, A. Goriely, H. J. Snaith. *ACS Nano*, **8**, 591-598(2014).

[11] L. Etgar, P. Gao, Z. Xue, Q. Peng, A. K. Chandiran, B.Liu, M. K. Nazeeruddin, M. Grätzel *J. Am. Chem. Soc.* **134**, 17396-399 (2014).

[12] J. Im, I. Jang, N. Pellet, M. Gratzel, and N. Park, *Nature Nanotechnology*, 2014, DOI: 10.1038/NNANO.2014.181

[13] NREL efficiency chart, 2014, http://www.nrel.gov/ncpv/images/efficiency_chart.jpg

[14] H. Zhou, Q. Chen, G. Li, S. Luo, T. Song, H. Duan, Z. Hong, J. You, Y. Liu, Y. Yang, *Science*, Vol. 345, No. 6196, pp.542-546, 2014.

[15] V. D'Innocenzo, G. Grancini, M. J. P. Alcocer, A. R. S. Kandada, S. D. Stranks, M. M. Lee, G. Lanzani, H. J. Snaith, A. Petrozza. *Nature Communications* 2014, DOI: 10.1038/ncomms4586.

[16] S. D. Stranks, G. E. Eperon, G. Grancini, C. Menelaou, M. J. P. Alcocer, T. Leijtens, L. M. Herz, A. Petrozza, H. J. Snaith. *Science*, **342**, 341-344(2013).

[17] Q. Chen, H. Zhou, Z. Hong, S. Luo, H. Duan, H. Wang, Y. Liu, G. Li, and Y. Yang, *J. Am. Chem. Soc.*, Vol. 136, pp. 622–625, 2014.

[18] J. Joannopoulos, and M. L. Cohen, *Phys. Rev. B.*, Vol. 10, No. 4, 1545-1559

[19] T. R. Walter, T. R. Herberholz, C.Muller and H. W. Schock, *J. Appl. Phys.* **80**, 4411(1996).

[20] J. Bhattacharya, R. W. Mayer, M. Samiee and V. L. Dalal, *Appl. Phys. Lett.*, **100**, 193501(2012).

[21] J. A. Carr, S. Chaudhary. *Appl. Phys. Lett.* **100**, 213902(2012).

[22] J.A. Carr, S. Chaudhary. *J. Appl. Phys.* **114**, 064509 (2013).

[23] G. Balaji, M.S. Esfahani, P. Joshi, J. Bhattacharya, M. Jefferies-EL, V. Dalal, *Eur. Polym. J.*, **49**, 3921(2013)

[24] M. Samiee, B. Modtland, D. Aidarkhanov, V. L. Dalal, *Applied Phys. Lett.* 104, 213909 (2014).

[25] R. F. Pierret, "Advanced Semiconductor Fundamentals", Second Edition, Prentice Hall, pp. 112.

[26] i.b.i.d., pp.152.

[27] S. S. Hegedus, E. A. Fagen, *J. Appl. Phys.***71**, 5941 (1992)

[28] T. Dylla, F. Finger, E. A. Schiff, *Appl. Phys. Lett.* **87**, 032103 (2005).

[29] F. Brivio, A. Walker, and A. Walsh, *APL Materials* 1, 042111 (2013).